Measurement of the δ and η muon decay parameters.

by

Anthony Hillairet
B.Sc., Université Joseph Fourier, Grenoble, France, 2003
M.Sc., Université de Strasbourg, Strasbourg, France, 2005

A Dissertation Submitted in Partial Fulfillment of the
Requirements for the Degree of

DOCTOR OF PHILOSOPHY

in the Department of Physics and Astronomy

Measurement of the δ and η muon decay parameters.

by

Anthony Hillairet

B.Sc., Université Joseph Fourier, Grenoble, France, 2003

M.Sc., Université de Strasbourg, Strasbourg, France, 2005

Supervisory Committee

Dr. A. Olin, Supervisor

(Department of Physics and Astronomy)

Dr. M. Lefebvre, Co-supervisor

(Department of Physics and Astronomy)

Dr. R. Kowalewski, Departmental Member

(Department of Physics and Astronomy)

Dr. D. Harrington, Outside Member

(Department of Chemistry)

Supervisory Committee

Dr. A. Olin, Supervisor
(Department of Physics and Astronomy)

Dr. M. Lefebvre, Co-supervisor
(Department of Physics and Astronomy)

Dr. R. Kowalewski, Departmental Member
(Department of Physics and Astronomy)

Dr. D. Harrington, Outside Member
(Department of Chemistry)

ABSTRACT

Muon decay is a unique process involving only the four leptons of the first two generations. This makes it an ideal framework to study the weak interaction. The momentum-angle spectrum of the decay positron can be studied using a general 4-fermion interaction model. Only four parameters are needed in this model to entirely describe the spectrum. The measurement of these four muon decay parameters, ρ, η, δ and $P_\mu\xi$, provide a direct test of the Standard Model and its extensions.

This thesis presents the final results from the blind analysis of the decay parameter δ using the TWIST (TRIUMF Weak Interaction Symmetry Test) spectrometer. The new precision on the parameter δ is a factor of 11.5 better than the last experimental result prior to TWIST achieving the goal of the TWIST collaboration of an order of magnitude improvement. The challenging parameter η is also measured from the momentum-angle spectrum for the first time since 1969 with a precision improved by a factor of 7.4.

The results are included in a global analysis to obtain stringent limits on some of the coupling constants of the 4-fermion interaction. The result of the measurement of δ are used to evaluate the possibility for a non-local tensor interaction.

ABSTRACT

La désintégration du muon constitue une unique réaction impliquant seulement les quatre leptons des deux premières générations ce qui la rend idéale pour l'étude de l'interaction faible. Le spectre en angle et impulsion du positron issue de la désintégration peut être décrit entièrement par seulement quatre paramètres en utilisant un modèle d'interaction de contact général à quatre fermions. La mesure des quatre paramètres de désintégration, ρ, η, δ et $P_\mu\xi$, permet de tester directement le Modèle Standard ainsi que d'autres modèles au-delà du Modèle Standard.

Cette thèse présente les résultats de l'analyse en aveugle du paramètre δ par le spectromètre TWIST (TRIUMF Weak Interaction Symmetry Test). Le paramètre δ a été mesuré avec une précision 11.5 fois meilleure que celle de l'expérience précédent TWIST, atteignant ainsi l'objectif de la collaboration d'une mesure d'un ordre de grandeur plus précise. Le paramètre η a aussi été mesuré à partir du spectre en angle et impulsion pour la première fois depuis 1969. Cette nouvelle mesure est un facteur 7.4 plus précise que la mesure précédente.

Ces résultats sont comparés aux prédictions du Modèle Standard. Ils sont aussi utilisés dans une analyse globale pour obtenir des limites sur certaines constantes de couplage de l'interaction générale à quatre fermions. Le résultat de la mesure de δ permet également d'évaluer la présence d'une interaction tensorielle non-locale.

Contents

List of Tables

List of Figures

ACKNOWLEDGEMENTS

I would like to thank the whole TWIST collaboration for welcoming me and providing me with a wonderful environment to learn and develop my skills as a physicist. Thank you in particular to Art Olin for his supervision and his help and advices to write this thesis. A special thanks to Glen Marshall for creating an amazing work environment in the group and for entrusting me with responsibilities. Thank you to Richard Mischke for his management of the analysis effort and his corrections on this thesis.

The technical staff at TRIUMF provided us with a great technical support during the acquisition of the data but also with the maintenance of the computers of the collaboration during the analysis. Thank you to Grant Sheffer for his careful technical work on the experiment at any time we needed him which helped me considerably as a run coordinator. Renée Poutissou was also crucial to the acquisition system and the computing component of the experiment, and she taught me a lot about computer administration.

A special thanks to my fellow graduate students and especially to James Bueno for helping me whenever I needed him during these four and a half years, in particular with writing this thesis and for the work we did together on the analysis. Also thank you to Alexander "cryptic" Grossheim for the very interesting discussions especially during the development of Clark.

I would like to thank Abdenour Lounis and Pierre Depommier for introducing me to the TWIST collaboration. Thank you to Michel Lefebvre for welcoming me at UVic and for taking care of all the administrative elements of the PhD program which allowed me to focus on my research.

Finally I want to thank my family and friends for their support. In particular thank you to Sean Bailly, Maud Versteegen, Peter Winslow and Reka Moldovan for being there when I needed them. Thank you to my sister Stéphanie for being the best sister. A special thanks to Ghazal Maleki for her presence and her support during the past year and a half and especially during the writing of this thesis.

The truth may be puzzling. It may take some work to grapple with. It may be counterintuitive. It may contradict deeply held prejudices. It may not be consonant with what we desperately want to be true. But our preferences do not determine what's true.

Carl Sagan

Chapter 1

Introduction

1.1 Physics motivation

The muon was crucial to the development of particle physics. It was one of the first unstable subatomic particles discovered and studied. This early discovery in 1936 [1] is due to the abundance of muons in cosmic rays at ground level. Muons are now produced at high rate in facilities such as TRIUMF, which makes high precision measurements possible.

Particle physics has come a long way since the discovery of the muon. The theoretical framework of particle physics, namely the Standard Model [2], is a successful theory capable of describing the experimental results at all reachable energies in current accelerators. The only piece missing to validate the Standard Model predictions is the Higgs boson and its discovery is expected in the coming years at the Large Hadron Collider at CERN.

Despite many successes, the scientific community believes that the Standard Model is a low energy limit of a more general theory [3]. Due to the accuracy of the Standard Model at low energy, a new theory is expected to be an extension rather than a replacement. Even if the new developments are expected at high energy, the new physics beyond the Standard Model could be measurable at low energy in processes such as muon decay.

In the Standard Model the muon decays through the weak interaction [4] and is described by the exchange of a virtual charged W boson which interacts only with left-handed particles and right-handed anti-particles. This pure leptonic decay provides useful observables to study the weak interaction while being free of strong

interactions.

The TWIST (TRIUMF Weak Interaction Symmetry Test) experiment was designed to measure the momentum-angle spectrum of the decay positron from highly polarized muons. Some properties of muon decay are measurable from the momentum-angle spectrum despite the fact that a significant part of the decay information is carried away by the two neutrinos. One significant advantage of this measurement is the possibility to use a model-independent approach. This theoretical framework describes the momentum-angle spectrum shape using the four decay parameters η, ρ, δ and $P_\mu\xi$. A precise measurement represents a direct test of the predictions of the Standard Model for these parameters. The four muon decay parameters also provide stringent limits on models describing physics beyond the Standard Model.

This chapter will present the model-independent framework used to extract the observables from the momentum-angle spectrum of the decay positron. The theoretical implications of the measurement of these observables will be described. Finally an overview of the TWIST experiment will introduce the blind analysis results of the final measurement of the δ parameter and the first measurement of the η parameter from the TWIST collaboration.

1.2 Theoretical description of muon decay

1.2.1 General 4-fermion interaction

To study muon decay in a model independent manner, one can use the general 4-fermion point interaction. This point-like interaction is a valid approximation because the mass of the W-boson is almost three orders of magnitude larger than the mass of the muon.

We use at this point very general assumptions; the interaction is described as local, derivative-free, Lorentz-invariant and lepton-number conserving. The matrix element [5] is therefore:

$$M = 4\frac{G_F}{\sqrt{2}} \sum_{\substack{\gamma=S,V,T \\ \epsilon,\mu=R,L}} g^\gamma_{\epsilon\mu} < \bar{e}_\epsilon|\Gamma^\gamma|\nu_e >< \bar{\nu}_\mu|\Gamma_\gamma|\mu_\mu > .$$

(1.1)

The factor G_F is the Fermi constant which is extracted from the muon lifetime. The

subscript and superscript γ represent the type of the interaction with S for scalar, V for vector and T for tensor:

$$\Gamma^S = 1, \qquad \Gamma^V = \gamma^\alpha, \qquad \Gamma^T = \sigma^{\alpha\beta} = \frac{1}{\sqrt{2}}(\gamma^\alpha\gamma^\beta - \gamma^\beta\gamma^\alpha) \qquad (1.2)$$

where γ^α are the Dirac matrices. The complex coupling constants $g^\gamma_{\epsilon\mu}$ give the relative strength of the interaction γ. Finally the subscripts ϵ and μ describe respectively the chirality of the electron and the muon.

Only 19 real and independent coupling constants are needed to completely describe the interaction because we have $g^T_{RR} \equiv 0$ and $g^T_{LL} \equiv 0$, and a common phase doesn't matter. The coupling constants are conventionally normalized [6] such that the strength of the overall interaction is contained in the constant G_F:

$$
\begin{aligned}
\frac{1}{4}\left(|g^S_{RR}|^2 + |g^S_{RL}|^2 + |g^S_{LR}|^2 + |g^S_{LL}|^2\right) &+ \\
|g^V_{RR}|^2 + |g^V_{RL}|^2 + |g^V_{LR}|^2 + |g^V_{LL}|^2 &+ \\
3\left(|g^T_{RL}|^2 + |g^T_{LR}|^2\right) \quad &= 1.
\end{aligned} \qquad (1.3)
$$

1.2.2   Momentum-angle spectrum parametrization

From this matrix element we can calculate the differential decay rate of polarized muons:

$$\frac{d^2\Gamma}{dx\,d\cos\theta_T} = \frac{m_\mu}{4\pi^3}W^4_{e\mu}G^2_F\sqrt{x^2 - x_0^2}\Big(F_{IS}(x) + P_\mu\cos\theta_T F_{AS}(x)\Big) + \mathrm{RC}(x, \cos\theta_T). \quad (1.4)$$

where $x = E_e/W_{e\mu}$ is the reduced positron[1] energy with the maximum energy for the positron $W_{e\mu} \equiv (m_\mu^2 + m_e^2)/2m_\mu$; the minimum positron energy is $x_0 \equiv m_e/W_{e\mu}$; the angle θ_T is the angle between the positron momentum and the muon polarization P_μ; $\mathrm{RC}(x, \cos\theta_T)$ are the radiative corrections. The experimental angle θ is defined between the z axis of the spectrometer and the decay positron momentum vector. The z axis corresponds to the bore of the solenoidal magnetic field and to the direction of the incoming muons. The muons are anti-polarized with respect to the z axis. For

---

[1]The TWIST measurement is performed on the decay of positive muons. For this reason the focus is on decay positrons. The negative muons become quickly bound in the atoms of the target material. The decay in orbit of the negative muons boots the outgoing electron which distorts the momentum-angle spectrum significantly. A small dataset of negative muon was taken and analyzed to study the muon decay in orbits [7].

this reason the experimental $\cos \theta$ has the opposite sign compared to the theoretical $\cos \theta_T$.

The isotropic and anisotropic parts of the spectrum are:

$$
\begin{aligned}
F_{IS}(x) = \;& x(1-x) + \frac{2}{9}\rho(4x^2 - 3x - x_0^2) + \eta x_0(1-x) \\
F_{AS}(x) = \;& \frac{1}{3}\xi\sqrt{x^2 - x_0^2}\left[1 - x + \frac{2}{3}\delta(4x - 3 + (\sqrt{1 - x_0^2} - 1))\right].
\end{aligned}
\tag{1.5}
$$

The four muon decay parameters ρ, η, δ and ξ are real bilinear combinations of the coupling constants $g_{\epsilon\mu}^\gamma$. They are generally referred to as the Michel Parameters although only ρ was introduced by L. Michel [8]. The other parameters were introduced in [9][10][11]. Their expressions in terms of the coupling constants are:

$$
\begin{aligned}
\rho = \;& \frac{3}{4} - \frac{3}{4}\left[\left|g_{RL}^V\right|^2 + \left|g_{LR}^V\right|^2 + 2\left|g_{RL}^T\right|^2 + 2\left|g_{LR}^T\right|^2\right. \\
& \left. + \Re\left(g_{RL}^S g_{RL}^{T*} + g_{LR}^S g_{LR}^{T*}\right)\right],
\end{aligned}
\tag{1.6}
$$

$$
\begin{aligned}
\eta = \;& \frac{1}{2}\;\Re\left[g_{RR}^V g_{LL}^{S*} + g_{LL}^V g_{RR}^{S*} + g_{RL}^V\left(g_{LR}^{S*} + 6g_{LR}^{T*}\right)\right. \tag{1.7} \\
& \left. + g_{LR}^V(g_{RL}^{S*} + 6g_{RL}^{T*})\right], \tag{1.8}
\end{aligned}
$$

$$
\begin{aligned}
\xi = \;& 1 - \frac{1}{2}\left|g_{LR}^S\right|^2 - \frac{1}{2}\left|g_{RR}^S\right|^2 - 4\left|g_{RL}^V\right|^2 + 2\left|g_{LR}^V\right|^2 - 2\left|g_{RR}^V\right|^2 \tag{1.9} \\
& + 2\left|g_{LR}^T\right|^2 - 8\left|g_{RL}^T\right|^2 + 4\Re(g_{LR}^S g_{LR}^{T*} - g_{RL}^S g_{RL}^{T*}), \text{ and}
\end{aligned}
$$

$$
\begin{aligned}
\xi\delta = \;& \frac{3}{4} - \frac{3}{8}\left|g_{RR}^S\right|^2 - \frac{3}{8}\left|g_{LR}^S\right|^2 - \frac{3}{2}\left|g_{RR}^V\right|^2 - \frac{3}{4}\left|g_{RL}^V\right|^2 - \frac{3}{4}\left|g_{LR}^V\right|^2 \tag{1.10} \\
& - \frac{3}{2}\left|g_{RL}^T\right|^2 - 3\left|g_{LR}^T\right|^2 + \frac{3}{4}\Re(g_{LR}^S g_{LR}^{T*} - g_{RL}^S g_{RL}^{T*}).
\end{aligned}
$$

These four parameters (with the addition of the radiative corrections) are sufficient to describe the shape of the momentum-angle spectrum of the decay positron (Fig. 1.1).

In the Standard Model the interaction is purely of the form V-A and therefore the only non-zero constant is $g_{LL}^V = 1$. The corresponding predictions for the muon
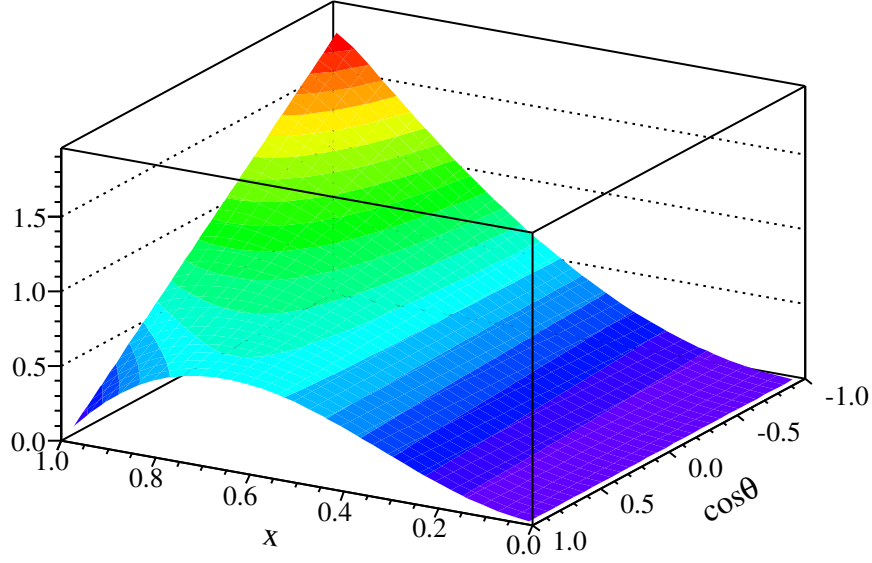
Figure 1.1: Theoretical momentum-angle spectrum of the decay positron from polarized muons. This spectrum uses the Standard Model values for the decay parameters and do not contain any radiative correction. The definition of $\cos\theta$ corresponds here to the experimental angle.

decay parameters are:

$$\rho = \frac{3}{4}, \qquad \eta = 0, \qquad \xi = 1, \qquad \delta = \frac{3}{4} \qquad (1.11)$$

The parameter ξ cannot be measured independently because it appears in Eq. (1.4) as a product of the muon polarization P_μ. Consequently only the combination $P_\mu\xi$ can be measured from the momentum-angle spectrum shape. The Standard Model prediction for the polarization P_μ^π at the time of the muon production from pion decay leads to:

$$P_\mu^\pi\xi = 1. \qquad (1.12)$$

The measured polarization differs from the polarization at the time of the muon production because of depolarization processes. Therefore the determination of $P_\mu^\pi\xi$ from our measurement of $P_\mu\xi$ relies on the knowledge of the depolarization processes.

1.3 Theoretical implications

1.3.1 Global analysis

The four muon decay parameters describing the momentum-angle spectrum are not sufficient to determine or limit the individual coupling constants $g_{\epsilon\mu}^{\gamma}$. A global analysis, performed by Gagliardi et al. [12], provided limits on the individual couplings by combining all the following muon decay observables [6]:

- the four muon decay parameters ρ, η, $P_\mu\xi$ and δ

- the measurement of $P_\mu\xi\delta/\rho$

- the parameters ξ' and ξ'' from the longitudinal polarization of the outgoing positrons

- the parameters η'', α, β, α' and β' from the transverse polarization of the outgoing positrons

- the parameter $\bar{\eta}$ from the radiative muon decay

The coupling constants are combined in an alternative set of bilinear combinations to facilitate the analysis:

$$
\begin{aligned}
Q_{RR} &= \frac{1}{4}|g_{RR}^S|^2 + |g_{RR}^V|^2 \\
Q_{LR} &= \frac{1}{4}|g_{LR}^S|^2 + |g_{LR}^V|^2 + 3|g_{LR}^T|^2 \\
Q_{RL} &= \frac{1}{4}|g_{RL}^S|^2 + |g_{RL}^V|^2 + 3|g_{RL}^T|^2 \\
Q_{LL} &= \frac{1}{4}|g_{LL}^S|^2 + |g_{LL}^V|^2 \\
B_{LR} &= \frac{1}{16}|g_{LR}^S + g_{LR}^T|^2 + |g_{LR}^V|^2 \\
B_{RL} &= \frac{1}{16}|g_{RL}^S + g_{RL}^T|^2 + |g_{RL}^V|^2 \\
I_\alpha &= \frac{1}{4}[g_{LR}^V(g_{RL}^S + 6g_{RL}^T)^* + (g_{RL}^V)^*(g_{LR}^S + 6g_{LR}^T)] \\
I_\beta &= \frac{1}{2}[g_{LL}^V(g_{RR}^S)^* + (g_{RR}^V)^* g_{LL}^S]
\end{aligned}
\tag{1.13}
$$

In particular the parameters $Q_{\epsilon\mu}$ represent the total probabilities for a μ-handed muon to decay into a ϵ-handed positron. Furthermore these bilinear combinations must satisfy the following constraints:

$$0 \leq Q_{\epsilon\mu} \leq 1, \qquad \text{where } \epsilon, \mu = R, L$$
$$0 \leq B_{\epsilon\mu} \leq Q_{\epsilon\mu}, \qquad \text{where } \epsilon\mu = RL, LR$$
$$|I_\alpha|^2 \leq B_{LR}B_{RL}, \qquad |I_\beta|^2 \leq Q_{LL}Q_{RR} \qquad (1.14)$$
$$Q_{RR} + Q_{LR} + Q_{RL} + Q_{LL} = 1$$

A Monte Carlo integration technique combines the probability distributions from the muon decay observable measurements, assuming Gaussian distributions, and produces the probability distributions for the parameters in Eq. (1.13). The definition of the $Q_{\epsilon\mu}$ parameters is then used to set upper limits on the coupling constants $g_{\epsilon\mu}^\gamma$ except for g_{LL}^V. Only the measurement of inverse muon decay allows to separate the coupling constants g_{LL}^S and g_{LL}^V and provides a lower limit for the latter. The decay parameters ρ, δ and $P_\mu\xi$ in the global analysis provide stringent limits on the coupling constants g_{LR}^V, g_{RR}^S and g_{RR}^V.

1.3.2 Extended formalism for a non-local tensor interaction

The coupling constants g_{RR}^T and g_{LL}^T are set to zero in the general 4-fermion interaction (Eq. (1.1)) because their corresponding matrix element cancel out. However by abandoning locality [13], one can redefine the tensor interaction (Eq. (1.2)) such as:

$$\Gamma^T = \sqrt{2}\sigma^{\alpha\lambda}\frac{q^\beta}{q} \qquad (1.15)$$

where q_μ is the momentum transfer of some virtual boson. This form of the tensor interaction conserves the terms with g_{RR}^T and g_{LL}^T. The terms with g_{RL}^T and g_{LR}^T remain unchanged because of the identity:

$$\sigma^{\alpha\lambda}P_\pm \otimes \sigma_{\beta\lambda}P_\pm \cdot \frac{4q_\alpha q^\beta}{q^2} = \sigma^{\alpha\beta}P_\pm \otimes \sigma_{\alpha\beta}P_\pm \qquad (1.16)$$

where $P_\pm$ is the chiral projection operator. Furthermore the differential decay rate (Eq. (1.4)) is modified. The definition of the decay parameters changes to include the new coupling constants g_{RR}^T and g_{LL}^T. Assuming that this tensor interaction is the

same for quarks and leptons, the pion decay data provides constraints leading to:

$$g_{LL}^T = g_{RL}^T = g_{LR}^T = 0. \tag{1.17}$$

Therefore only left-handed (right-handed) neutrinos (anti-neutrinos) interact with this new tensor current. In this context the decay parameter the most sensitive to the tensor interaction is δ [14]. In particular if one assumes that all the coupling constants except g_{LL}^V and g_{RR}^T are equal to zero:

$$\delta = \left(\frac{3}{4}\right) \frac{1 - |g_{RR}^T|^2}{1 + 5|g_{RR}^T|^2} \approx \frac{3}{4}(1 - 6|g_{RR}^T|^2). \tag{1.18}$$

The final TWIST measurement of δ can provide stringent limits on this possible non-local tensor interaction.

1.4 Experimental status of δ and η

1.4.1 Previous measurements of δ

The final goal of the TWIST experiment is to measure the parameters ρ, δ and $P_\mu\xi$ with a precision of an order of magnitude better than the measurements prior to TWIST. The last pre-TWIST measurement of the parameter δ was performed by B. Balke *et al.* [15] in 1988 at TRIUMF. The experiment used a muon-spin-rotation technique to determine the parity-violation decay asymmetry as a function of the positron momentum. Their result was consistent with the Standard Model:

$$\delta = 0.7486 \pm 0.0026(\text{stat}) \pm 0.0028(\text{syst}). \tag{1.19}$$

The TWIST collaboration already published an initial result [16] and an intermediate result [17] which represented already a significant improvement over the previous measurement with the respective values:

$$\delta = 0.74964 \pm 0.00066(\text{stat}) \pm 0.00112(\text{syst}) \tag{1.20}$$

and

$$\delta = 0.75067 \pm 0.00030(\text{stat}) \pm 0.00067(\text{syst}). \tag{1.21}$$

These three measurements were performed on the M13 beamline at TRIUMF which provides highly polarized muons. Although the parameter δ can be measured from muons with a low polarization, a high polarization is desirable in order to increase the measurement sensitivity to this parameter.

1.4.2 Previous measurements of η

The parameter η is crucial to the description of muon decay because it has an influence on the momentum-angle and the polarization of the decay positron, and the decay rate. Furthermore the muon decay rate is used to determine the Fermi constant G_F. The Standard Model is most often assumed such as in the results of the MuLan [18] and FAST [19] experiments. Currently the precision on G_F is limited by the experimental precision of the muon decay rate measurement if the Standard Model is assumed ($\eta = 0$). However in a model independent approach, the relationship between the decay rate and the Fermi constant leads to:

$$G_F \approx G_F^{V-A} \left(1 - 2\eta \frac{m_e}{m_\mu} \right). \tag{1.22}$$

where G_F^{V-A} corresponds to the Standard Model assumption. In this approach the leading uncertainty is from the measurement of η. For instance using the uncertainty from the best direct measurement of η (in Eq. (1.25)) leads to an uncertainty on G_F 80 times larger.

The measurement of the parameter η from the momentum-angle spectrum shape is quite difficult because of the multiplying factor $x_0 \approx 10^{-2}$ which diminishes significantly the sensitivity to this parameter (Eq. (1.5)). This type of measurement of η was last performed by S.E. Derenzo [20] with a result of

$$\eta = -0.12 \pm 0.21. \tag{1.23}$$

The parameter η can also be determined by measuring the transverse polarization of the decay positron as a function of energy [6]. The results from the *direct*[2] measurements from the transverse polarization by Burkard *et al.* [21] and Danneberg *et al.*

---

[2]Along with their direct measurements, Burkard and Danneberg reported results from restricted and global analyses such as the one presented in Sec. 1.3.1. These analyses use further assumptions or the other decay parameters to constrain their η measurement. These results cannot be compared to the direct measurement presented in this thesis.

[22] are respectively:

$$\eta = 0.011 \pm 0.081(\text{stat}) \pm 0.026(\text{syst}) \tag{1.24}$$

and

$$\eta = 0.071 \pm 0.037(\text{stat}) \pm 0.005(\text{syst}). \tag{1.25}$$

Although less sensitive, a new direct measurement of η from the momentum-angle spectrum is a precious result complementary to the transverse polarization measurements.

1.5 Overview of the TWIST experiment

The TWIST spectrometer is composed of 56 wire chambers built with high precision (chapter 2); it is installed in a highly uniform 2 T solenoidal magnetic field. The muons from the M13 beamline stop in the center of the wire chamber stack in a target foil. The decay positrons traverse and ionize the gas in the wire chambers, triggering signals on various wires.

The analysis reconstructs helical tracks of the decay positrons from the signals on individual wires, or hits (chapter 3). An event selection algorithm identifies and selects the valid decay positron tracks (chapter 4). The reconstructed momentum and angle with respect to the z axis of the spectrometer are used to create a high statistics momentum-angle spectrum.

The experimental spectrum is fitted against a spectrum extracted from a Monte Carlo simulation of the experiment (chapter 5) to measure the decay parameters between the two spectra. The apparatus, the simulation and the analysis are carefully calibrated to high precision prior to the decay parameter measurement (chapter 6).

The fitting procedure extracting the decay parameters has a very low sensitivity to the η parameter. Furthermore the ρ and $P_\mu\xi$ are highly correlated with η. This is why η is fixed during the blind analysis for the extraction of ρ, δ and $P_\mu\xi$. A subsidiary analysis fitting the four parameters simultaneously was used to determine η only. For this reason the systematic uncertainties and corrections (chapter 7) and the results (chapter 8) are presented for each parameter separately.

The author's personal contributions to the experiment are detailed in appendix A.

Chapter 2

TWIST experimental setup and data

2.1 Experimental setup

Highly polarized positive muons provided by the M13 beamline at TRIUMF stop in a metal foil at the center of a spectrometer (Fig. 2.1). The spectrometer is composed of 56 wire chambers which measure at high precision the trajectory of the decay positrons. The spectrometer is installed in a superconducting solenoid contained in a steel yoke that increases the homogeneity of the magnetic field [23]. The muon beam position and direction are measured using a pair of time expansion chambers [24]. The resulting muon beam measurement is used as an input to the Monte Carlo simulation (MC).

2.1.1 Highly polarized muon beam

The TWIST apparatus is installed at the end of the TRIUMF M13 beamline (Fig. 2.2). The TRIUMF cyclotron produces a 500 MeV proton beam that travels in the proton beamline BL1A and collides with a carbon target. The protons have enough energy to overcome the electrostatic repulsion and reach the nucleus of the atom. The strong nuclear interaction produces a pair of quarks $d\bar{d}$ which leads to the conversion of a proton of the target into a neutron and a positive pion. Some of the pions stop in the production target and decay at rest with a mean half life of about 26 ns. The pions decay primarily into a positive muon and a neutrino. Due to conservation of
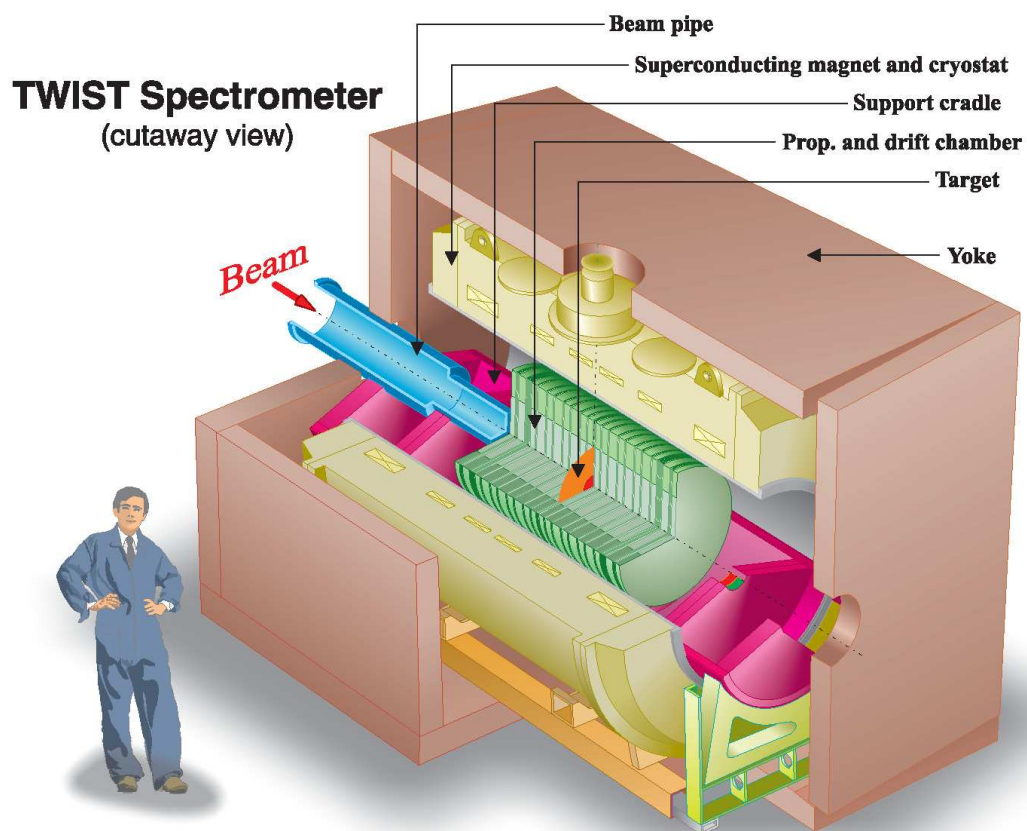
Figure 2.1: The different parts of the TWIST spectrometer are visible in this cutaway view.

momentum, the muon from a pion decaying at rest is emitted at:

$$p_\mu = \frac{m_\pi^2 - m_\mu^2}{2m_\pi} = 29.792 \text{MeV/c} \tag{2.1}$$
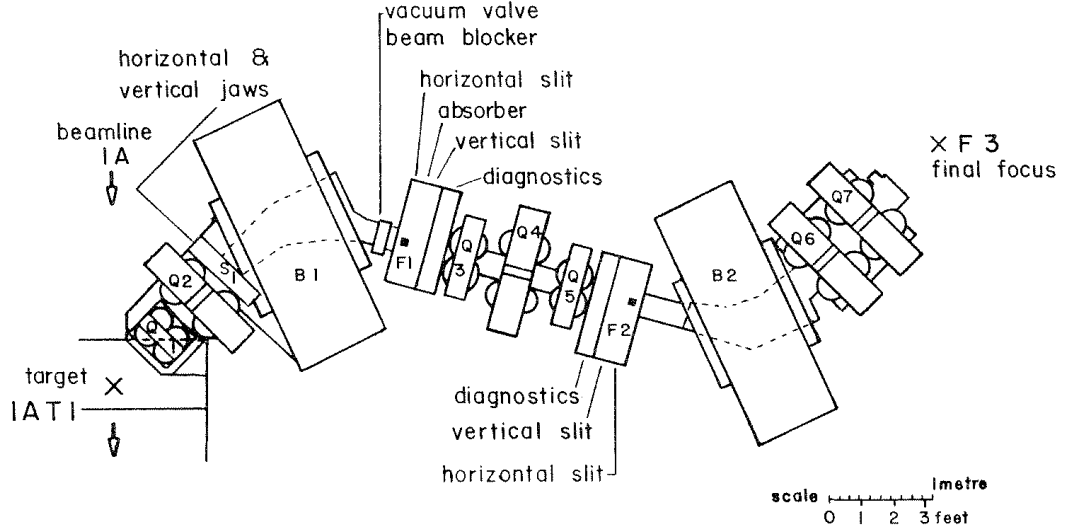
Figure 2.2: The momentum selection is performed by the B1 dipole and the horizontal slits between B1 and Q3. The total rate delivered to TWIST is controlled by the horizontal and vertical jaws upstream of B1.

The emitted neutrino has a left-handed helicity[1]. The conservation of angular momentum guarantees that all the muons emitted by pions have a left-handed helicity (Fig. 2.3).
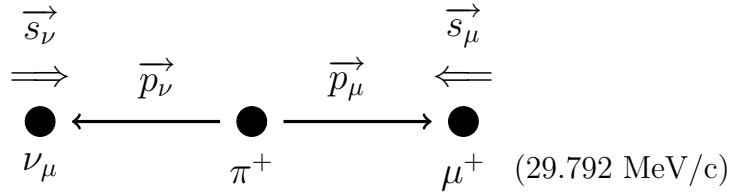
Figure 2.3: The pion decay into a muon and neutrino is the dominant decay mode. In the rest frame, the muon is emitted with a momentum of 29.792 MeV/c and with its spin opposite to its momentum.

The muons that are used by TWIST are produced close to the production target

---

[1] The neutrinos are not 100% left-handed in reality because they are not massless and because of the radiative decay of the pions: $\pi^+ \rightarrow \mu^+ \nu_\mu \gamma$. However these effects are below the 10^{-4} level and therefore can be neglected in our experiment.

surface. They undergo multiple scattering which changes the direction of the momentum but not the direction of the polarization before they reach the M13 beamline. The amount of multiple scattering undergone by the muons is a function of the amount of energy lost. Therefore the muons with a higher momentum have a higher polarization. The momentum selection of the M13 beamline is set to an average of 29.6 MeV/c (Fig. 2.4), slightly away from the kinematic end-point, to produce a beam of highly polarized muons at a useful rate. These muons are produced on the surface of the target in a depth of less than 16 μm and are consequently called surface muons.
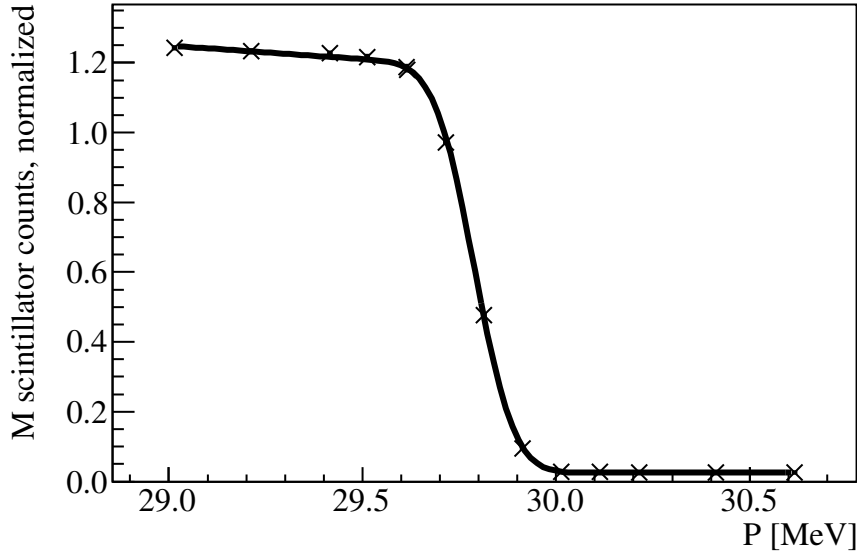
Figure 2.4: The beamline momentum selection is carefully calibrated before each data set by using the kinematic end point of the pion decay at 29.79 MeV/c. The rate in the main scintillator of the detector is recorded for various values of the B1 dipole current. The corresponding distribution is fit to extract the B1 setting providing a momentum selection centered on 29.6 MeV/c.

The beam has a contamination of "cloud muons" from pions decaying in flight between the production target and the dipole B1, as well as pions and beam positrons. The beam positrons originate mostly from muons decaying inside the production target, or in the surrounding materials. The time of flight is used to separate the surface muons from the cloud muons and the pions. A capacitive probe installed on the proton beamline defines the time of arrival of the protons on the target which is also the time of the pion production. The difference between the pion production time and the arrival of the secondary particles in the TWIST detector as measured by the muon counter (see Sec. 2.1.4) defines their time of flight. The beam positrons

cannot be completely separated from the surface muons and must be identified in the analysis (see Sec. 3.2.3). The typical muon rate was 2500 Hz in 2006 and 4300 Hz in 2007.

The M13 beamline was improved in early 2006 in order to adjust the position and direction of the beam in y. The direction of the beam in x and incidentally its position at the spectrometer can be adjusted using the dipole B2. The 2004 beam was not centered on the spectrometer axis, which was a source of depolarisation of the muon and a problem for the measurement of the $P_\mu\xi$ parameter [25]. Additional current sources were installed on the poles of the quadrupoles Q4, Q6 and Q7. The extra current is injected to only two of the coils of the quadrupole in order to break the symmetry of the magnetic field and effectively steer the beam in one direction. The steering from the quadrupoles and the B2 dipoles allows for a precise adjustment of the position and the angle of the beam.

2.1.2 Spectrometer

The spectrometer allows a high precision reconstruction of decay positron trajectories using the signals on the individual wires, referred to as hits, from 44 Drift Chambers (DCs). It also contains 12 Proportional Chambers (PCs) for particle identification. The chambers are installed symmetrically about a stopping target foil in which the muons stop (Fig. 2.5(a)). The wire chambers were designed to be low mass in order to reduce positron multiple scattering and to allow the muons to reach the target since it takes only about 1 mm of water equivalent to stop muons at 29.6 MeV/c. Furthermore the reduced multiple scattering facilitates the reconstruction of the decay positron tracks. The space between the chambers is filled with 97% helium also to reduce the multiple scattering. The remaining 3% of the gas is nitrogen to prevent high voltage breakdown on the module exteriors.

The wires chambers are installed in a support structure called the cradle. One crucial aspect of the construction of the spectrometer is the high precision positioning of all its components. In particular the distance between the wire chambers is controlled by high precision ceramic spacers of a Russian material known as Sitall. Pneumatic cylinders compress the stack of wire chamber Sitalls to mechanically stabilize position of the chambers for the whole run period. The Sitalls length is almost insensitive to the pressure from the pneumatic cylinders and to the temperature. The relative uncertainty on the 1 m long Sitall stack is less than 50 μm which means that

(a)

(b)
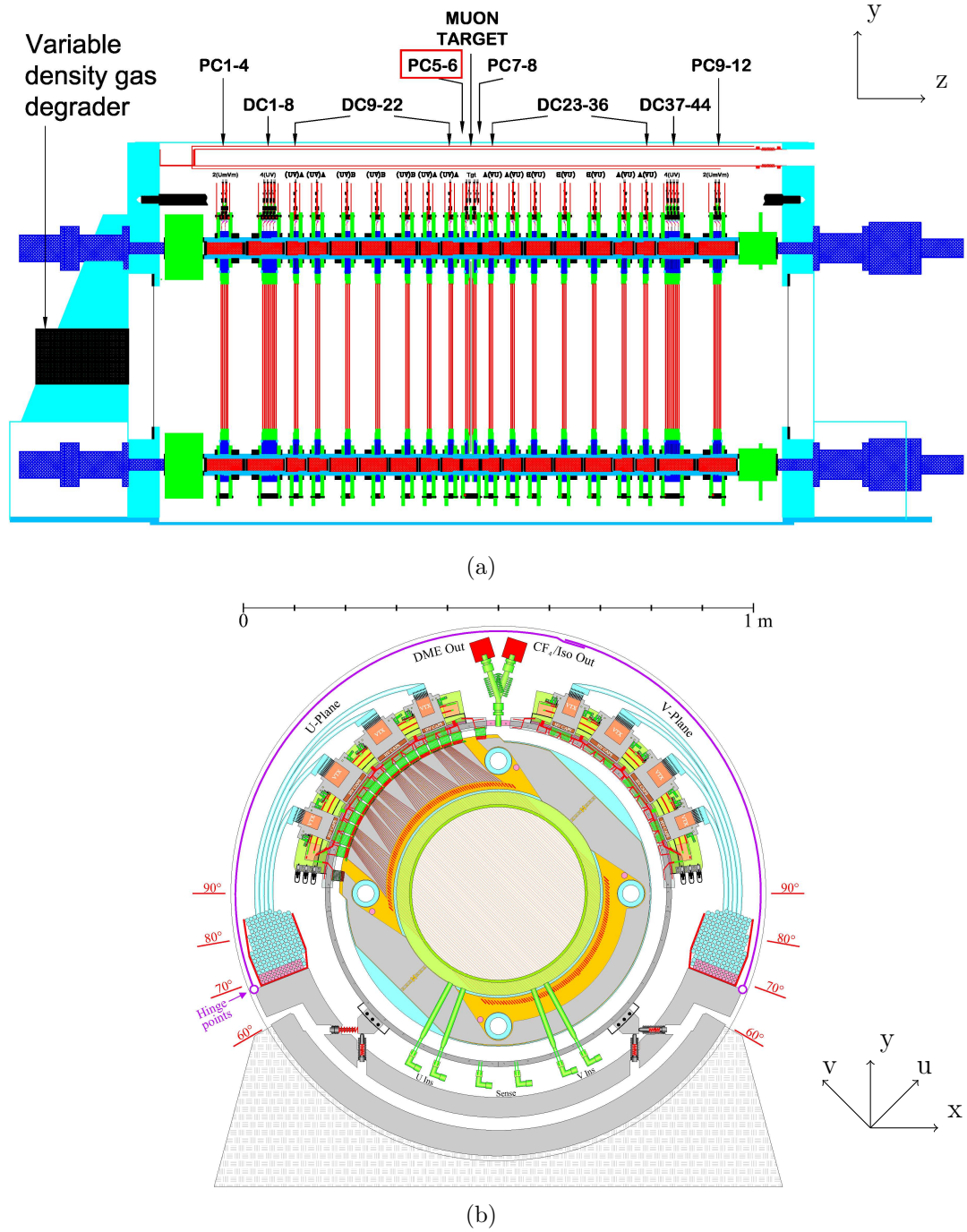
Figure 2.5: The side cross section of the detector (Fig. (a)) shows the 56 planar wire chambers installed symmetrically around the muon stopping target. A system of pneumatic cylinders keep precisely in place the chambers for the duration of the run period. The wires are oriented parallel to the u or v axis (u plane shown on Fig. (b)). The uvz coordinate system is equivalent to the xyz coordinate system rotated by $45°$ around the z axis.

the z positions of the chambers are known with a precision of a few μm [23].

Drift chambers

The drift chambers are made of 80 parallel wires separated by 4 mm and installed between 6 μm thick cathode foils of aluminized Mylar (Fig. 2.5(b)). The cathode-to-cathode distance is 4 mm as well. The wires and the cathode foils are installed on circular glass plates of 600 mm diameter with a very low coefficient of thermal expansion. The 320 mm separating the first and last wires of a plane expands only by 1.6μm/$^\circ$C.

In order to reduce gravitational effects on the chambers and therefore on the measurement, the wires are not oriented in the x and y direction but instead are oriented in the u and v direction. The uvz coordinate system is obtained by rotating xyz by 45° around the z axis. The u (v) planes measure the u (v) position of the positron track with their wires parallel to the v (u) direction.

The drift chambers are arranged into two groups referred to as the sparse stack and the dense stack. The sparse stack covers most of the tracking region and is composed of seven drift chamber modules on each side of the target. Each module is made of a u plane and a v plane with one cathode foil in common. The dense stacks installed at both ends of the spectrometer are extended drift chamber modules containing eight planes (with nine cathode foils) instead of two in order to reconstruct the longitudinal momentum of the decay positron with high accuracy. The z position of the sparse stack modules was modified for this measurement in order to reduce the degeneracies in the track reconstruction. (Fig. 2.6).

The drift chambers are filled with dimethyl ether (DME) gas which is a slow drift gas with a small Lorentz angle[2]. The reconstruction resolution defined by the σ of the drift distance residual distributions is about 50 μm across the entire drift cell. The high voltage on the wires was set at 1950 V to optimize the hit efficiency [23]. Efficiency measurements using beam positron tracks in zero magnetic field showed this operating voltage to be well into the proportional mode efficiency plateau.

The cathode foils on the outside of the chamber modules separate the DME gas of the chambers from the He-N mixture in the cradle. A differential pressure between these two gases leads to a bulge of the cathode foils. This bulge deforms the electric field line shapes in the drift chambers and therefore changes the relationship between

---

[2]The Lorentz angle is the angle between the drift field and the electron drift direction that occurs in a non-zero magnetic field.
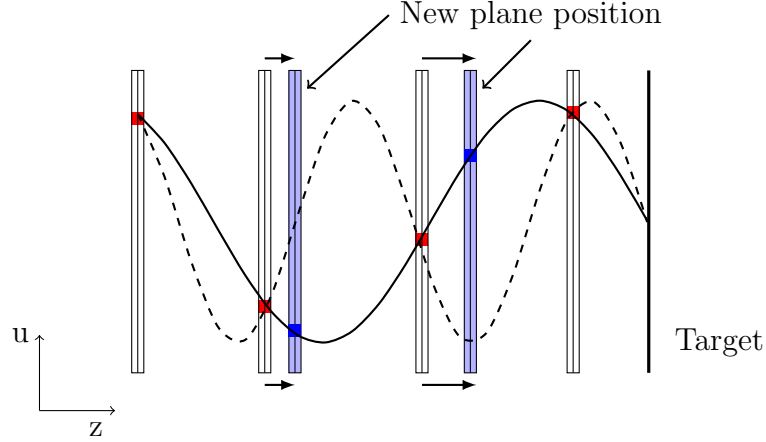
Figure 2.6: Several of the sparse stack DCs were moved prior to this measurement in order to reduce the degeneracies in the track reconstruction such as for this upstream decay. This schematic does not represent the actual geometry of the spectrometer.

drift time and drift distance which is a crucial element of the track reconstruction. For this reason the differential pressure between the inside and the outside of the chamber is regulated very precisely by the gas system, which controls the DME gas flow in the chambers. The calibration procedure used to determine the optimal differential pressure is detailed Sec. 6.1. Under stable ambient temperature conditions, the differential pressure and therefore the cathode foil bulge are kept constant by the gas system. The differential pressure transducer that measures the detector-cradle differential pressure is outside of the magnet volume, connected to the detector and cradle volumes by long tubes. A consequence of this is that if the difference in temperatures between the cradle and the experimental hall changes, this causes an artificial change in the measured differential pressure, which in turn causes the foils to bulge. This can happen if the temperature in the experimental hall changes too quickly. A 3 °C change in the differential temperature between the cradle and experimental hall results in a foil bulge of 35 μm [26]. Runs with a differential temperature larger than 3 °C are removed from the analysis.

The first stage of the electronic readout is composed of pre-amplifiers installed on the outside of the wire chambers in order to amplify the signal to transport it outside of the detector. Higher gain post-amplifiers complete the amplification before sending the signal to discriminators producing rectangular signals. The width of the rectangular signal corresponds to the time-over-threshold of the raw signal. The digitalization of the signal is performed by Lecroy 1877 FastBus Time to Digital

Converters (TDCs) which have a least significant bit of 0.5 ns [27]. The differential non-linearity between channels in one TDC is less than 0.1 ns and the non-linearity of one TDC is less than 25 ppm for full range [28]. The non-linearities in the acquisition system are further reduced by spreading the signals through multiple TDCs.

Proportional chambers

Besides the 44 drift chambers, 12 proportional chambers (PCs) are installed in the spectrometer for particle identification purposes. The proportional chambers offer a time response with most drift times less than 50 ns. These chambers have the same construction as the drift chambers with the exception that each chamber contains 160 sense wires separated by 2 mm. The cathode-to-cathode distance is unchanged at 4 mm. Instead of DME the proportional chambers are filled with CF_4/isobutane, which provides a fast response. The high voltage of maximal efficiency was determined using the same technique as for the DCs and found to be 2050 V. The electronic readout is the same as for the DCs.

The 12 proportional chambers are installed in three modules containing four chambers each. The target module is detailed in the next section. The upstream and downstream PC modules are installed at the extremities of the spectrometer. Their role is to detect the particles entering and exiting the spectrometer. The time-over-threshold of the hits in the PCs is crucial for the identification of the particles (see Sec. 3.2.3).

PC target module

The cathode foil separating PC 6 and PC 7 is the stopping target for the muons. In order to study the effects of the target material on the results, such as the muon depolarization, two different targets were used for the two run periods:

- 2006: high purity silver target, 99.999% silver, $(30.9 \pm 0.6)\mu$m thick

- 2007: high purity aluminium from the 2004 measurement, 99.999% aluminium, $(71.6 \pm 0.5)\mu$m thick

The targets cannot be installed like the aluminized Mylar cathodes because they are not flexible enough to be tensioned and stay flat. Instead the target is glued in the 110 mm diameter cutout of an aluminized Mylar cathode (Fig. 2.7). The superposition of the target material and the aluminized Mylar supporting it creates

sharp edges which are problematic for the operation of the PCs. For this reason Kapton masks with a central cutout of 110 mm are installed on all the cathodes of the target module. The masks limit the active region of the target PCs to the cutout in the center of the masks and only the 48 central wires of the PCs are instrumented. The silver epoxy glue ensures conductivity between the target and the aluminized Mylar. A third target was used at the end of the summer 2007 which did not use a Kapton mask for a special set of upstream stops data (see Sec. 5) to validate the MC. The details of this target and the corresponding data can be found in [29].
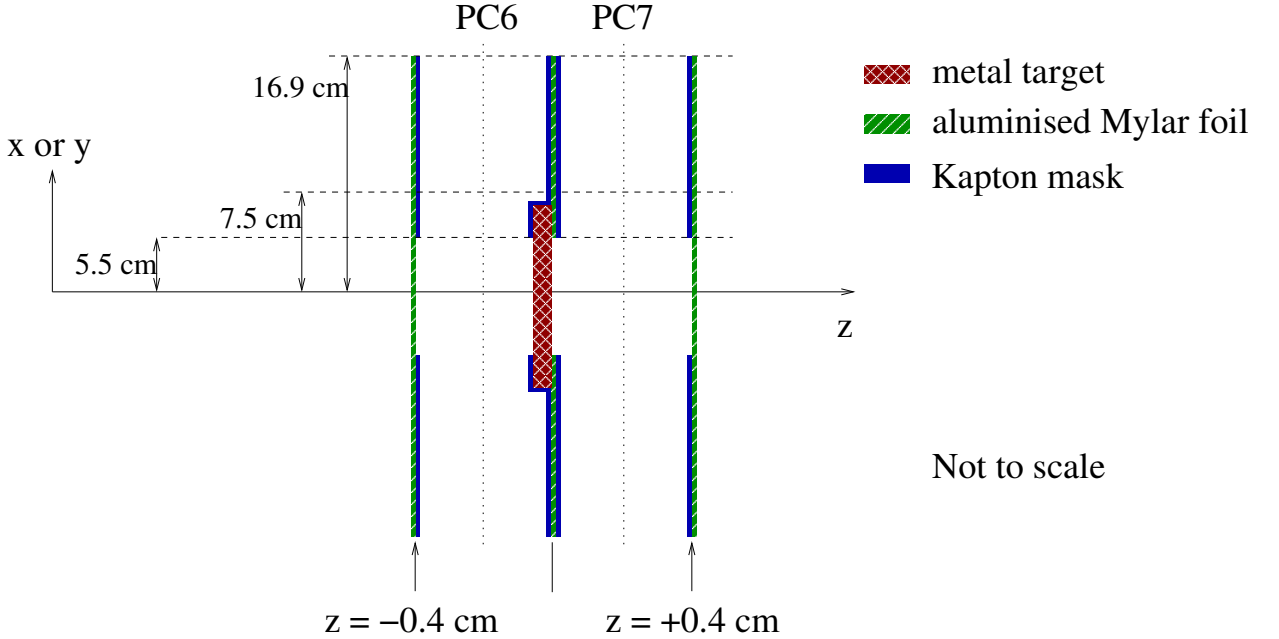
Figure 2.7: The target module is different from the two other PC modules. The stopping target acts as the cathode foil between PC 6 and PC 7.

The purpose of the PCs surrounding the target is to determine if a muon stopped in the target. A muon stopping downstream of the target creates a hit in PC 7 and is excluded during the analysis. Requiring a muon hit in PC 5 and 6 on the other hand is not sufficient to guarantee that the muon stops in the target since it does not exclude the stops in PC 6.

A Monte Carlo study showed that muons deposit different amounts of energy in PC 5 and 6 if they stop in the target or in the gas or a wire of PC 6 (see Sec. 4.2). In order to measure accurately this energy deposited using the pulse width[3], the voltage

---

[3]For technical reason it was not convenient to install an ADC (Analog to Digital Converter) unit to measure the integral of the hits in PC 5 and 6. The time over threshold or pulse width is a good approximation to the hit amplitude.

on PC 5 and 6 is lowered to 1600 V.

2.1.3 Superconducting solenoid and the yoke

The spectrometer is installed in the center of an Oxford Instruments superconducting solenoid cooled by liquid helium. The whole apparatus itself is inside a steel yoke with two circular holes (Fig. 2.1). The upstream hole allows for the muon entrance and the downstream hole is important for the symmetry of the magnetic field. The purpose of the yoke is to increase the uniformity of the magnetic field in the tracking region inside the spectrometer. The nominal data sets are taken with a magnetic field of 2 Tesla at the center of the spectrometer. Within the tracking region the magnetic field varies by less than 8 mT. Two NMR probes are installed on the cradle at each end of the spectrometer to measure the strength of the field during data taking with a precision better than 0.1 mT.

The z component of the magnetic field was measured with high precision using a Hall probe installed on a rotating arm. The resulting map granularity is not sufficient for the high precision track reconstruction. A finer magnetic field map was generated from a simulation of the solenoid and the yoke using the finite element software called `OPERA-3d` [30]. The measured map and the simulated map agree to within ± 0.2 mT over the drift chamber region.

2.1.4 Beam package and scintillators

The muons travel through the vacuum of the M13 beamline, which ends inside the yoke before the first chamber of the spectrometer. The end of the beamline is equipped with a "beam package" containing the muon counter (M counter), which is the trigger for the acquisition system. The two photomultipliers of the M counter are installed outside of the yoke and are connected to the scintillator by Plexiglas light guides. The signals from the two phototubes, M1 and M2, are linearly summed to form the signal M12. The thresholds of the electronic readout are set to provide the maximal efficiency on muons and the minimal efficiency on beam positrons. The muon trigger is defined by the coincidence M1*M2*M12. The muon trigger hit time is the earliest time between M1 and M2 and the signal from M12 is sent to an ADC to provide the amplitude of the hit.

The M counter scintillator is radially surrounded by the positron scintillator (PU scintillator) which is used in special analyses requiring the decay positron time such

as the calibration of the drift chambers wire time offsets (see Sec. 6.2). The PU scintillator measures only decay positrons upstream of the stopping target. For this reason a scintillator is installed downstream, outside of the yoke, and covers entirely the downstream hole in the yoke (See details in [31]). The electronic readout of the PU and downstream scintillators are set to have high efficiency on positrons.

The muon stopping distribution in the spectrometer is adjusted using the gas degrader installed in the beam package between the end of the M13 beam pipe and the M counter (Fig. 2.8). The gas degrader contains an adjustable mixture of He and CO_2 gas. The ratio of the two gases is modified to change the density inside the gas degrader consequently changing the amount of material traversed by the muon. The room temperature and the atmospheric pressure also affect the density. An online analysis of 3% of the data provides a measurement of the muon stopping distribution from the target PCs occupancy and a feedback loop adjusts automatically the gas mixture to keep the stopping distribution stable during the duration of the data set.
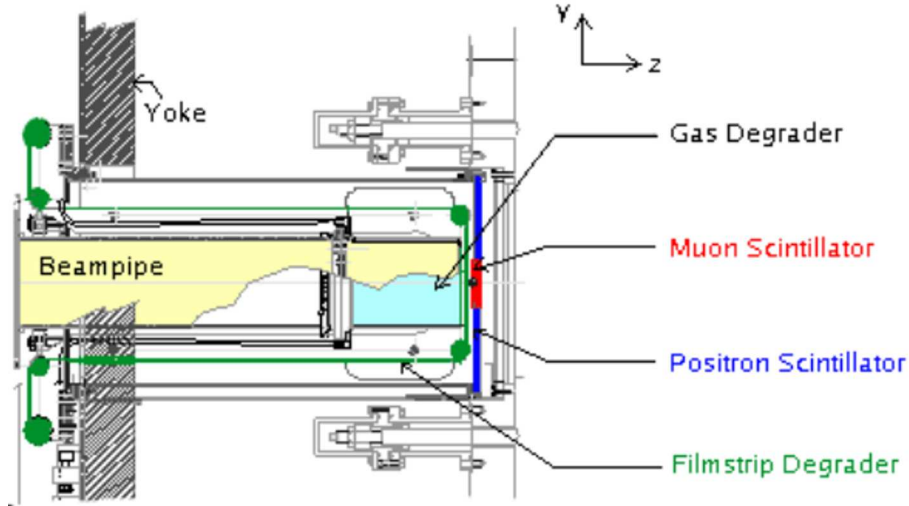
Figure 2.8: The beam package assembly includes the muon counter and the PU scintillator as well as their respective photomultipliers. It also contains the gas degrader which adjusts the stopping distribution of the muons in the spectrometer.

2.1.5 Time expansion chamber (TEC)

The TEC, as it will be referred to in this thesis, is actually composed of two time expansion chambers measuring in series the position and the emittance of the muons in the beam. The first chamber measures the x coordinates of the beam while the

second chamber measures y. Both chambers are installed in a "gas box" which is filled with DME gas at a constant pressure of 80 mbar (Fig. 2.9). The gas box is installed in the vacuum of the M13 beamline close to the final focus point of the beam (Fig. 2.2). The DME gas is operated at low pressure in order to reduce the multiple scattering undergone by the muons. The low pressure also reduces the tracking efficiency for the beam positrons. Although the TEC was designed to be low mass, the 6 μm thick aluminized Mylar windows separating the DME gas from the vacuum are sources of significant multiple scattering. For this reason the TEC is installed only at the beginning and the end of each data set.

The two main components of a TEC module are the drift region and the sense wires. The muons travel through the drift region and ionize the DME gas (Fig. 2.10). A drift cathode and a series of drift field wires surrounding the drift region create an electric field perpendicular to the z axis. In the first module the electrons drift toward negative x and in the second module toward positive y. The electrons are consequently guided toward a multiplication region made of sense wires (anodes) at 1150 V installed between a cathode grid plane and a cathode plane. In this region the drift electrons accelerate and ionize the DME gas further creating a situation of avalanche. A sense wire plane (one per module) is composed of 24 wires separated by 2 mm. The drift region is contained between the drift cathode and the cathode grid plane which are separated by 60 mm creating an effective active area of 60 mm $\times$ 60 mm $\times$ 46 mm for each module. The typical drift velocity in the drift region is about 10 mm/μs. The aging of the sense wire planes decreases their efficiency. The sense wire planes were changed twice during the 2006 run period and three times during the 2007 run period. The rapid aging of the sense planes is blamed on the sparking occurring in the TEC modules.

The signals on the sense wires go through the same electronic system as the signals from the drift chambers in the spectrometer. The measured drift distances are used to reconstruct the projected straight tracks in x and y separately in the two TEC modules. The reconstruction algorithm detailed in [31] identifies the muon tracks and removes isolated hits generally coming from overlapping beam positron tracks which have a much lower efficiency in the TEC. For each hit the drift time is converted into a drift distance according to the space time relation of each wire. The measurement of these space time relations along with the other calibrations of the TEC are detailed appendix C.
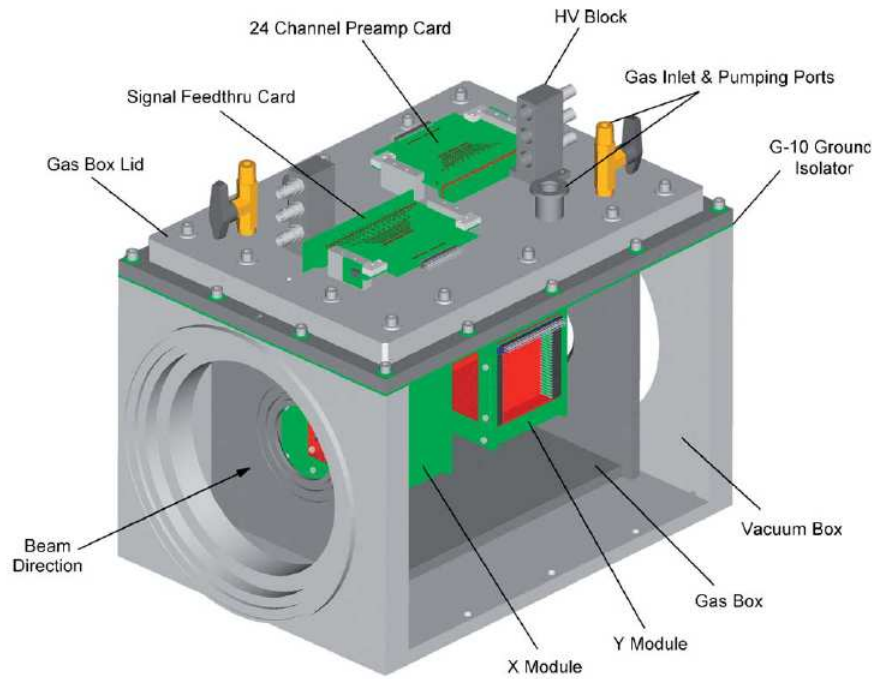
(a)
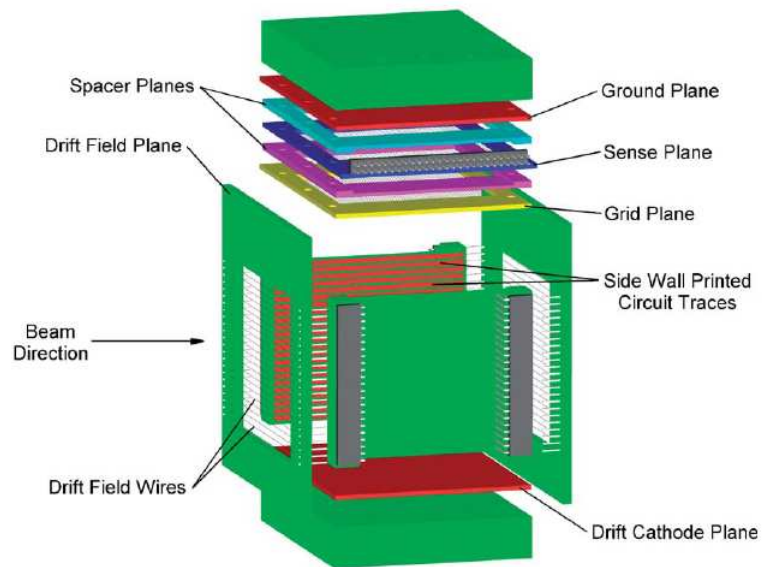
(b)

Figure 2.9: Two time expansion chambers are installed the gas box (Fig. (a)). The gas box and the TEC electronics are removed from the vacuum box for nominal data measurement. The vacuum box is a permanent element of the M13 beamline. Both time expansion chambers are identical and measure respectively the x and y directions (Fig. (b)).
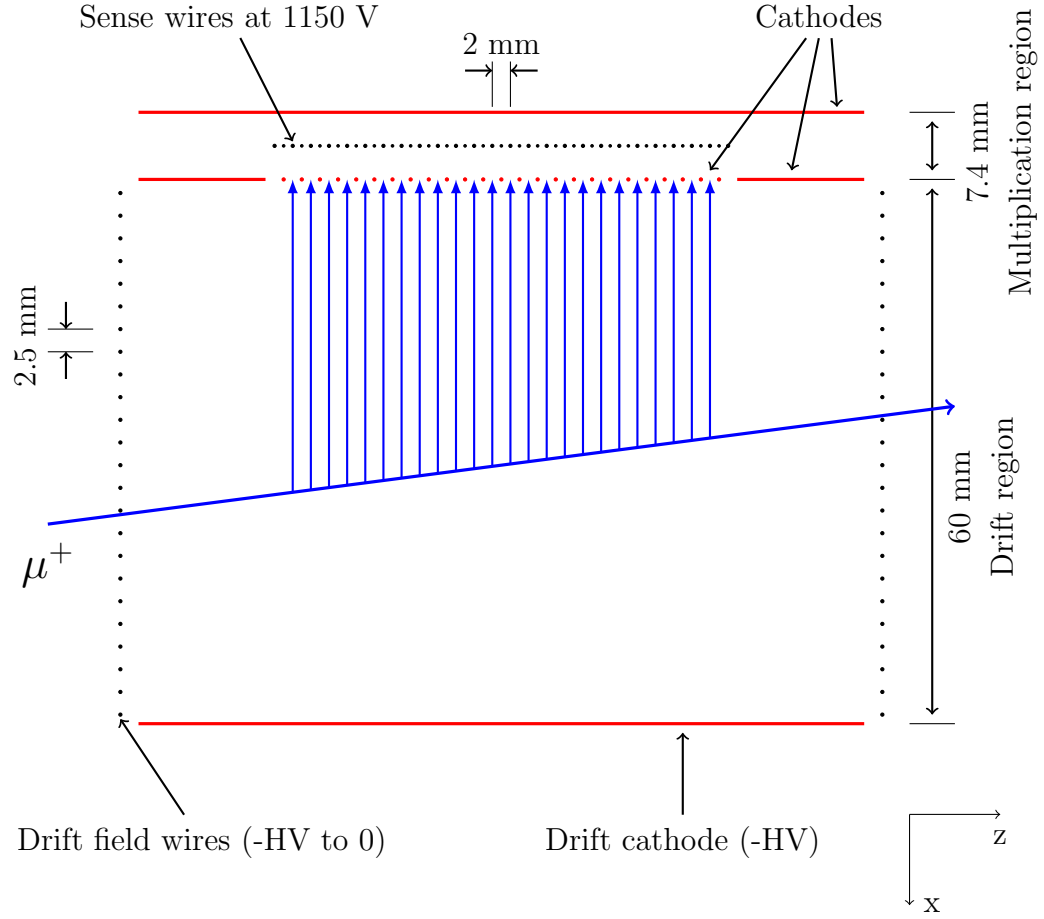
Figure 2.10: Typical event in the x time expansion chamber. The muon ionizes the DME gas and the free electrons produced drift toward the sense wires because of the drift field created by the drift cathode at a high voltage (HV) of 1000 V. The sense wires are separated by 2 mm with a shield wire in the interval to isolate them from each other.

2.2 Experimental data

The data are stored in files of 2 GB maximum. Each run is typically taken in 9 minutes. The running conditions are kept constant generally for six consecutive days between two cyclotron maintenance days. A data set is defined for each running condition and contains about 900 runs (see Tab. 2.1). Each nominal run contains about 8×10^9 events.

Individual runs to be analyzed are selected to ensure stable conditions for the data set. The stability of elements such as the M13 beamline or the temperature in the cradle are guaranteed for the selected runs. The number of discarded runs represents

between 10 and 30% of the data set.

The nominal sets (74, 75, 84, 87) are taken with optimal conditions for the measurement of the decay parameters. All the components of the experiment are set to their nominal value. Set 68 is almost nominal except for the muon stopping distribution which is peaked 1/3 into the target in the z direction.

The spectrometer is designed to be highly symmetric around the stopping target. However the upstream beam package, which represents a significant amount of material is not mirrored downstream. The decay positrons backscatter in particular on the scintillators of the beam package. The backscattered decay positrons create a second track overlapping in z and in time with the original decay positron track. These backscatter events are the source of track reconstruction confusion. Set 83 was taken with a downstream beam package installed. This second beam package mirrors the upstream beam package. This data set is used to test the consistency of the results with or without a symmetric apparatus.

Two sets (70 and 71) were taken with different solenoid magnetic field strength to test that the decay parameters measurement is consistent for same momenta measured at different radii. In particular these sets test that the decay parameters are insensitive to a change in the physical hit position in the chambers which modifies the effects of the degeneracies.

The set 72 was taken with the TEC in place in the beamline contrary to all the other sets for which the TEC was installed only at the beginning and the end to characterize the beam. The stability of the muon beam position and angle was monitored with the TEC in place for 6 days. This set was also used to test the effects of extra multiple scattering of the muon beam on the parameter $P_\mu\xi$ through the depolarization of the muons.

The parameter $P_\mu\xi$ is also very sensitive to the position and direction of the muon beam as it enters the fringe magnetic field between the TEC and the yoke. The muon beam was steered off the detector axis with an angle $\theta_y \approx$30 mrad for set 76 and with a position $x \approx$-1 cm and an angle $\theta_x \approx$-10 mrad for set 86. These sets are used to validate the depolarization in the fringe field in simulation.

The M13 beamline momentum selection was set at a value lower than the nominal value of 29.6 MeV/c to validate the correction on $P_\mu\xi$ due to the multiple scattering in the production target. The momentum selection was set at 28.75 MeV/c for set 91 and 28.85 MeV/c for set 92 and 93.

A special set of data referred to as far upstream stops are used to validate the

simulation (see Sec. 5.5). The momentum selection is changed and a degrader film (Fig. 2.8) is installed in the trajectory of the muons so they stop in the upstream PCs. Two sets (73 and 80) used the nominal targets. The set 89 used the modified large aluminium target to eliminate the effect of the Kapton mask on the decay positrons [29].

Set	Stopping target	Conditions	Number of good runs
68		Nominal centered at 1/3 of the target	619
70		Magnetic field 1.96 T	855
71		Magnetic field 2.04 T	771
72	Silver	TEC installed	979
73		Far upstream stops	363
74		Nominal	549
75		Nominal	838
76		Muon beam off-axis	689
80		Far upstream stops	209
83		Downstream beam package installed	974
84		Nominal	847
86	Aluminium	Muon beam off-axis	1192
87		Nominal	908
91		Low momentum at 28.75 MeV/c	241
92		Low momentum at 28.85 MeV/c	316
93		Low momentum at 28.85 MeV/c	533
89	Large aluminium	Far upstream stops	605

Table 2.1: List of data sets used for the final TWIST measurement. The sets are listed in chronological order except for set 88 which was divided into the sets 91, 92 and 93 during the analysis because the running conditions changed. The "good runs" are the runs selected for the analysis. The set numbers are not contiguous because of rules of nomenclature or sets being irrelevant for this analysis. No nominal set was discarded from the analysis.

Chapter 3

Analysis

The analysis converts raw hit information from the wire chambers into physics observables and eventually the muon decay parameters are measured from the momentum-angle spectrum of the decay positrons. The spectrum cannot be used to extract the decay parameters directly since it includes the detector response as well as the reconstruction efficiency. For this reason the analysis strategy of the TWIST experiment includes a full Monte Carlo simulation (MC) of the detector. The MC and the experimental data output files have the same format in order for them to go through the same analysis procedure in parallel. This procedure is summarized in the Fig. 3.1.

The goal of the first part is to reconstruct the event properties and the decay positron tracks. The event reconstruction software called MOFIA extracts the hit information from the data files, identifies the particles present in the event and fits all the potential decay positron tracks in a two stage track reconstruction.

In the second part of the analysis the information stored in the MOFIA output is used to identify valid events and decay positron tracks and include them in the momentum-angle spectrum. This section of the analysis includes the momentum calibration algorithm, which corrects for differences in the detector response of the experimental apparatus and the MC. Finally the MC spectrum is fit to the experimental spectrum to measure the difference in terms of muon decay parameters. This relative measurement has many advantages. The biases from the event and track reconstruction are included in both spectra and therefore cancel out in the fit of the difference. As a result, most of the systematic uncertainties arise from the inaccuracies in the simulation of the detector geometry and physics processes. The analysis method also facilitates a blind analysis.

Figure 3.1: In the TWIST analysis scheme the experimental and the Monte Carlo data go through the same event and spectrum reconstruction software. The experimental data undergo a second pass at the spectrum reconstruction in which the results of the momentum calibration are applied. The muon decay spectrum fit only measures the difference between the spectra in terms of muon decay parameters changes. The absolute values of the muon decay parameters are known only once the hidden decay parameters used to generate the Monte Carlo events are revealed.

3.1   Blind analysis

To minimise human biases, the decay positrons are created in the MC according to a momentum-angle spectrum generated by an independent server [32][33]. Hidden parameters are selected within a range of $\pm 10^{-2}$ away from the Standard Model prediction by this server and immediately encrypted. The key necessary to reveal the parameters is in a safe managed by TRIUMF administration staff for the entire duration of the analysis.

The server uses a Monte Carlo acceptance-rejection method to produce pairs of $(|\vec{p}|, \cos\theta)$ according to the probability distribution function defined by the hidden parameters and the differential decay rate (Eq. (1.4)). These samples are used in the MC of the detector as the initial kinematics of the decay positrons.

3.2   Event reconstruction

3.2.1   Data run unpacking

The analysis starts with the unpacking of the information stored in the run data files. The file contains, for each event, the list of times of the leading and trailing edges (see Fig. C.5), as they were measured by the TDCs. Each leading and trailing edge is associated with a channel number describing from which wire it originates. MOFIA associates trailing and leading edge from the same wire to create hits with a starting time and a time over threshold also called TDC width as well as a wire chamber number and a wire number. The zero time offset calibration (see Sec. 6.2) is applied here to correct the hit times just as they are extracted from the data files. The hit times are defined relative to the muon counter. The event window extends 6 μs before and 10 μs after the muon counter recorded hit. Only the leading and trailing edges contained within this event window are recorded. Errors in the unpacking such as a missing leading or trailing edge are closely monitored since they could potentially introduce analysis biases.

3.2.2   Crosstalk signal removal

The signal of a hit on a channel of a wire chamber can create fake signals on neighbouring channels. These so-called crosstalk signals create extra hits which eventually confuse the track reconstruction and reduce its efficiency. The crosstalk signals have a
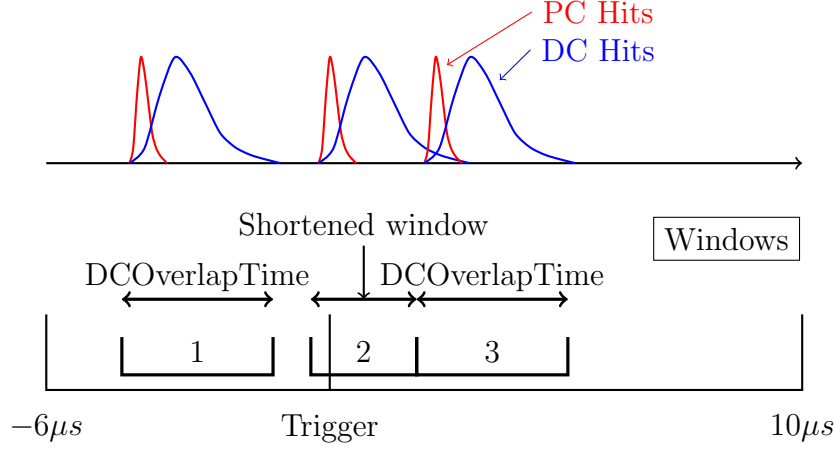
Figure 3.2: This typical event is composed of an early beam positron (window 1), a muon triggering the event (window 2) and a decay positron (window 3). The windows 1 and 3 are of length *DCOverlapTime*. The window 2 stops at the beginning of the window 3.

typical signature. They happen shortly after the real hits on adjacent wires and they have a narrow TDC width. An algorithm identifies the crosstalk signal and removes it before the beginning of the event analysis. A hit on a DC (PC) with a TDC width less than 50 (40) ns and with a coincidence interval with another adjacent hit of less than 40 (60) ns is identified as a crosstalk hit and removed. The crosstalk signal is not simulated in the MC simulation. For this reason the crosstalk removal is disabled for the analysis of MC data.

3.2.3 Event identification

At this stage, called the classification, the analysis contains only the list of hit times which occurred during the 16 μs of the event. Due to the drift time in the wire chambers, the hits from a particle are spread in time. The longest drift times are up to 100 ns in the PCs and 1000 ns in the DCs. Time windows are defined to group the hits from one particle or more. The hits in the window are subsequently analysed to identify the associated particle. Finally the event is classified depending on the number of windows and the type of particles identified.

The hits from a typical event are shown Fig. 3.2. This example consists of a beam positron followed by a muon triggering the event. The muon decays upstream about 800 ns after its arrival.

The PCs are used to detect the presence of a new particle in the spectrometer and therefore define the beginning of most time windows. In some rare cases a particle does not trigger any PC and the classification must decide to create a window based on DC information only. In our example the PC hits lead to the creation of three time windows. The length of a window is by default defined by the parameter $DCOverlapTime$. The window starts 50 ns before the first PC hit and the parameter $DCOverlapTime$ is set at 1000 ns in order to include all the DC hits in the window. However if a second particle appears before the end of window, the window time is shortened. This is referred to as a DC overlap. In Fig. 3.2 the decay positron appears 800 ns after the beginning of the muon window. The latter is shortened and eventually some of the hits from the muon might end up in the decay positron window.

The hits from the different particles are now grouped into time windows. The next step is to identify the type of particles associated with each window. A wide range of observables are used. Once more the PCs play a dominant role. The time of the PC hits as well as their corresponding time-over-threshold (TDC width) are used. In the example the muon and positrons can be identified using the difference in TDC width of their PC hits. The spatial distributions of the hits in u, v and more importantly in z are used as well. The decay positron leaves PC hits only on one side of the target while the beam positron leaves them on both sides. A window type describing the particle content is assigned to each time window. The list of window types is in the appendix B.1.

Finally a given set of window types defines the event type. The start time of the windows is also used in order to identify the events with DC overlap like in Fig. 3.2 in which muon and decay positron windows overlap. In the case of an upstream decay the positron and extra muon hits in the window are on the same side of the target and are analyzed together by the track reconstruction algorithm reducing its efficiency. The example Fig. 3.2 contains a beam positron (window type 4), a muon (window type 1) and an upstream decay positron (window type 2) overlapping in time with the muon window. It is therefore classified as a "Time DC overlap" event (event type 4). The complete list of event types is in the appendix B.2.

During the classification, the hits are analyzed to create hit clusters. A hit cluster groups hits from adjacent wires for each window and each pair of planes. The u and v plane hits together with the z position of the center of the pair of plane, define completely the position of the cluster in three dimensions. The width of the cluster

is defined by the wire spacing. This clustering of the hits is performed between the definition of the windows and the event types because the clusters are used in the latter.

In the case of time overlap of hits from different particles, multiple possible associations of the u and v hits lead to "ghost" clusters (Fig. 3.3). These "ghosts" clusters are eliminated during the "first guess" reconstruction because they do not produce consistent particle tracks.
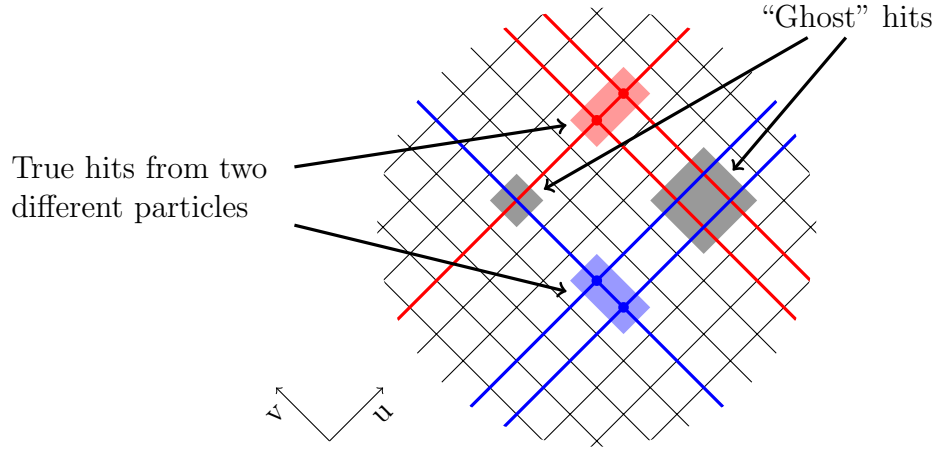
Figure 3.3: Hit clusters formation. Two adjacent wires with a hit are grouped together. The u and v hits are associated to have the u v position of the clusters. In the case of time overlap of two tracks, ghosts clusters appear.

3.2.4   First guess

The first stage of the track reconstruction referred to as the "first guess" has the task of identifying the list of hits belonging to the same track, as well as estimating the momentum and angle of the track candidates. The algorithm is capable of extracting multiple tracks in one time window. This feature is fundamental in the case of window types such as 14 or 15 which contain the decay positron as well as a beam positron. Multiple tracks can also appear from a single decay positron if it undergoes a hard scatter in the detector which "breaks" the track (Fig. 3.4).

The "first guess" obtains from the classification a list of hits and associated clusters for each window. In order to reduce computation time, only window types containing decay positrons are analyzed. The drift time information is ignored in the "first guess". For this reason DC and PC hits are used and handled in the exact same
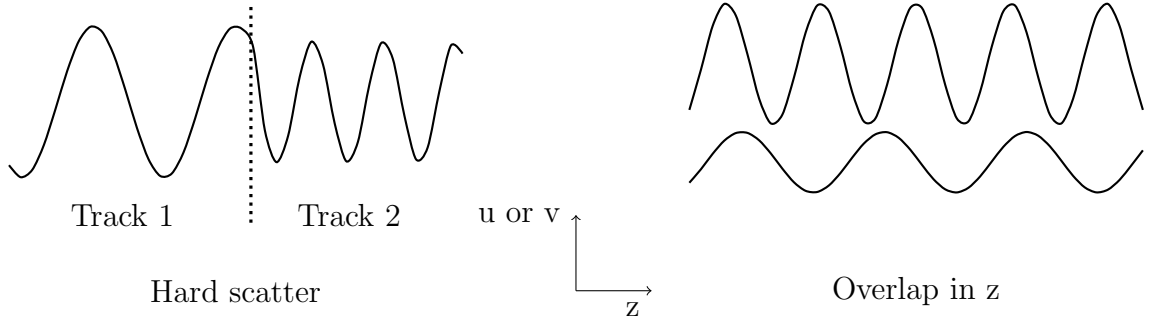
Figure 3.4: The "first guess" reconstruction algorithm is designed to deal with multiple tracks originating from hardscatters or from the superposition in time and in z of two particles.

way. Their position is defined on the wire they triggered. In this context the hit position distribution around the wire does not correspond to a Gaussian, but to a uniform distribution in the square u-v cell. In consequence the track candidate "goodness" is not evaluated using the standard χ^2 fitting function since it relies on Gaussian distributed residuals. Instead the "first guess" uses a parameter called the Chebychev norm which suits the reconstruction of tracks in wire chambers. This is equivalent to a maximum likelihood for uniform error distributions [34].

The clusters in the decay window are ordered according to their z position. The "first guess" analyses iteratively the list of clusters and shortens the list until it finds a track candidate. Using shorter list of clusters effectively changes the range in z onto which the algorithm searches for a track in order to find tracks broken by hard scatters.

Each list of hit clusters goes through the following algorithm until a track candidate satisfies cuts on the Chebychev norm. The first step is to fit a circle to the u-v projection of the clusters (Fig. 3.5). The circles formed by all possible combinations of three hits are calculated. The Chebychev norm of all the hits close enough to the circle is calculated. The circles are ordered by decreasing values of the Chebychev norm. The second step takes care of the z coordinate. The phase of the helix candidate at the first and last cluster is calculated and the series of possible winding numbers are fit (Fig. 3.6). Once again a Chebychev norm is calculated for the hits close to the track. The first track candidate passing the cuts on the circle and winding number Chebychev norms is stored as a track candidate. The hits close to the track candidate are included in the track data structure and removed from the list of hits in the window. The algorithm restarts with the new list of hits if it contains at least

four hits to find other track candidates.

The "first guess" algorithm was improved since the previous TWIST measurement by adjusting the cuts on the Chebychev norm of the circle and phase of the track candidate. The "first guess" now includes:

- a radius dependent cut on the circle Chebychev norm

- a $\cos\theta$ dependent cut on the phase Chebychev norm

- a reduction of the possible winding numbers in the phase search

The values of the cuts were chosen to maximize the reconstruction efficiency of the "first guess".

For each track the list of hits associated with the track, the radius of the helix in u and v, the frequency and the phase in z are passed to the second stage of the track reconstruction.

3.2.5 Helix fitter

The second and last stage of the track reconstruction is the helix fitter. It uses the "first guess" results as a starting point and refines the helix fit.

The helix fitter minimises the residuals at each DC plane using a least squares method. The minimization function also includes kinks in the helix that take into account the scatter of the positron as it goes through significant amount of material such as the DC chambers. The χ^2 function is given by:

$$\chi^2 = \sum_{\text{hits}} \frac{(d_f - d_m)^2}{\sigma_d^2} + \sum_{\text{kinks}} \frac{\theta_k}{\sigma_k} \tag{3.1}$$

where d_f is the drift distance of the fitted hit position, d_m is the measured drift distance, σ_d is the drift distance resolution for the fitted hit, θ_k is the kink angle and σ_k is the width of the kink distribution.

The kink approach is well-adapted to the TWIST spectrometer since the scattering masses are discrete [35]. The kinks on the track are allowed at the central cathode foil of each pair of DC planes as well as at the cathode foil in the middle of the dense stacks. There are no limits on the values of the kink however they are constrained in the fit through the χ^2 minimization. The value of σ_k in equation (3.1) is calculated using the formula for multiple scattering through small angles [36].
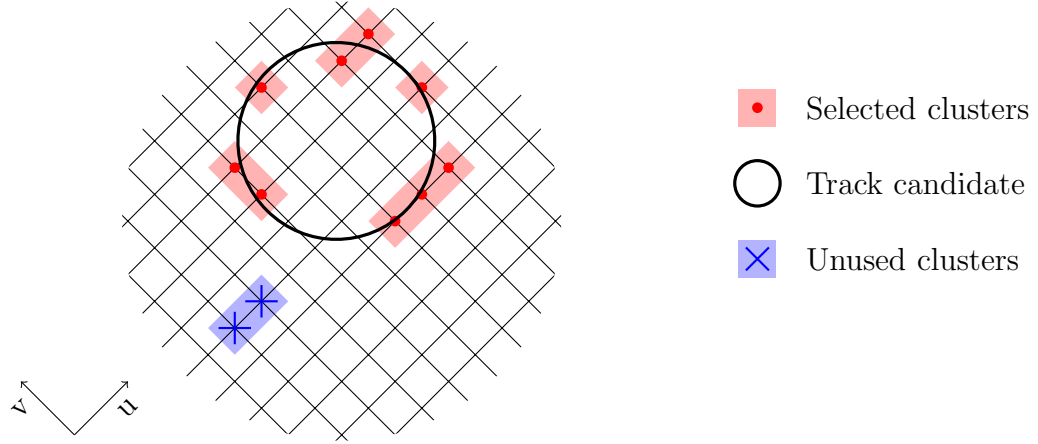
Figure 3.5: The u-v projection of the hits is fit with various circles from various combinations of three hits. The Chebychev norm is calculated only for the hits or clusters with small enough residuals.
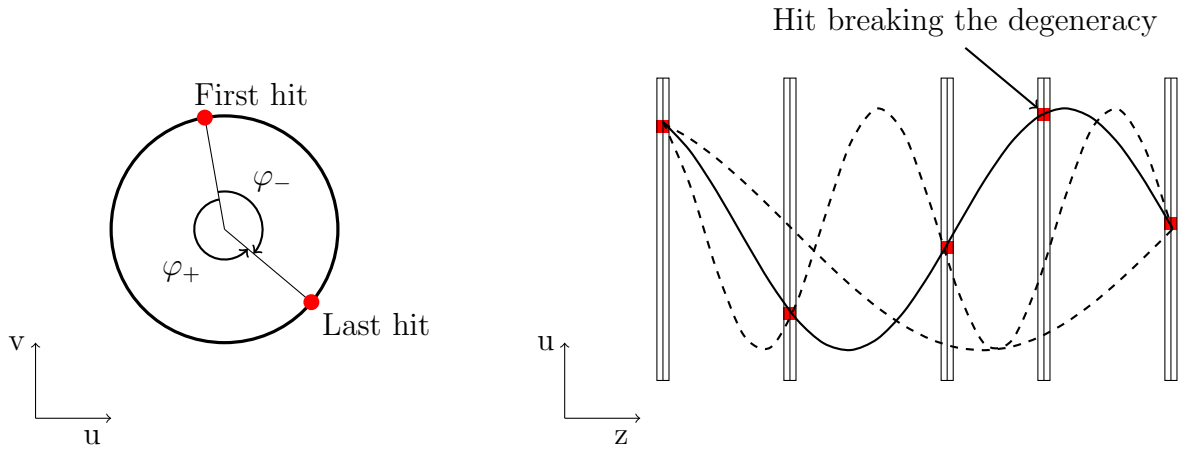
Figure 3.6: Second step in the "first guess" algorithm. The angular difference between the first and the last hit is $\varphi \pm 2\pi k$ with k an integer (left diagram). The diagrams are in two dimensions but the algorithm works in three dimensions. This stage of the reconstruction software is vulnerable to degeneracies in the winding numbers. Negative and positive charge tracks are evaluated in parallel (φ_-, φ_+).

The trajectories between the DC chambers are calculated using the OPERA field map to take into account the inhomogeneities of the solenoid magnetic field. The algorithm uses an arc step approximation with variable size step to integrate the magnetic field features.

The helix fitter must resolve the right-left ambiguity, which refers to the difficulty of determining on which side of the wire the particle traveled. The narrow window analysis described in [34] restricts the allowed position of the hits and resolves most of the right-left ambiguity using the hit clusters and the track angle from the "first guess" (Fig. 3.7).
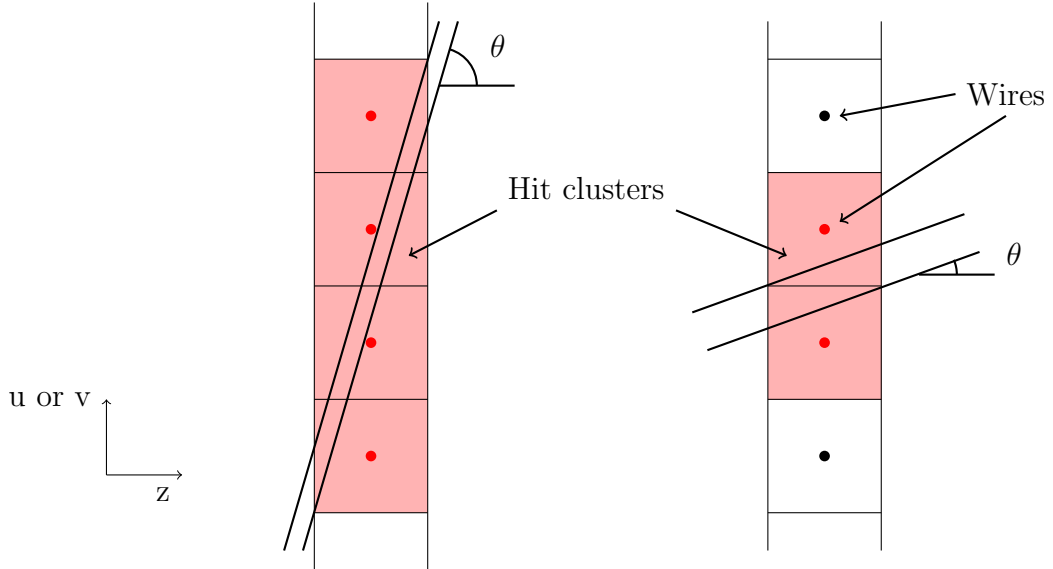
Figure 3.7: In the case of clusters containing more than one hit, the track is contained within a narrow window. This narrow window is defined by the two extreme possible rays with the track angle from the "first guess" and going through all the drift chamber cells with a hit. This narrow window is fundamental to resolving the right-left ambiguity.

For each hit in the DC chambers, the helix fit has the absolute recorded time of the hit as well as the position of the corresponding wire. The algorithm calculates the drift time from the difference between the ionization time and the recorded hit time. The ionization time corresponds to the time at which the particle is in the chamber and is calculated using the muon decay time and the time of flight of the decay positron from the target to the DC. The muon decay time is a free parameter of the helix fit to achieve a precision higher than the PCs.

The drift times are converted into drift distances using a Space Time Relation-

ship (STR) table. The STR table defines the isochron map of the drift times. The helix fitter uses the closest distance between the track and the wire to determine the position of the hit on the isochron (Fig. 3.8). This approach is motivated by the discrete ionization of the gas in the DC all along the particle trajectory with the closest ionization to the wire defining the hit start time. The STR tables for this TWIST analysis were derived from the decay positron tracks to improve the reconstruction (see Sec. 6.3).
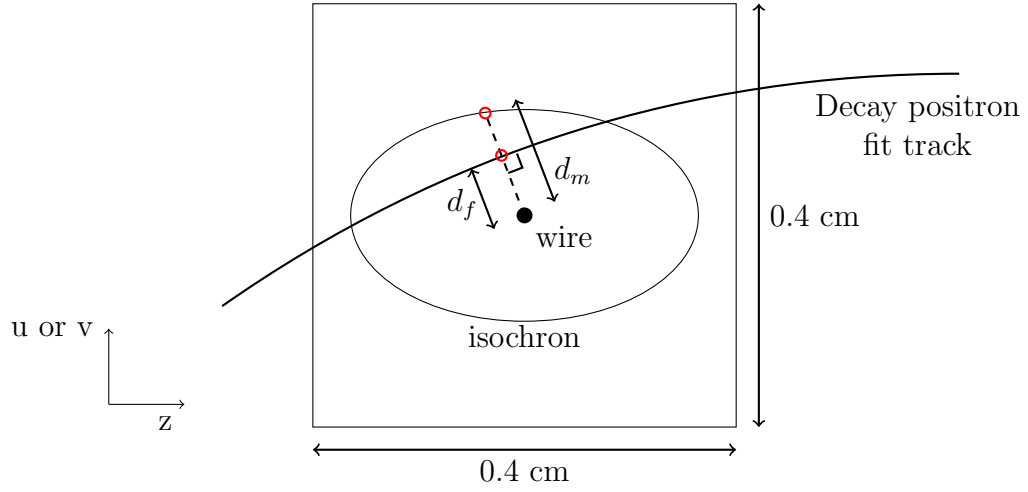
Figure 3.8: Calculation of the drift distances d_f and d_m for the χ^2. The tangent to the positron track in used in the context of the closest distance of approach. Only the isochron of the measured drift time is drawn here. The difference $|d_m - d_f|$ is the residual for the hit.

The drift distance resolution σ_d was set at the constant value of 100 μm during the previous TWIST analyses. A more realistic resolution dependent on the drift distance was implemented for this analysis (see Sec. 6.3).

Beside scattering, the particle also loses energy by ionization in the material as it travels through the detector. For this reason the helix radius and pitch change between the first DC and the last DC. This effect is taken into account in the fitting procedure:

$$\Delta E = \frac{1}{\cos \theta} \sum_i l_i \epsilon_i^{ion} \tag{3.2}$$

with ΔE the average energy loss of a track, l_i the thickness of the material i and ϵ_i the ionization energy lost per unit of thickness in the material i. The ionization energy loss is only corrected on average. The energy loss due to bremsstrahlung is mostly unseen by the helix fitter [37]. The bremsstrahlung has a significant impact

on the "first guess" when the energy lost is sufficient to force the identification of two separate tracks.

The helix fitter results are stored in the MOFIA output file for all the tracks. In particular the momentum and angle of the track at the DC closest to the target are saved.

3.3   Extraction of the decay parameters

MOFIA produces a `ROOT` [38] output file for each run analyzed. The event information stored is used to select events and to produce the momentum-angle spectrum of the decay positron.

Up to this point data and MC are analyzed independently. Now the two spectra are fit to each other first of all to perform a momentum calibration and secondly for the measurement of the decay parameters.

3.3.1   Spectrum reconstruction

The `ROOT` data structure (TTree) contains all the events of its corresponding run because MOFIA do not apply any cut or selection. Each entry in the data structure corresponds to one event. It contains the event type, the list of windows and the list of reconstructed tracks. For each window and each track a set of variables needed for the analysis are also stored. A `C++/ROOT` program called Clark analyses all the MOFIA output files and selects the valid decay positron tracks according to a set of cuts and selections detailed in Chapter 4. Finally the selected tracks are entered in a two dimensional histogram corresponding to the momentum-angle spectrum used for the muon decay parameters extraction and for the momentum calibration.

3.3.2   Muon decay parameter fit

The decay parameter fit extracts the difference between the data and the MC spectra in terms of muon decay parameters. The fitting procedure exploits the linearity in the decay parameters η, ρ and the products $P_\mu\xi$ and $P_\mu\xi\delta$. The difference between the data spectrum (S_D) and the MC spectrum (S_{MC}) can be expressed in terms of

derivative spectra as:

$$S_D = S_{MC} + \frac{\partial S}{\partial \eta} \Delta \eta + \frac{\partial S}{\partial \rho} \Delta \rho + \frac{\partial S}{\partial P_\mu \xi} \Delta(P_\mu \xi) + \frac{\partial S}{\partial P_\mu \xi \delta} \Delta(P_\mu \xi \delta). \qquad (3.3)$$

The derivative spectra are generated according to their analytical forms:

$$\left. \frac{\partial S}{\partial \eta} \right|_{\rho, P_\mu \xi, P_\mu \xi \delta} = \frac{m_\mu}{4\pi^3} W_{e\mu}^4 G_F^2 \sqrt{x^2 - x_0^2} \cdot \frac{2}{9}(4x^2 - 3x - x_0^2), \qquad (3.4)$$

$$\left. \frac{\partial S}{\partial \rho} \right|_{\eta, P_\mu \xi, P_\mu \xi \delta} = \frac{m_\mu}{4\pi^3} W_{e\mu}^4 G_F^2 \sqrt{x^2 - x_0^2} \cdot x_0(1 - x), \qquad (3.5)$$

$$\left. \frac{\partial S}{\partial P_\mu \xi} \right|_{\eta, \rho, P_\mu \xi \delta} = \frac{m_\mu}{4\pi^3} W_{e\mu}^4 G_F^2 (x^2 - x_0^2) \cdot \frac{1}{3} \cos \theta (1 - x), \qquad (3.6)$$

$$\left. \frac{\partial S}{\partial P_\mu \xi \delta} \right|_{\eta, \rho, P_\mu \xi} = \frac{m_\mu}{4\pi^3} W_{e\mu}^4 G_F^2 (x^2 - x_0^2) \cdot \frac{2}{9} \cos \theta (4x - 4 + \sqrt{1 - x_0}). \qquad (3.7)$$

Events are also generated for the negative regions of the derivative spectra (Fig. 3.9). A special variable containing the sign of the event is passed from spectrum generation to the spectrum reconstruction software.

Only the bins contained in fiducial regions for which the track reconstruction efficiency is maximal, are converted (Fig 3.10). The fiducial regions are detailed in the Sec. 4.4. A histogram referred to as the base and containing the MC bins and the weighted bins of the derivatives is created. The differences between the data bins and the corresponding base bins are used to define a χ^2 function which is minimized by the ROOT implementation of the standard MINUIT algorithm [39] with the derivatives weight as fit parameters. The fitting algorithm underwent various consistency tests [32].

3.3.3   Momentum calibration

Although the MC simulation was carefully designed to reproduce the experimental setup, some components are not reproduced accurately enough to provide the precision necessary to achieve the TWIST experiment goals. The decay positron reconstructed momentum is different from its momentum at the time of the decay. In fact the decay positron loses energy as it travels through the target module between the decay vertex and the first DC where the reconstruction starts. A mismatch of this energy loss between data and MC leads to a different detector response which
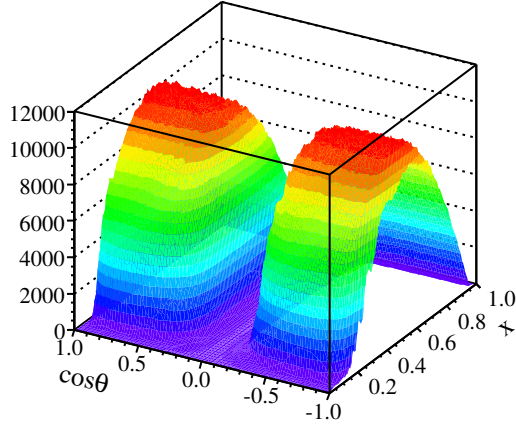
(a) Derivative $\dfrac{\partial S}{\partial \eta}$.
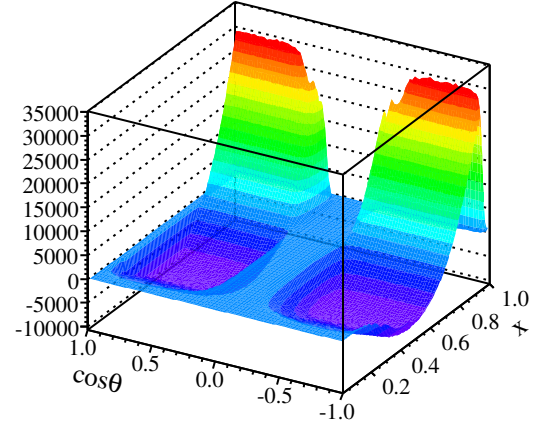
(b) Derivative $\dfrac{\partial S}{\partial \rho}$.
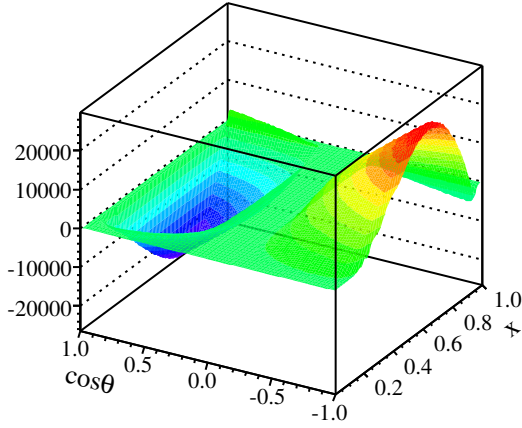
(c) Derivative $\dfrac{\partial S}{\partial P_\mu \xi}$.
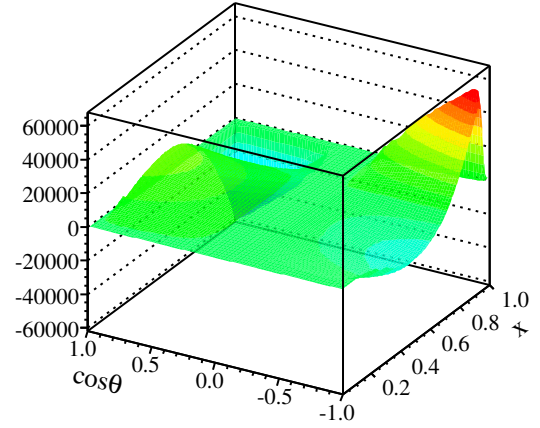
(d) Derivative $\dfrac{\partial S}{\partial P_\mu \xi \delta}$.

Figure 3.9: The derivative spectra describe the contribution of the decay parameters to the shape of the momentum-angle spectrum. The reduced positron energy $x = E_e/W_{e\mu}$ is used here instead of the momentum. These spectra include the detector response.
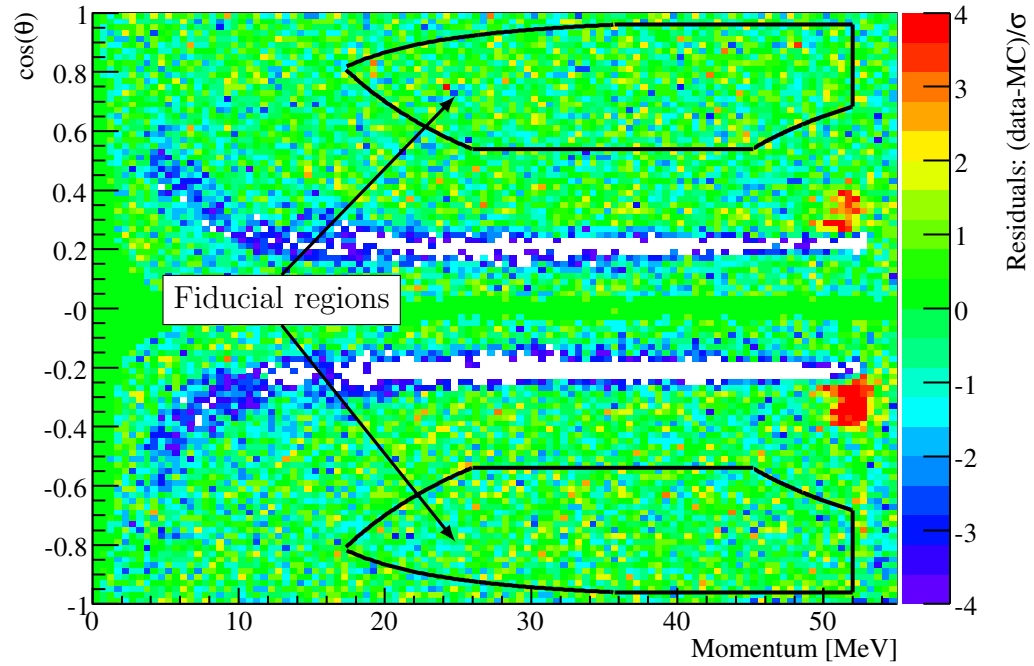
(a) Residuals from the spectra fit.
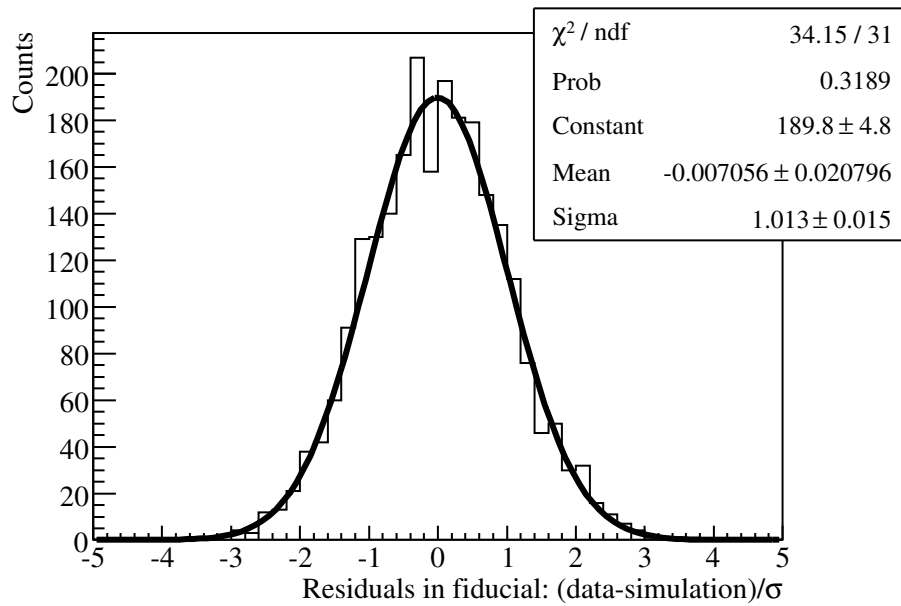
(b) Gaussian fit of the residuals in the fiducial regions.

Figure 3.10: The relative fit of the two spectra is performed only in the fiducial regions. The residuals are consistent with zero in these regions.

in return biases the decay parameters measurement. Such mismatch can originate from a mismatch in target thickness or in muon stopping distribution. Similarly the momentum is affected by a mismatch in the magnetic field strength since it changes the radius of the helix. A momentum calibration briefly described in this section is performed prior to the final decay parameter fit to correct for these biases. Further details can be found in [29].

The momentum calibration exploits the kinematic end-point of the decay positron as a point of reference to measure the bias in momentum and angle between data and MC. The maximum momentum p_{edge} of the decay positron is given by:

$$p_{edge} = \frac{m_\mu^2 + m_e^2}{2m_\mu} \simeq 52.83 \text{ MeV/c}$$

The algorithm determines the momentum shift required in the data spectrum to match the kinematic edges (Fig. 3.11(a)). The kinematic end-point shape is affected by the muon decay parameters. The data and MC spectra have very different parameters because of the hidden parameters in MC. This difference is typically few parts in 10^{-3} and it eventually biases the edge fit of the two spectra. For this reason a preliminary decay parameter fit is performed. The momentum calibration uses the sum of the MC spectrum and the weighted derivatives using these preliminary decay parameters. Only one iteration of the momentum calibration is needed for the decay parameters to converge.

Due to the planar geometry of the TWIST detector, potential momentum biases such as the energy loss have a $1/\cos\theta$ dependence. For this reason the momentum calibration is performed on kinematic edges at different values of $1/\cos\theta$. The momentum-angle spectrum is divided in constant bins of $1/\cos\theta$ in the range $0.5 < |\cos\theta| < 0.9$ ($1.11 < |1/\cos\theta| < 2.00$). For each $1/\cos\theta$ bin, the MC edge spectrum is shifted with respect to the data edge spectrum from 52.3 to 53.4 MeV/c by steps of one bin of 10 keV/c at a time. At each step a χ^2 is calculated such that:

$$\chi^2 = \sum_i \frac{(B_{data}(i) - B_{MC}(i))^2}{\sigma_{data}^2(i) + \sigma_{MC}^2(i)} \tag{3.8}$$

where $B_{data}(i)$ and $B_{MC}(i)$ are the number of counts in the bin i and $\sigma_{data}(i)$ and $\sigma_{MC}(i)$ are the statistical uncertainties for bin i. The resulting χ^2 distribution is fit with a second order polynomial to determine the momentum shift required to

minimize the χ^2.

Finally the momentum mismatch between data and MC versus $1/\cos\theta$ is fit independently upstream and downstream with straight lines (Fig. 3.11(b)). The calibration is given by the intercepts at $1/\cos\theta = 0$ referred to as the offsets (b_{up} and b_{down}), and two slopes or angle dependences (a_{up} and a_{down}).

The measured momentum mismatch at the kinematic edge is applied in a second reconstruction of the data spectrum (Fig 3.1). The model used for the propagation of the momentum mismatch to the entire spectrum depends on the source of the mismatch which could not be isolated. For this reason the muon decay measurement is the average of the analyses using a constant shift and a constant scale in momentum. A systematic uncertainty is assigned to this model dependence of the momentum calibration (Sec. 7.1.3).
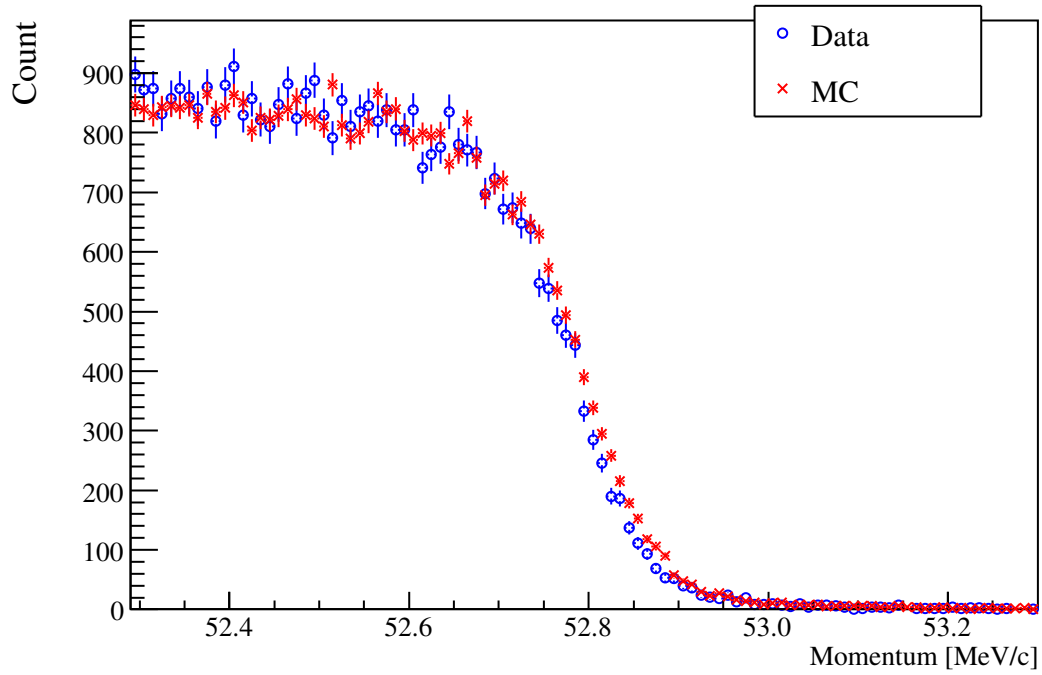
(a) Fit of the MC edge versus the data edge.
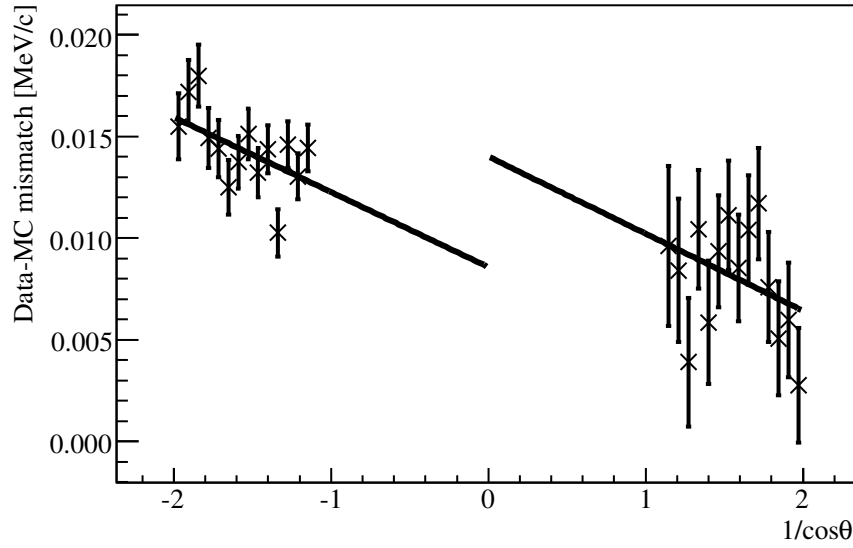
(b) Fit of the mismatch between data and MC versus $1/\cos\theta$.

Figure 3.11: The kinematic edges of the data and MC spectra are fit for certain $1/\cos\theta$ bins independently. The momentum calibration is defined by independent straight lines for upstream and downstream decays.

Chapter 4

Event selection

Most of the event selection is done during the spectrum reconstruction (Fig. 3.1). This chapter will describe the cuts in the spectrum reconstruction and the fiducial region of the momentum-angle spectrum selected in the spectrum fit. Fig 4.1 shows the number of events selected by each cut. Most of the cuts are applied identically on data and MC. For this reason, as long as they are applied in regions of minimal biases, these cuts are not a source of biases because their effects cancel out when the two spectra are fitted against each other. The pulse width cut is the only exception.

4.1 Beam and event type cuts

Time of flight cut

The high polarization of the muons is guaranteed by the selection of events triggered by surface muons. Only the events triggered by the highly polarized surface muons are used in the analysis. These events are selected using the time of flight structure of the M13 beamline.

The time of flight of a particle of mass m is given by the relativistic formula:

$$T = \frac{d}{v} = d\frac{E}{pc^2} = d\frac{\sqrt{(mc)^2 + p^2}}{pc} \tag{4.1}$$

where d is the distance between the production target and the muon counter (11.4 m), E is the total energy, p is the momentum and c is the speed of light. The corresponding time of flight for the pion and the muon is respectively 183 ns and 141 ns. This difference allows for a separation in time of muons and pions but not of

Figure 4.1: Number of events before each cut or selection is applied.
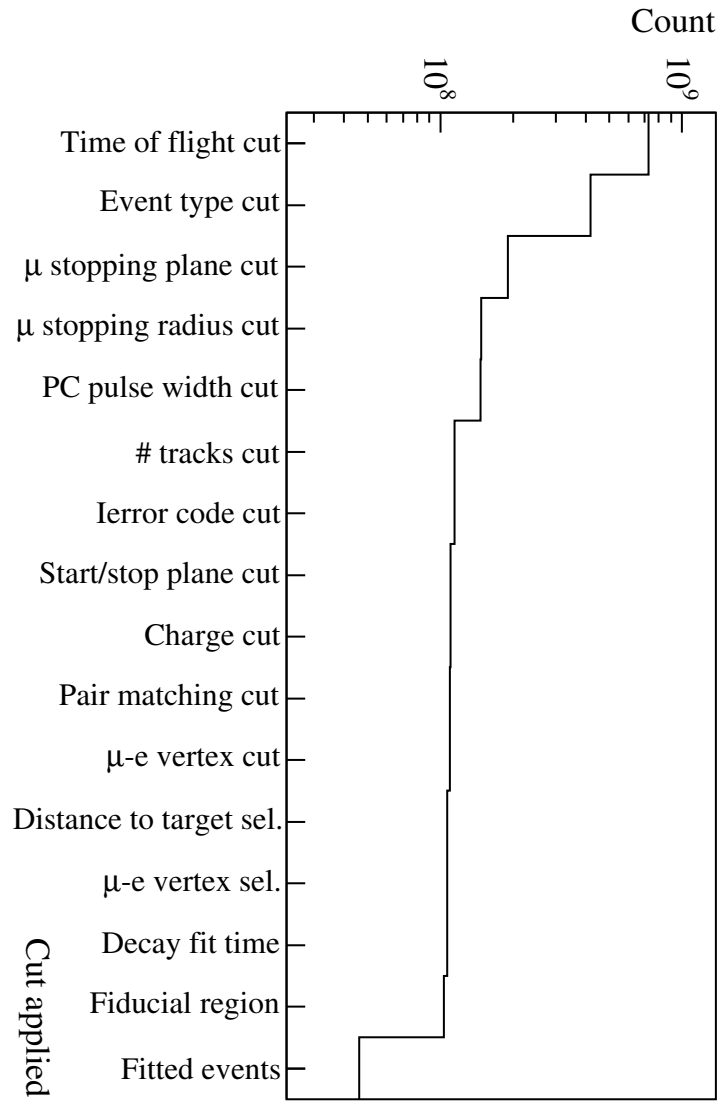
cloud muons and surface muons. Cloud muons are emitted from pions decaying in flight which leave the production target immediately after being produced. For this reason the cloud muons are emitted in coincidence with the production of the pions. On the other hand the surface muons are emitted according to the pion decay rate. This difference in emission time is used to select only the surface muons (Fig. 4.2).

The selected range of time of flight for the 2006 run period is (32,52)ns and for most of the 2007 run period the range is (32,55)ns (Fig. 4.3(a)). The selected range is (32,52)ns for the sets 91, 92 and 93 because the beam momentum selection is set at about 28.8 MeV/c instead of 29.6 MeV/c which changes slightly the time of flight distribution. The measured time of flight is actually the time between the particle's arrival at the muon counter and the *next* capacitive probe signal of the proton beamline (Sec. 2.1.1). This is why the distribution Fig. 4.3(a) appears to go backward in time compare to time of flight structure Fig. 4.2.
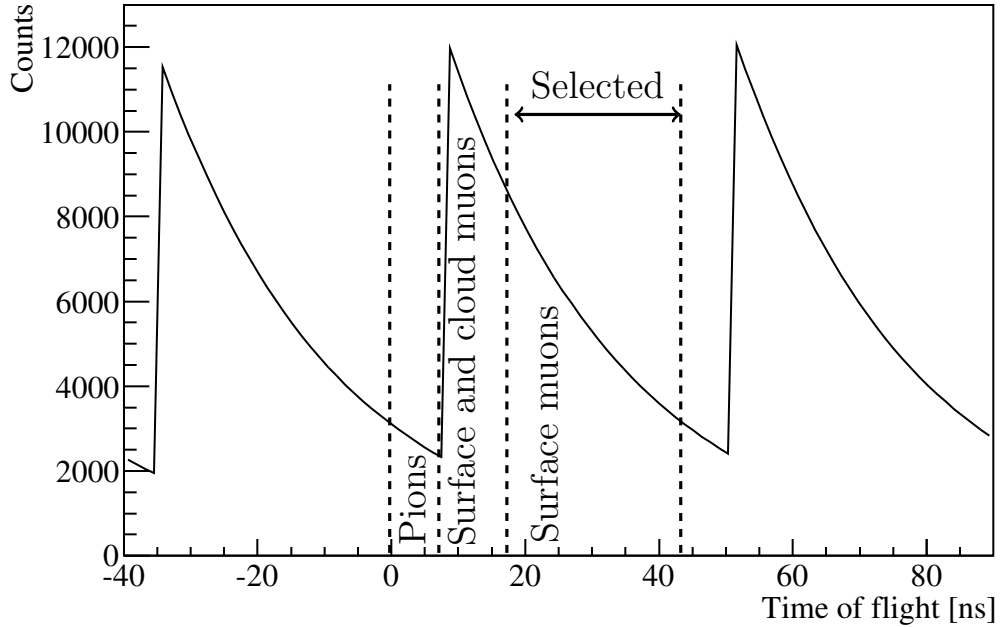
Figure 4.2: Time of flight structure of the beamline M13 at 29.6 MeV/c is periodic due to the cyclotron emitting protons every 43 ns. The main component is the surface muon distribution which is the exponential decay rate of the pion with a time constant of 26 ns. The pions and cloud muons on the other hand are prompt and therefore peaked around their respective time of flight.

Event type cut

Only the event types 1, 2, 6, 7, 10, 11, 21 and 22 are kept (Fig. 4.3(b)). The events types 1 and 2 are the most basic and clean events in which a muon and the decay positron as well as eventual beam positrons are well separated in time. Each time window contains only one particle.

The event types 6, 7 identify events in which the decay positron and a δ ray[1] overlap in time but not in the z direction. In fact the δ ray is emitted in the direction opposite to the decay positron. The event types 10 and 11 identify the decay positrons which scatter back into the spectrometer on material outside. This specific scatter is referred to as backscatter. These four event types are included because the emission of δ rays and the backscatter of decay positrons depend on the phase space and can be different in data and in MC. Some tracks of decay positrons backscattering are identified by the classification as being beam positron tracks. For this reason the event types 21 and 22 (decay and beam positrons overlap) are included in the analysis despite the fact that decay positrons and beam positrons are not correlated.

4.2   Muon selection

Muon stopping plane cut

The PCs surrounding the stopping target are used to determine where the muon stopped (Fig. 2.7). This cut removes events with hits in PC 7 or 8 making sure that the muon did not stop downstream of the target. A hit in PC 6 is required as well. Fig. 4.3(c) shows the wire chamber number of the last hit in the muon track. The wire chamber number refers to both PCs and DCs ordered by increasing z. Only muon tracks with a last hit in the wire chamber 28 (PC 6) are selected.

Muon stopping radius cut
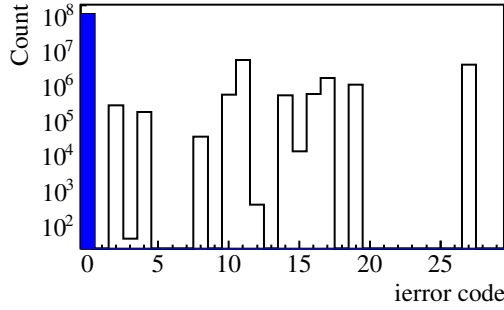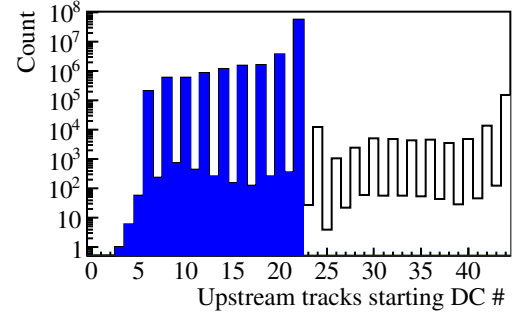
Muons stopping too far away from the detector axis are removed in order to exclude the possibility for the subsequent decay positrons to hit the glass structure of the outside of the DCs. The uv coordinates of the muon stopping position on the target are measured by PC 5 and 6. The muons with a radius such that $\sqrt{u^2 + v^2} > 2.5$ cm are excluded (Fig. 4.3(d)).

---

[1]A δ ray refers to an electron knocked out of its atomic orbital by another particle such as the decay positron.
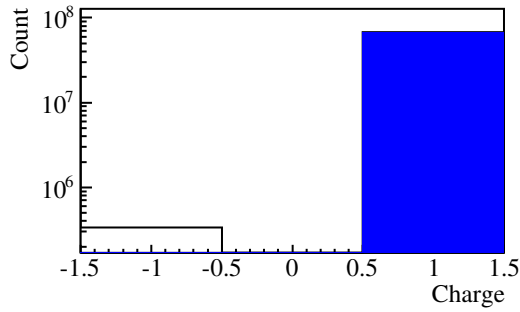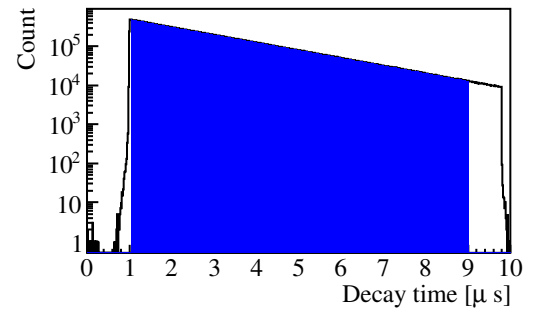
Figure 4.3: Typical histogram for each cut. The blue region represents the events selected by the cut.

PC 5 and 6 pulse width cut

This cut complements the muon stopping plane cut by identifying muons stopping upstream of the target. The muons stopping in the target and those stopping in PC 6 deposit different amounts of energy in PC 5 and 6. The pulse width of the hits in those wire chambers are therefore different and are used to discriminate between these two cases (Fig. 4.4).

The pulse width cut is defined by two straight lines in order to cut out the stops in the gas on one side and the stops in the wires on the other side (Fig. 4.5). The position of the cuts are tuned first on data. The cut on MC is defined such that the rate of muons passing the cut is the same in data and in MC. This guarantees that the muon stopping distribution along z matches in data and MC. A mismatch leads to a bias for the measurement of the decay parameters. For this reason a systematic uncertainty is assigned to this cut (see Sec. 7.1.5).

4.3   Track selection

The decay positron window in each event can contain more than one reconstructed track. The purpose of the following cuts is to identify which track corresponds to the decay positron.

Number of reconstructed tracks cut

This cut requires that the event has at least one reconstructed track.

Ierror code cut

All track candidates are recorded in the MOFIA output file even if they are not successfully reconstructed. An error code named "ierror" is set to zero if the reconstruction is successful and to an error code number specifying the error encountered by the reconstruction otherwise. The tracks with an "ierror" code different from zero are removed (Fig. 4.3(e)).

Start and stop plane cut

The window type of the decay window specifies if the decay positron travelled upstream or downstream of the target (Fig. 4.3(f)). This cut removes the tracks which
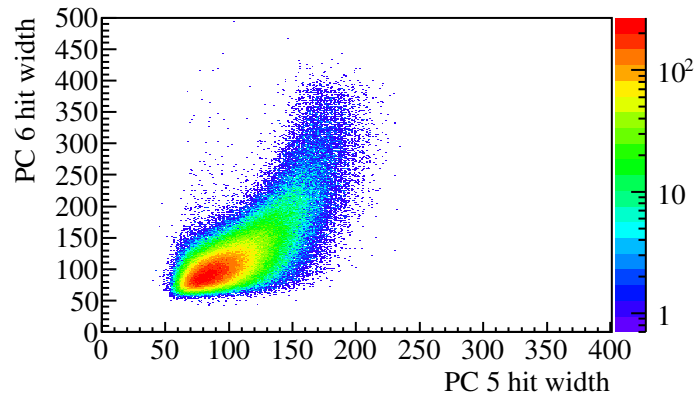
(a) Pulse width distribution for muons stopping in the target.
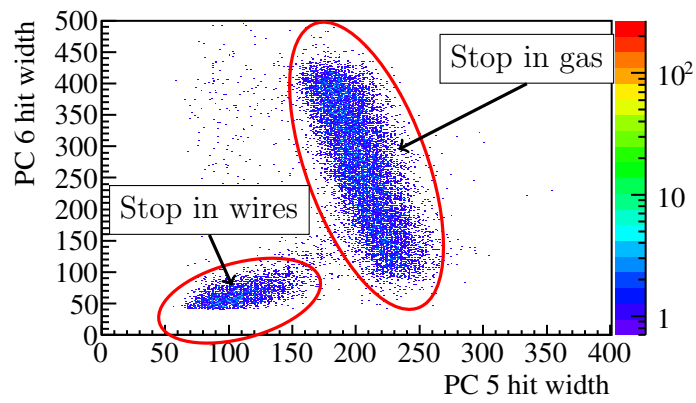
(b) Pulse width distribution for muons stopping in PC 6.
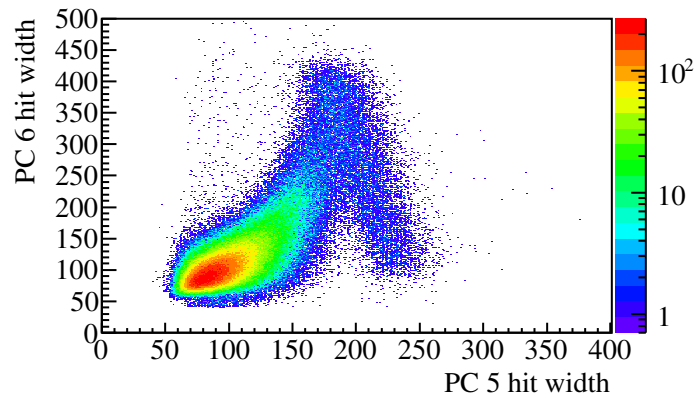
(c) Complete pulse width distribution.

Figure 4.4: The pulse width distribution in PC 6 versus PC 5 for muons stopping in the target and in PC 6 are separated in the MC to identify the different components of the complete distribution and to define the cut.
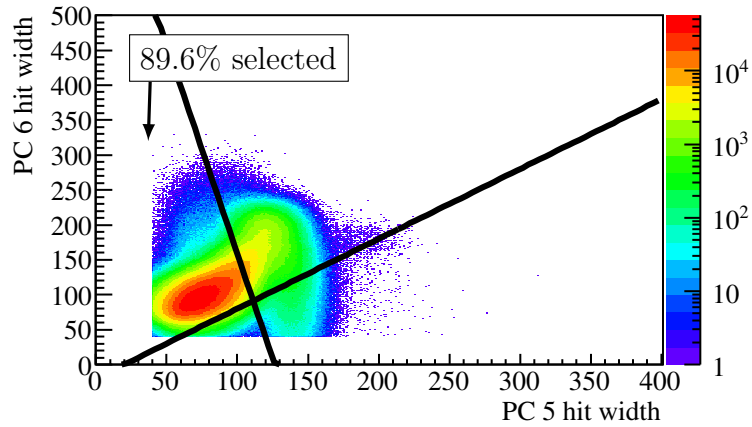
(a) Set 74 pulse width distribution.
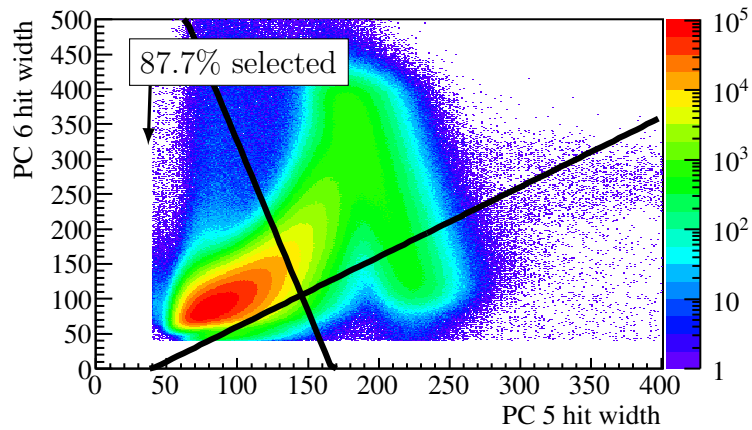
(b) MC matching set 74 pulse width distribution.

Figure 4.5: The cuts are tuned on data to reduce the stops in PC 6 and the subsequent fast depolarization. The MC cuts are tuned in order to have the same rate of selected event as in data. The chamber response in MC for PC 5 and PC 6 was not tuned accurately to data which explains the large differences in shape between Fig. (a) and (b).
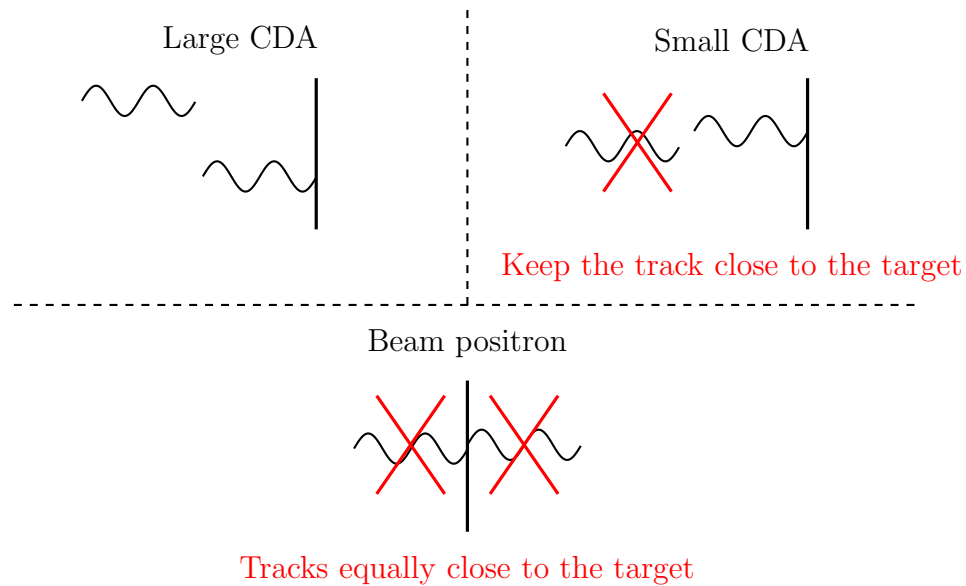
Figure 4.6: For two independent tracks the closest distance of approach (CDA) is large. For broken tracks, the CDA is small and the track further away from the target is removed. In the case of a beam positron or a backscattered decay positron, both halves are close to the target and are removed.

are on the wrong side of the target according to the window type.

Charge cut

The standard analysis is on positive muon decays therefore tracks of negatively charged particles are removed (Fig. 4.3(g)).

Pair matching cut

The purpose of this cut is to verify if two tracks in the decay window are actually from a unique particle to remove unnecessary tracks. Two parameters are used to find out if two tracks match. The track times of two matching tracks as determined by the helix fitter must agree within than 60 ns. Also the closest distance of approach (CDA) between the two tracks is calculated in three dimensions in MOFIA. A small distance of approach means that the tracks are from the same particle. Broken tracks and beam positron tracks are the two configurations targeted by the cut (Fig. 4.6).

The CDA distribution is different in the case of a beam positron or a broken track. In the case of the beam positron, the two tracks are reconstructed separately on each

side of the detector. The corresponding CDA is related to the multiple scattering in the target. In the case of a broken track the reconstruction identified two tracks instead of one because of a large scatter which could not be taken into account by the kinks in the reconstruction. This is why the CDA from broken tracks is on average larger than the CDA from beam positron tracks.
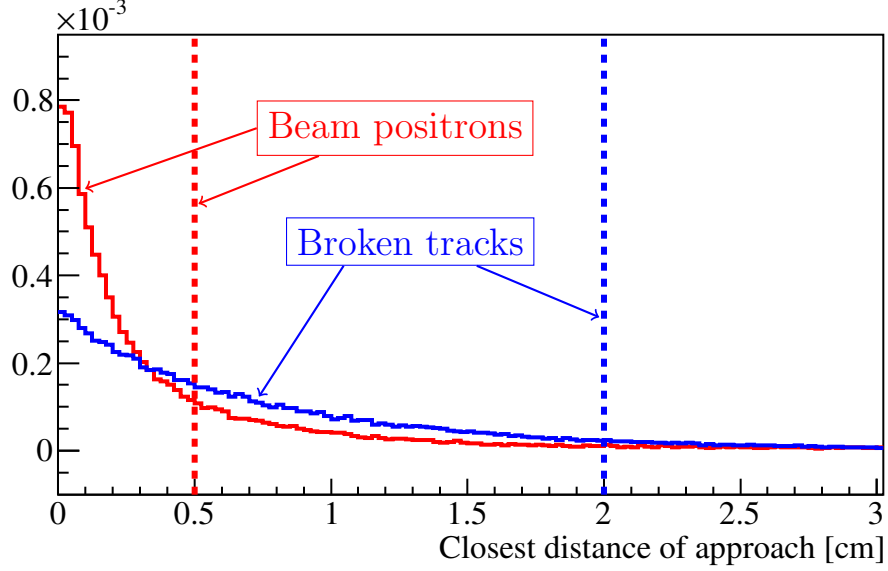
Figure 4.7: The CDA distribution for beam positrons shows that most CDA values are less than 0.5 cm. On the other hand the CDA for broken tracks is much more spread out and the cut is set at 2 cm.

The CDA cut is set at 0.5 cm for beam positrons and 2 cm for broken tracks. The z position of the CDA is used to determine which case the tracks correspond to. Tracks with a CDA located less than 6 cm away from the target are from beam positrons. Tracks with a CDA located more than 22 cm away from the target are from broken tracks. In the intermediate region between 6 and 22 cm the CDA generally comes from the match of two tracks distant in z. The conservative value of 0.5 cm is used in this region.

Muon-positron vertex cut

A way to certify if a track is the decay positron is to use the position of the track at the target with respect to the muon stop position. The muon position on the target is measured by PC 5 and 6. The reconstructed tracks (decay positron candidates) are extrapolated to the target in MOFIA and their position in u and v is stored in the

MOFIA output file. This extrapolation corrects the average energy loss between the target and the first tracking chamber. A track is not the decay positron if its distance to the muon at the target is too large. The distance travelled by the decay positron between the decay vertex and the first tracking chamber depends on $1/\cos\theta$. For this reason the vertex distance is also $1/\cos\theta$ dependent (Fig. 4.8). The cut takes this dependence into account and is set at the limit where the ratio signal over background is 50% for the selected tracks.
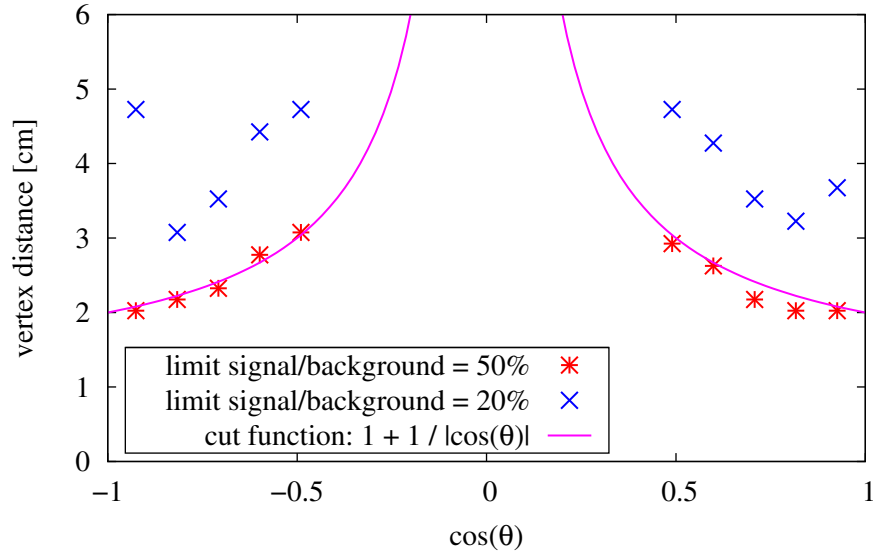
Figure 4.8: Limit of the ratio signal over background. For the selected tracks the ratio is larger than 50%. The decay positron track is identified in the MC study to define the signal and the background. Here background means any particle other than the decay positron. The vertex distance depends on $1/\cos\theta$ because of the planar geometry of the detector.

Distance to target selection

If more than one track passed the previous cuts, the analysis must decide which track is more likely to be the decay positron. The track closer to the target should be the decay positron. If both tracks are from the decay positron, the reconstruction of two tracks instead of one is indicative of a large scatter between the two. For these reasons the track farther away from the target is removed.

Muon-positron vertex selection

This final selection ensures that only one track is selected to go into the spectrum. It evaluates which track is closer to the muon at the target using the same information used for the muon-positron vertex cut.

Decay fit time

Positrons from early or late decays in the event are removed using the decay time calculated by the helix fitter (Fig. 4.3(h)). The positron hits from early decays could overlap the muon hits in the upstream half of the detector leading to a different reconstruction efficiency upstream and downstream. Some of the positron hits from muon decaying close to the end of the event window are eventually not recorded and the track reconstruction is missing hits. The decay fit time cut removes such tracks.

4.4 Fiducial region selection

Unlike the other cuts presented in this chapter, the fiducial cuts defining the fiducial region in the $(p, \cos\theta)$ spectrum are applied in the decay parameter fit procedure (Fig. 4.9). The reason for this difference is that the fiducial cuts do not select individual events. Instead the cuts are applied on the energy-angle spectrum and select histogram bins according to their central position in the spectrum. This guarantees that all the bins used in the decay parameter fits have an occupancy independent of the fiducial cuts. The fiducial cuts are applied identically to the data and the MC spectra and for this reason do not create any biases as long as the fiducial region is within the region of minimal biases.

The choice of the fiducial region is driven by two opposing constraints. On the one hand the fiducial region must be as wide as possible to increase the number of events used in the decay parameters fit. The sensitivity to changes in the muon decay parameters is also enhanced by the inclusion of a larger part of the spectra. On the other hand the fiducial cuts exclude regions which may have significant biases. These biases can be due to the track reconstruction, to reduced resolution or differences in the detector geometry between data and MC.

- $|\cos\theta| > 0.54$

  Each track is reconstructed from 22 planes only. In this geometry high angle tracks cannot be resolved due to the high winding numbers.

- $|\cos\theta| < 0.96$

  Small angle helices have also very small radii comparable to the DC wire spacing of 4 mm. For this reason the reconstruction of these tracks in not reliable.

- $p < 52.0$ MeV/c

  The tracks with a momentum above this cut are used in the energy calibration and therefore are excluded for the muon decay parameter fit.

- $p_l > 14.0$ MeV/c

  This cut on the longitudinal momentum removes the region with potential degeneracies (Fig. 2.6) in the track reconstruction. Although the detector geometry was modified, some degeneracies still exist. However they are now further away from the fiducial region.

- $p_t < 38.0$ MeV/c

  Large transverse momentum tracks eventually go outside of the tracking region. They can in particular hit the glass frame in the detector which is not in the MC leading to a difference between data and MC.

- $p_t > 10.0$ MeV/c

  This cut removes tracks with small transverse momentum and therefore with very small radii.
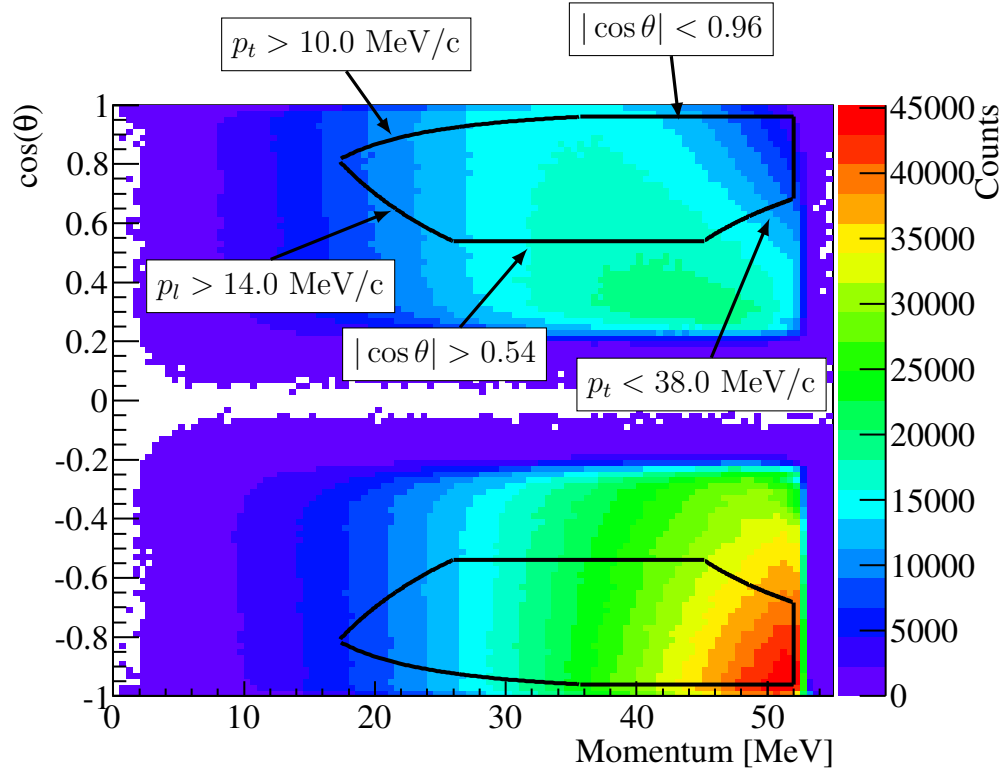
Figure 4.9: Experimental energy-angle spectrum with the fiducial cuts superposed. The bins with their center inside one of the two fiducial regions are used for the spectra fit.

Chapter 5

Monte Carlo simulation

The Monte Carlo simulation (MC) of the TWIST experiment uses the `GEANT3.21` package [40] to simulate the particle interactions, the detector geometry and its electronics. The simulated physics processes include the energy loss in matter, multiple scattering and hard scattering such as bremsstrahlung emission and δ ray production. None of these processes are modified from the `GEANT3.21` package. The positions of the spectrometer components are set to reproduce as accurately as possible the experimental detector.

For each data set, a matching MC set was generated with the corresponding experimental conditions. As a naming convention, the set numbers for the MC sets matching a data set with the silver stopping target are in the 400 range and in the 500 range for the aluminium target. For example the MC set 474 matches silver target data set 74, and the MC set 584 matches the aluminium target data set 84. In total over all the sets, the number of events generated represents 2.7 times the number of events from the data sets.

This chapter describes the component of the MC specific to the TWIST experiment. An overview of the validation of the physics processes and the detector geometry is also presented.

5.1 Beam rate and profile

The M13 beamline is not included in the MC. Only surface muons and beam positrons from M13 are simulated because pions and cloud muons are removed in data by the time of flight cut (see chapter 4). The muon rate is extracted from the muon trigger

rate. The beam positron rate is extracted from the average number of beam positron per event in data.

The muon beam profile is measured by the TEC. For this reason the muon beam starts in the MC in the center of the TEC at approximatively -191 cm. The low hit efficiency for positrons prevents the TEC from reconstructing their tracks. Instead the beam positron profile is measured by the spectrometer with zero magnetic field. In this configuration, the beam positron straight tracks are reconstructed in the spectrometer and extrapolated back at -295 cm upstream of the target, at the beginning of the magnetic field map. This beam profile is used to generate the beam positrons starting at -295 cm.

5.2 Detector geometry

The simulation includes the elements necessary to reproduce accurately the muon and positron tracks and their interactions. The magnetic field is the same `OPERA` field map used for the analysis; it covers the whole spectrometer and extends 3 m upstream of the target to cover the fringe field region outside of the steel yoke. The particles are transported in the magnetic field using a classical fourth order Runge-Kutta numerical method. The muon spin is also transported in the magnetic field using the BMT equation [41].

The wire chambers with their cathode planes and wires are included. The type and properties of the gas inside the chambers and the cradle are also simulated. The composition of the gas in the gas degrader is set precisely to match the composition of the corresponding data set. This is required to reproduce the muon stopping distribution in the target.

5.2.1 Outside material

Decay positrons sometimes backscatter on material outside of the wire chamber tracking region. The hits from backscattered positron tracks are a source of confusion for the reconstruction algorithm, which reduces the reconstruction efficiency. Furthermore the probability for the decay positron to backscatter depends on its phase space therefore the effect on the reconstruction efficiency is eventually momentum and angle dependent.

The time of flight distribution measured by the upstream and downstream PCs

is used to compare the amount of backscattered positrons in data and MC (Fig. 5.1). For most data sets the upstream backscatter is much larger than the downstream backscatter due to the upstream beam package (Sec. 2.1.4). The downstream backscatter in the regular MC does not match the data because of interactions in the yoke which is not simulated. The downstream beam package installed for the set 83 (Sec. 2.2) is simulated in the MC set 583. The comparison of the upstream and downstream backscatter validates the symmetry of the detector in data and MC for this special set.

5.3 Decay positron spectrum

The event server producing pairs of $(|\vec{p}|, \cos\theta)$ for the MC simulation uses the theoretical muon decay spectrum with hidden decay parameters in a Monte Carlo acceptance-rejection method. This theoretical spectrum includes full $\mathcal{O}(\alpha)$ radiative corrections with exact electron mass dependence [42], the leading logarithmic terms of $\mathcal{O}(\alpha^2)$ [43], the next-to-leading logarithmic terms of $\mathcal{O}(\alpha^2)$ [44, 45], leading logarithmic terms of $\mathcal{O}(\alpha^3)$ [45], correction for soft pairs and virtual pairs [46], and an ad-hoc exponentiation. Each sample is used only once so all the events simulated are statistically independent.

During the generation of the simulation runs, the MC program connects to the event server and receives a set of samples. Other than the initial momentum and angle of the decay positrons, all the physics processes are generated from the MC random seed. The seed is defined by the run number of the simulated file. Each run number is used only once to keep all the MC runs statistically independent.

5.4 Chamber response

The MC reproduces the discontinuous behavior of the ionization of the wire chamber gas. Ionization clusters are randomly generated along the path of charged particles. The drift time of each cluster is calculated from STRs that were created by a `Garfield` simulation [47]. The analysis STRs measured from decay positron tracks and used for the track reconstruction (see Sec. 6.3) include features from the helix fitter on top of the chamber response. For this reason they cannot be used to simulate the drift times in the MC. The different ionization clusters from a drift cell are summed up and the closest cluster to the wire defines the hit time to reproduce the behavior
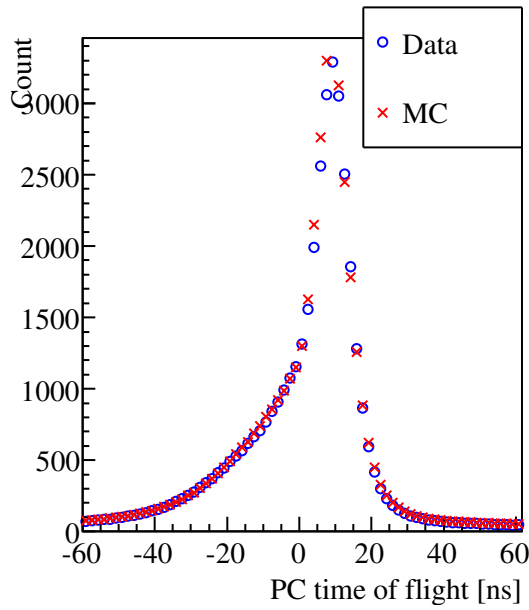
(a) Upstream backscatter signal in set 84 and MC set 584.
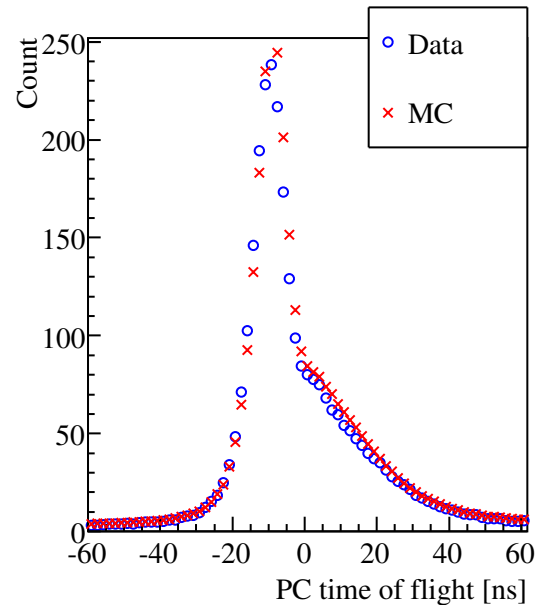
(b) Downstream backscatter signal in set 83 and MC set 583. Both data and MC contain a downstream beam package.
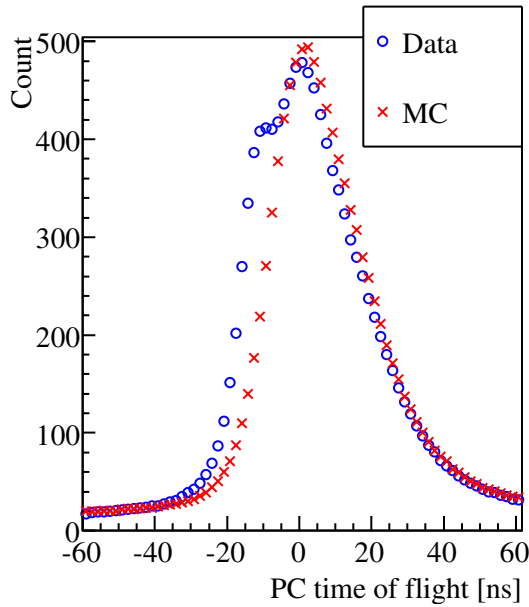
(c) The downstream backscatter signal in the data set 84 (at -18 ns) is not in the MC set 584 because the yoke is not simulated.
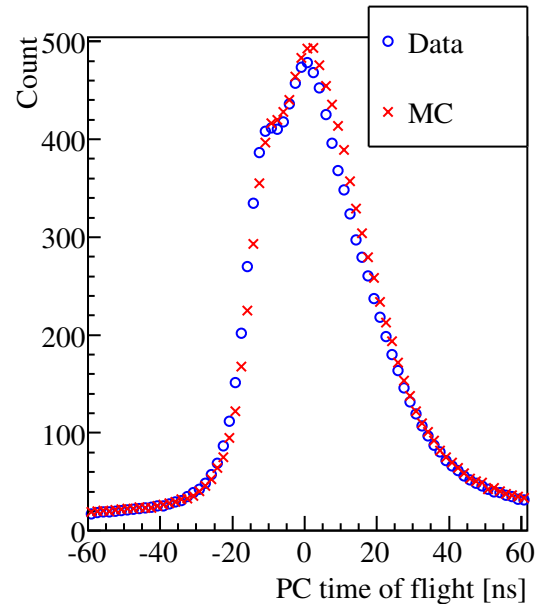
(d) The downstream backscatter signal (at -18 ns) is well reproduced in a special MC simulating the yoke.

Figure 5.1: The time of flight is measured by the difference between the downstream PC and the upstream PC hit times. The backscattered positrons and beam positrons cannot be separated reliably. For this reason these distributions contain the time of flight distributions from both sources.

of the real chambers. The chamber response is matched to the data by adjusting the statistical threshold and the ion cluster separation in the MC configuration. The statistical threshold, set at 1.6 clusters, defines the number of clusters in a cell needed to create a hit. The ion cluster separation, set at 0.3 mm, defines the average distance between two ion clusters. These two parameters were tuned for this measurement to improve the MC chamber response (Fig. 5.2).
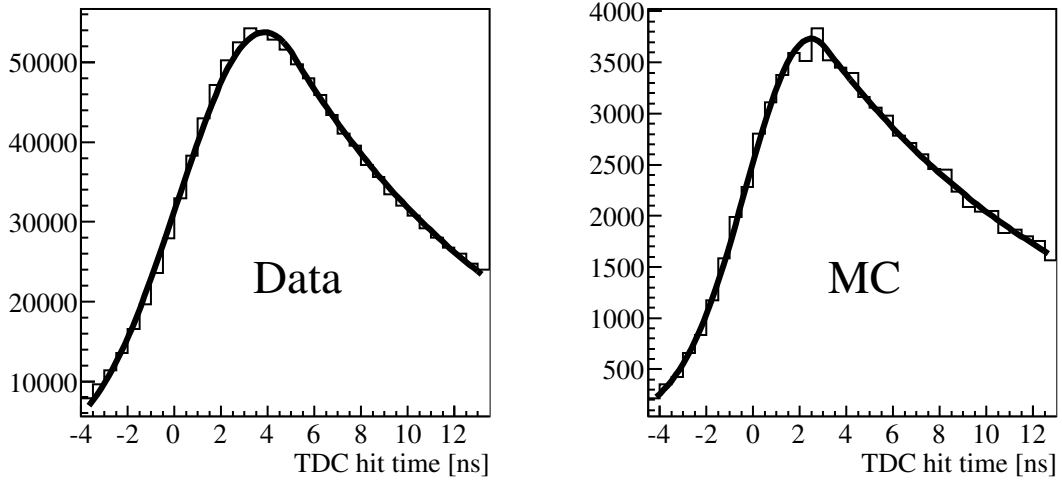
Figure 5.2: The TDC hit time distributions are used to tune the chamber response. The two tuning parameters are adjusted until the widths of the data and MC distributions match.

5.5   Validation

5.5.1   Target stops

The simulation and the experimental data are compared at different stages of the analysis in order to evaluate how well the MC reproduces the experimental setup. These comparisons are used in particular to validate the incoming beam (muons and beam positrons) in the simulation.

The stopping distribution of the muons in the z direction shows the match in the amount of material traversed by the muon and in the initial muon momentum (Fig. 5.3). The remaining difference mostly comes from the identification of the muons using the PCs which do not have exactly the same response in data and in MC.

Similarly the event type distributions show a good agreement between data and
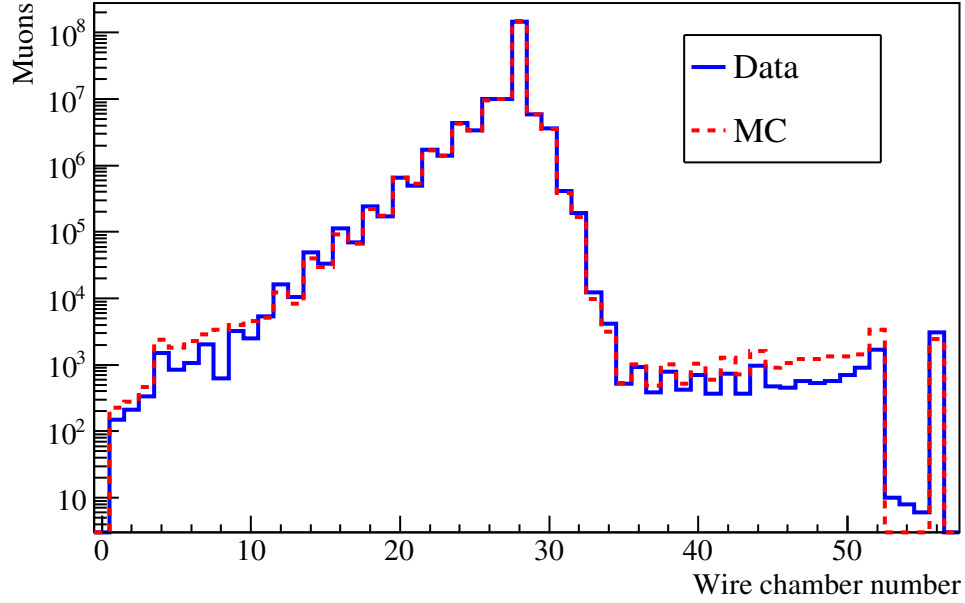
Figure 5.3: The muon stopping distribution is well matched by the simulation.

MC (Fig. 5.4). Only the event types used in the reconstructed spectrum are relevant in this comparison. The other event types are affected by the fact that the beam in data contains background particles such as pions and radioactive gas but the input beam in MC contains only muons and beam positrons. The mismatch in the event types 10, 11, 21 and 22 is due to the beam positron rate being too high in the MC.

5.5.2 Far upstream stops

A special set of data is taken with the muons stopping in the upstream PCs (PC 1 to 4) and the muon counter. A downstream decay positron then travels through the entire detector. Furthermore they cover the phase space according to the $\cos\theta > 0$ half of the energy-angle spectrum. This provides a set of tracks that are reconstructed in both halves of the detector simultaneously. The details of the analysis of the far upstream stops data can be found in [29].

Positron interactions

Using the upstream stops data, the angle and momentum at the extremity of the two reconstructed tracks near the target are compared in order to validate the MC of the decay positron interactions in the target.
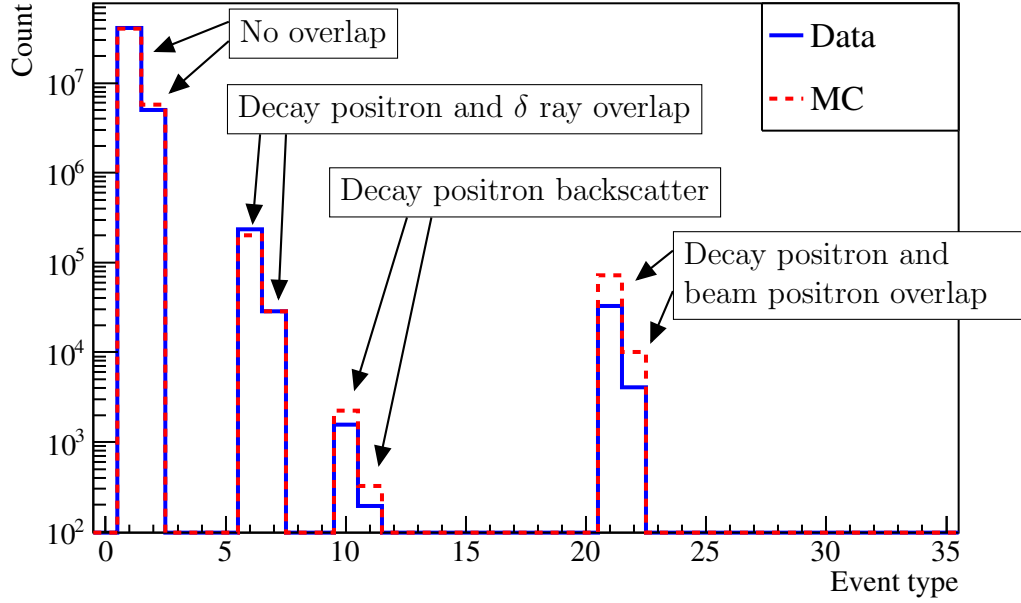
Figure 5.4: Event type distributions used for the muon decay parameters measurement. The differences are mostly due to a mismatch in the beam positron rate.

The change in angle, $\Delta\theta$, provides a measurement of the multiple scattering through the target module which includes the target foil and the target PCs (Fig. 5.5 and 5.6). The mismatch between data and MC for the silver target multiple scattering is in part due to a mismatch in the target thickness. The thickness of both targets was reevaluated after the MC sets were generated and the silver target thickness was found to be $(30.9 \pm 0.6)\mu m$ instead of the 29.5 μm measured previously and used in the MC geometry. The aluminium target thickness is consistent in MC and data at $71\mu m$ and $(71.6 \pm 0.5)\mu m$ respectively.

The change in momentum, Δp, is a measure of the energy loss through the target module. The quantity $\Delta p|\cos\theta|$ is shown in Figs. 5.7 and 5.8 instead of Δp in order to remove the $1/\cos\theta$ dependence of the momentum originating from the planar geometry of the detector. The match between MC and data for the aluminium target is again better because of the mismatch in the thickness of the silver target. The difference between the energy loss distributions in data and MC is less than 10% from 100 keV/c up to 10 MeV/c. The mismatch in energy loss between data and MC is corrected in the analysis of the nominal data by the momentum calibration procedure. The tail of the distributions (> 1.0 MeV/c) shows the match of the hard scatter processes. The evaluation of the corresponding systematic uncertainties from

the δ ray and bremsstrahlung rates using target stops confirms a match of respectively 0.7% and 2.4% (see Sec. 7.1.1).

Track reconstruction efficiency

The upstream stops data are also used to measure the track reconstruction efficiency because the same decay positron is reconstructed independently by the two halves of the spectrometer. The upstream (downstream) reconstruction efficiency is defined by the presence of a track downstream (upstream) and a reconstructed track upstream (downstream). Hits in the upstream and downstream PCs are required to guarantee that the decay positron traversed the whole spectrometer.

The advantage of the upstream stops measurement is that the reconstruction efficiency is obtained with respect to the angle and the momentum of the reconstructed track (Fig. 5.9). The momentum region around 29.6 MeV/c is removed from the analysis because this is the momentum of the beam positrons. Since their rate and beam profile are not very well matched between data and MC, using them would bias the reconstruction efficiency measurement.
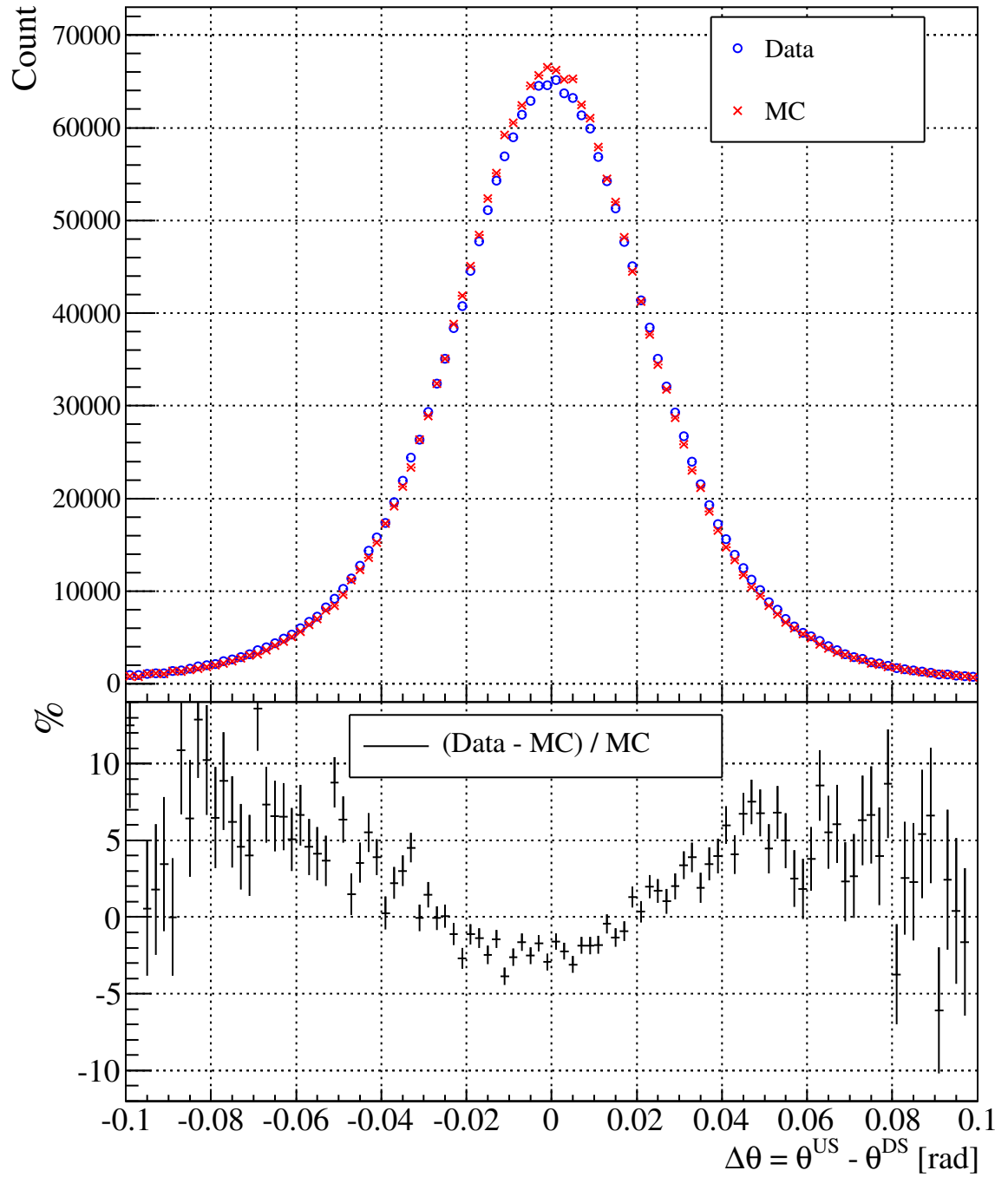
Figure 5.5: Angle difference between the upstream and downstream tracks for the silver target. The difference between data and MC is explained by the known difference in target thickness.
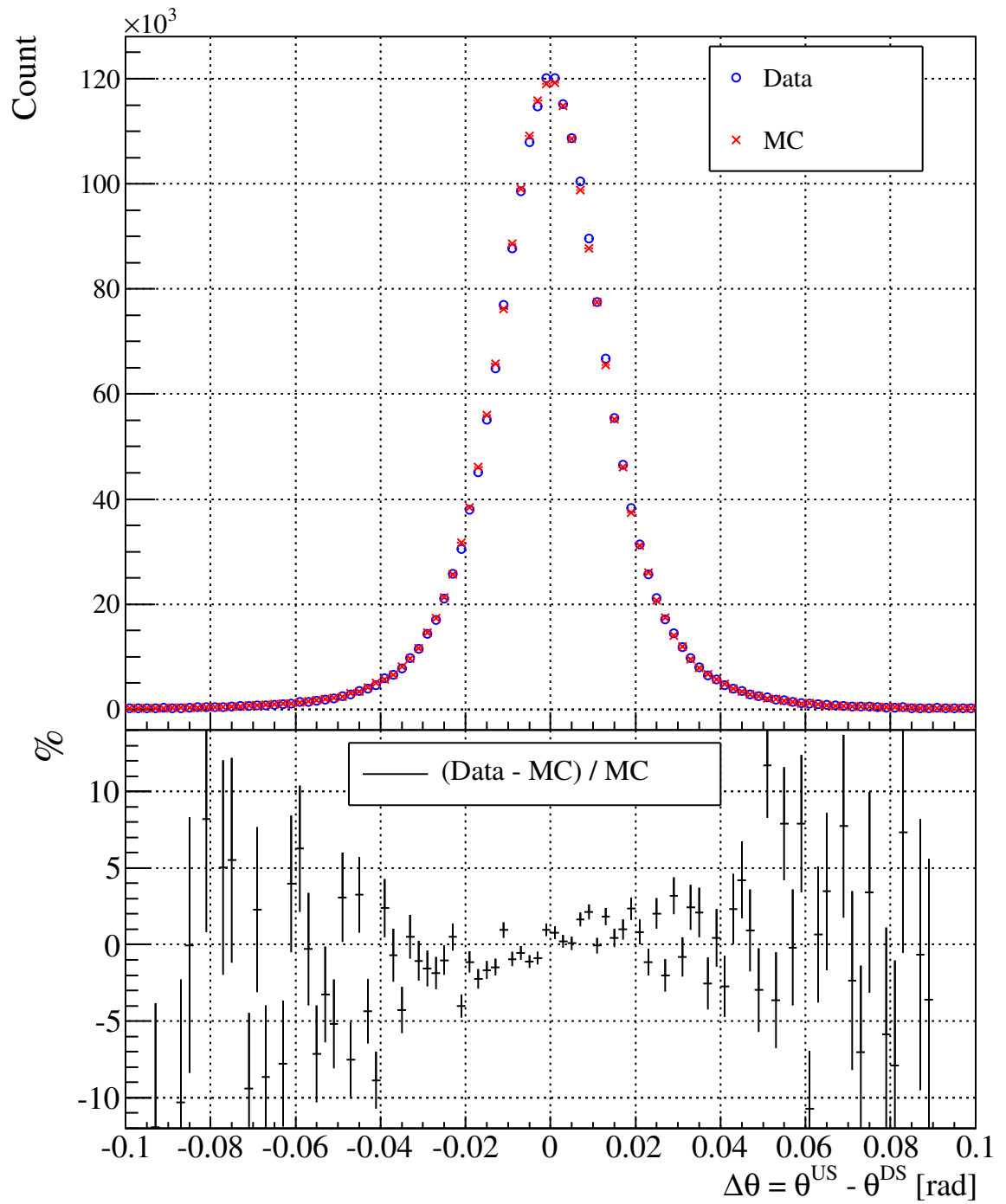
Figure 5.6: Angle difference between the upstream and downstream tracks for the aluminium target. The mismatch between data and MC is less than 5% which validates the physics processes and the geometry of the target module in the simulation.
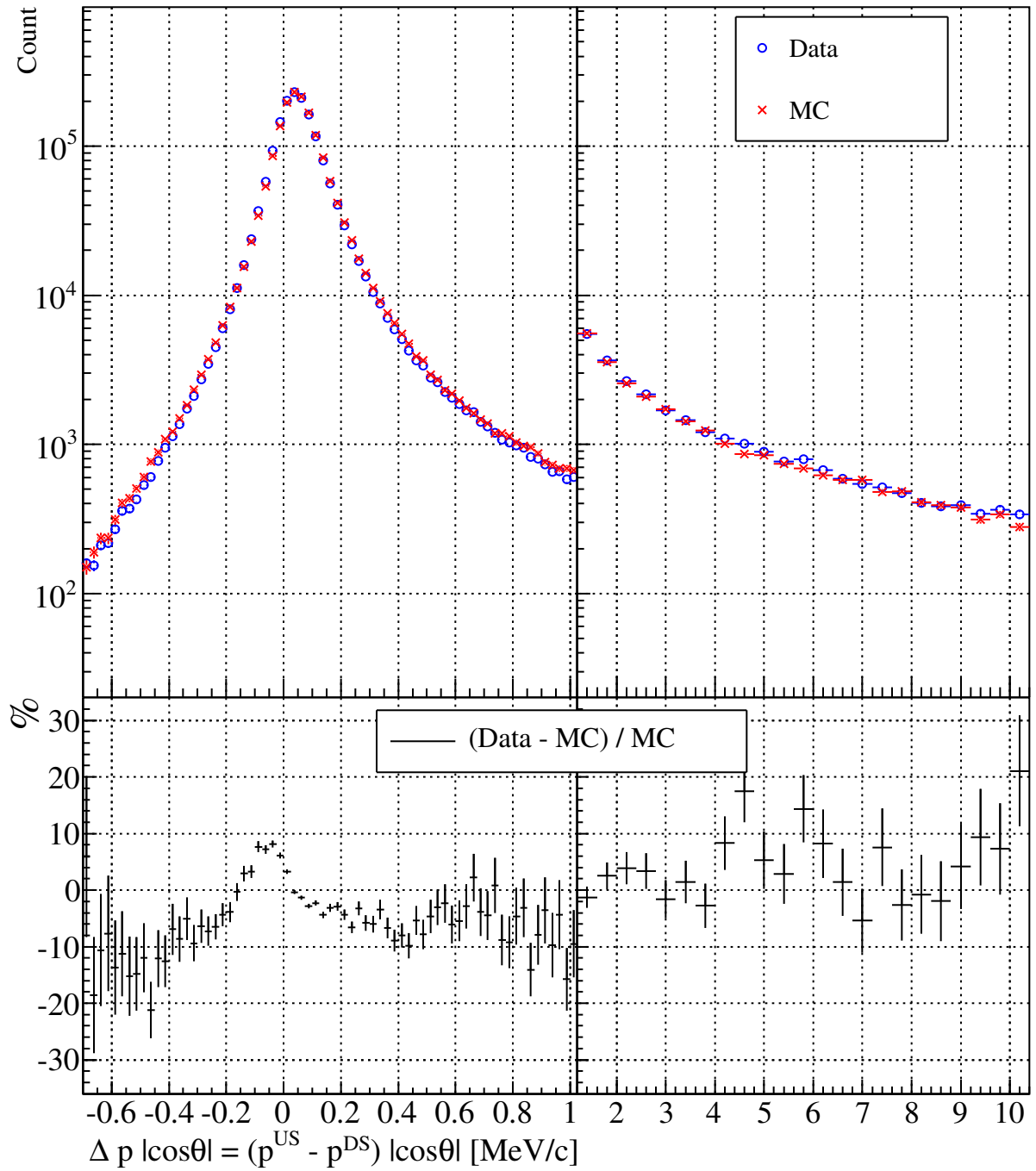
Figure 5.7: Energy loss through the silver target. A positive difference in momentum between the upstream and downstream tracks represents an energy loss for the decay positron. The bin size is different for the right and the left plots.
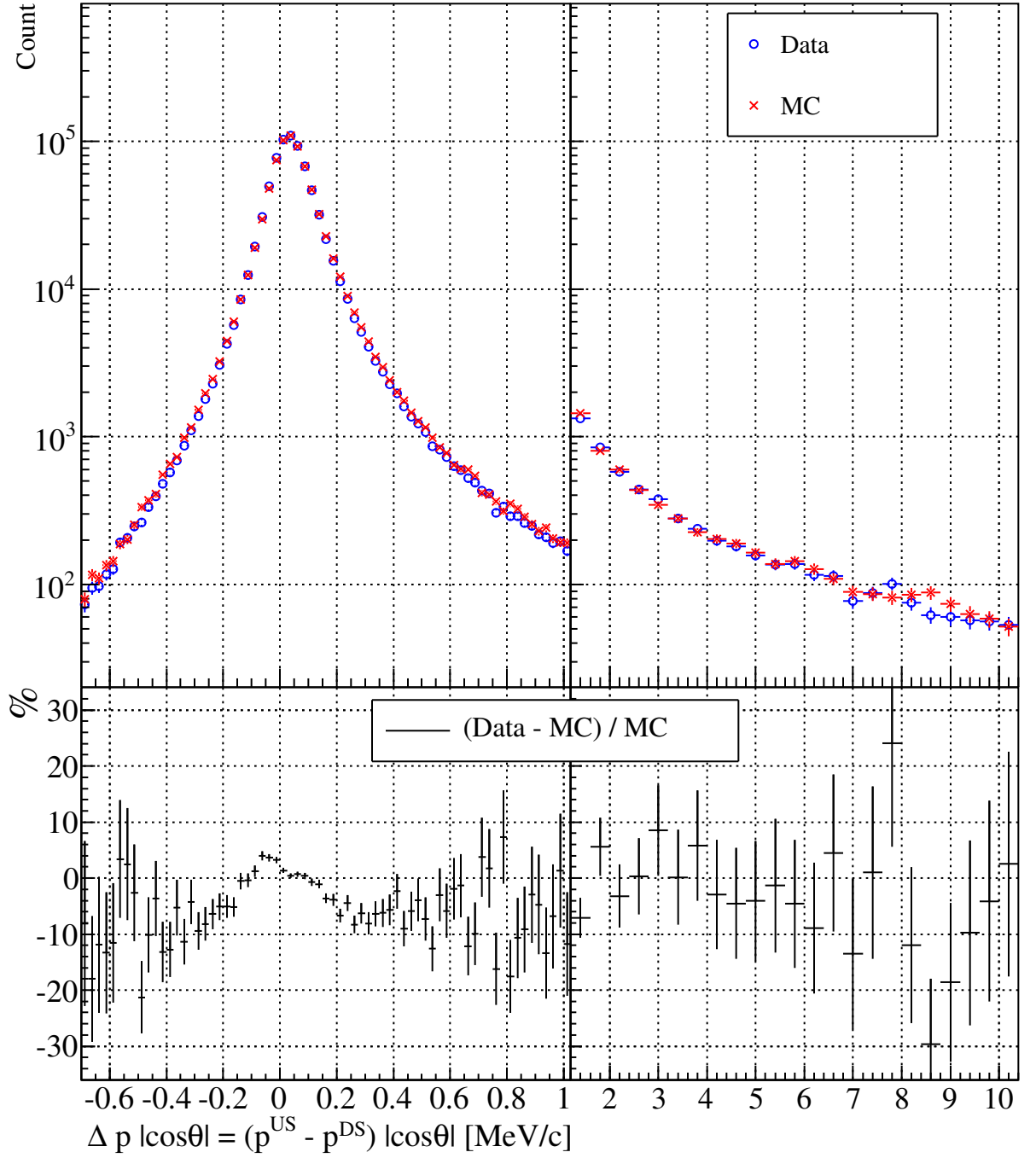
Figure 5.8: Energy loss through the aluminium target. A positive difference in momentum between the upstream and downstream tracks represent an energy loss for the decay positron. The bin size is different for the right and the left plots.
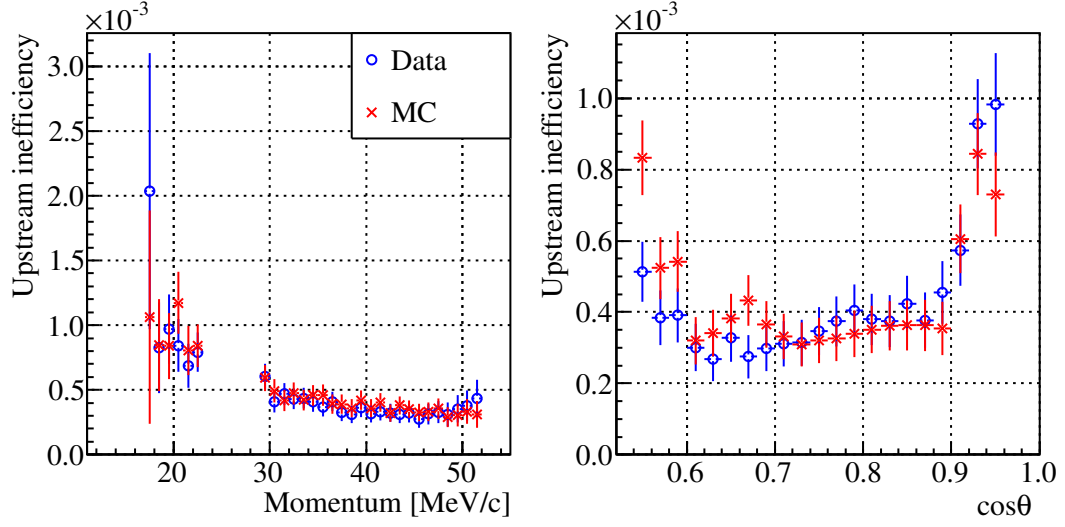
(a)
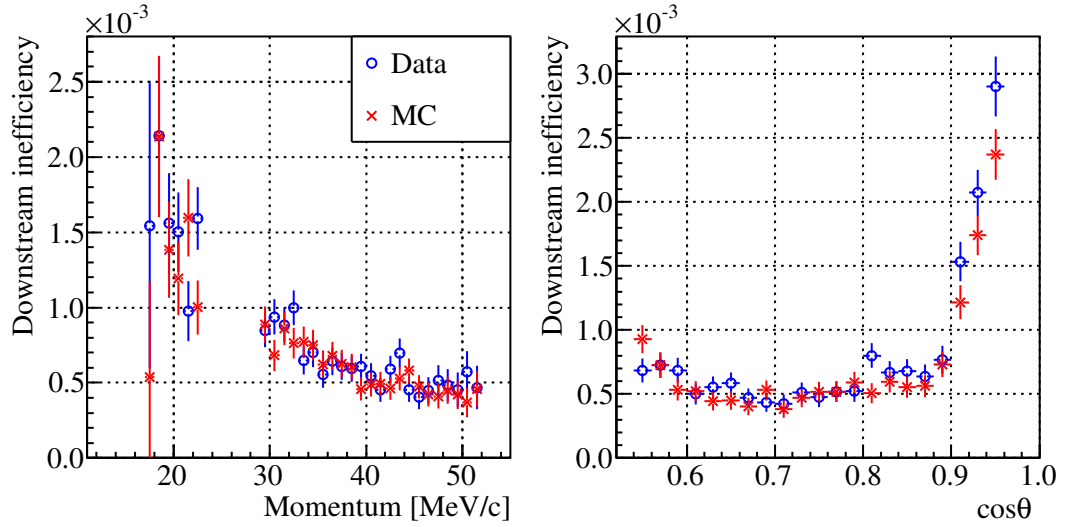
(b)

Figure 5.9: Reconstruction inefficiency (one minus the efficiency) extracted from upstream stops data taken with the aluminium target. This inefficiency measurement is consistent with the measurement using the silver target.

Chapter 6

Detector calibration

The calibration of the TEC and the relative alignments of the apparatus components did not lead to any significant systematic uncertainties for δ or η. For this reason the explanation of these calibration procedures can be found in appendix C for the TEC and appendix D for the alignments.

6.1 Cathode foil bulge

The cathode foil bulge must be minimal in the spectrometer in order to reduce the difference between data and MC since the latter contains perfectly flat cathode foils. The calibration procedure presented here determines the differential pressure between the wire chambers and the cradle required to minimize the bulge.

The foil bulge changes the distance between the anode wires and the cathode foil, which alters the strength of the electric field. This modifies the drift time across the DC. The foil bulge is measured by comparing the average drift times in a disk at the center of the DC and in a surrounding ring (Fig. 6.1). The average drift time is different in the two regions only if the foil is bulged.

The optimal differential pressure is extracted from a special set of data for which the differential pressure is varied (Fig. 6.2) and is consistent between the 2006 and 2007 data at 113 mTorr. An estimation of the relationship between bulge and differential pressure was evaluated at 12 μm/mTorr [26]. The differential pressures for the physics data during the 2006 and 2007 run periods are respectively 108 mTorr and 113 mTorr. For this reason there was a permanent bulge of $(-60\pm22)\mu$m (average) during the 2006 run period, and a bulge of $(8\pm22)\mu$m during 2007.
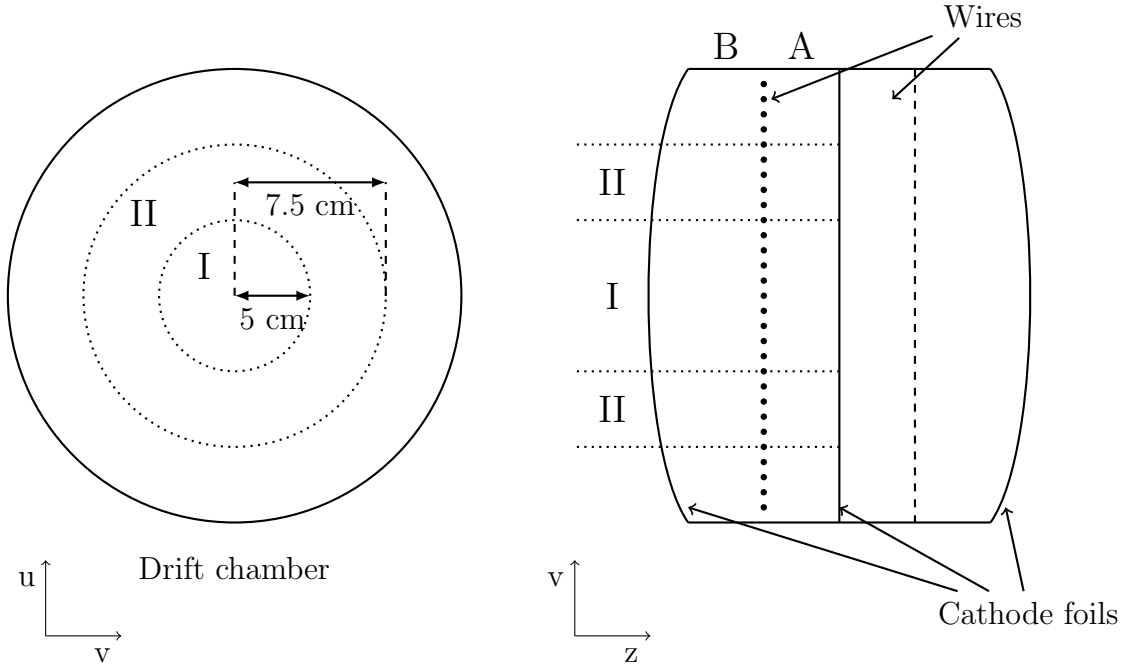
Figure 6.1: The differential pressure between the inside and the outside of a drift chambers module leads to a bulge of the outer cathode foil. In order to compare the bulge between different chambers, the average drift time on the side A of the wires is used as a reference. The foil bulge is given by a difference in average drift times: $\Delta T = (T_{\mathrm{IA}} - T_{\mathrm{IB}}) - (T_{\mathrm{IIA}} - T_{\mathrm{IIB}})$.

6.2   Wire time offsets in the drift chambers

The hit times in the wire chambers must be corrected to take into account the different propagation times of the signal between the sense wire and the TDC due to cable lengths and electronic components. This wire time offset affects the drift time and therefore the drift distance used during the track reconstruction. Also the decay time is extracted from the decay positron track reconstruction and a mismatch between the wire time offsets upstream and downstream of the stopping target would lead to an asymmetry resulting in a bias for the muon decay parameters.

For all previous TWIST measurements the wire time offsets were extracted from straight pion tracks without the solenoid magnet energized. These special pion data were taken only at the beginning and the end of the run periods due to the technical constraints of turning off the solenoid. Differences in time offsets between the beginning and the end of the run periods lead to significant systematic uncertainties for the previous measurements.
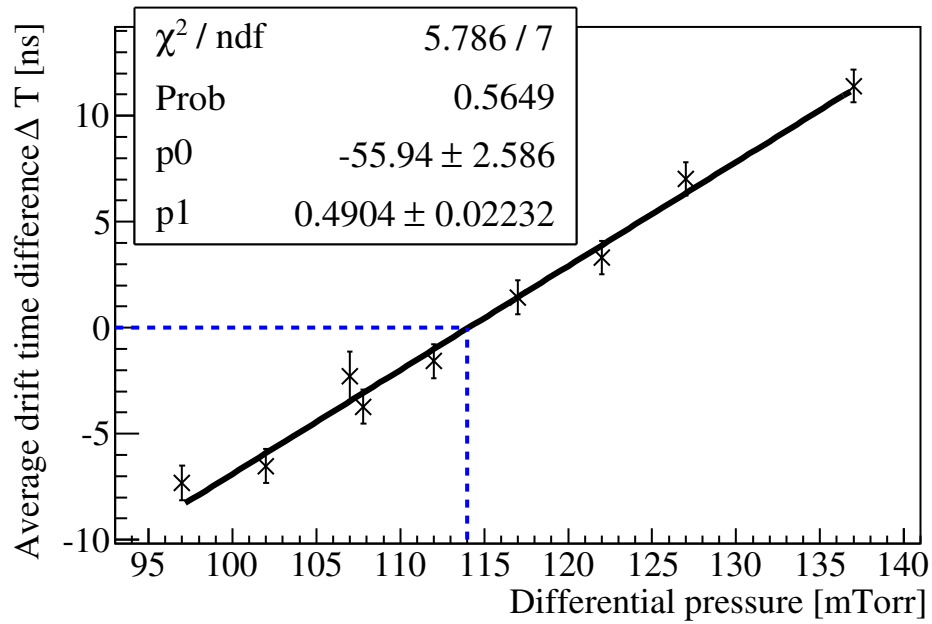
(a)
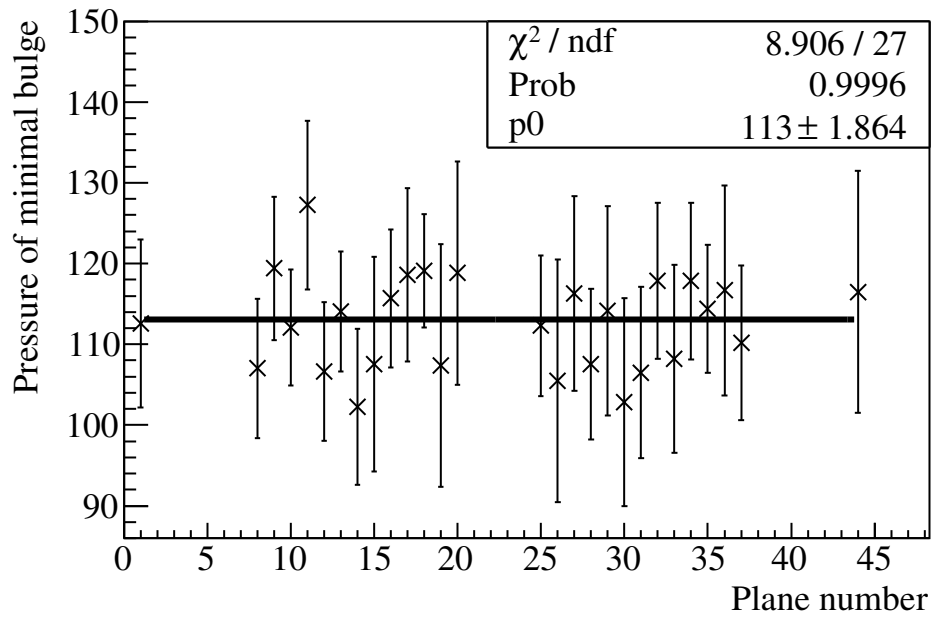
(b)

Figure 6.2: The cathode foil is flat if the difference between the average drift times of center and the outside of the chamber is zero . (for example for plane 13 on Fig. (a)). The pressure of minimum bulge is taken from an average for all the planes (Fig. (b)).

A new time offset calibration technique produces set dependent calibrations. The new technique uses the decay positrons and is therefore using the physics data directly. The wire time offset is determined with respect to the general time frame of the event. This is done indirectly by measuring the wire time offset with respect to two scintillators. The PU scintillator is used for the upstream decays and the downstream scintillator for the downstream decays.

A wire time offset is extracted from the rising edge of the hit time distribution with respect to the corresponding scintillator (Fig. 6.3). The hit time is corrected to take into account the time of flight of the decay positron from the drift plane to the scintillator. This correction depends on the angle of the track, which is determined with adequate precision by the first guess stage of the reconstruction. A fitting function composed of a Heaviside step function convoluted with a Gaussian distribution for the rising edge and an exponential decay for the falling edge extracts the midpoint of the rising edge. The function is written as:

$$f(t) = \frac{N}{2\pi\sigma} \times \exp\left(\frac{\sigma^2}{2\lambda^2} - \frac{t - k}{\lambda}\right) \times \mathrm{erfc}\left(\frac{k - t + \frac{\sigma^2}{\lambda}}{\sqrt{2}\sigma}\right) + B \tag{6.1}$$

with N the normalisation factor, k the edge of the step function, λ the relaxation time of the exponential decay, σ the width of the Gaussian convoluted and B a flat background.

The calibration technique was validated using MC. The difference between the input and the output is less than 1 ns. It is mostly due to the fact that the parameter k in Eq. 6.1 is not exactly the middle of the rising edge. For this reason a constant pedestal appears between input and output time offsets which is unimportant since the helix fitter uses drift times coming from time differences. The difference between the data and the MC time wire offsets is estimated by observing the difference of the fit parameter σ in the eq. (6.1) which represents the steepness of the rising edge. The mismatch of this parameter is less than 0.3 ns downstream and 0.5 ns upstream of the target (Fig. 6.4). Therefore the mismatch between data and MC of the wire time offsets is estimated to be less than 0.5 ns over the entire spectrometer.

The relative calibration of the upstream and downstream halves of the detector uses beam positrons that traverse the whole detector and therefore leave hits in both halves. Only the five central wires of each wire chamber are used because beam positrons have very small transverse momenta. The upstream and downstream wire
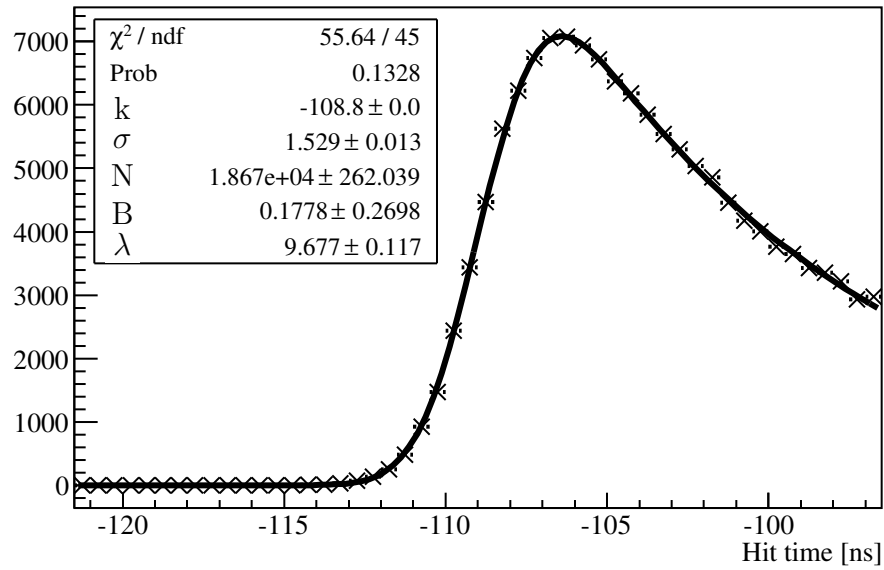
Figure 6.3: The average rising edge is extracted from a fit to the hit times on each wire. The parameter k defining the position of the step function is the value of the wire time offset for this wire.
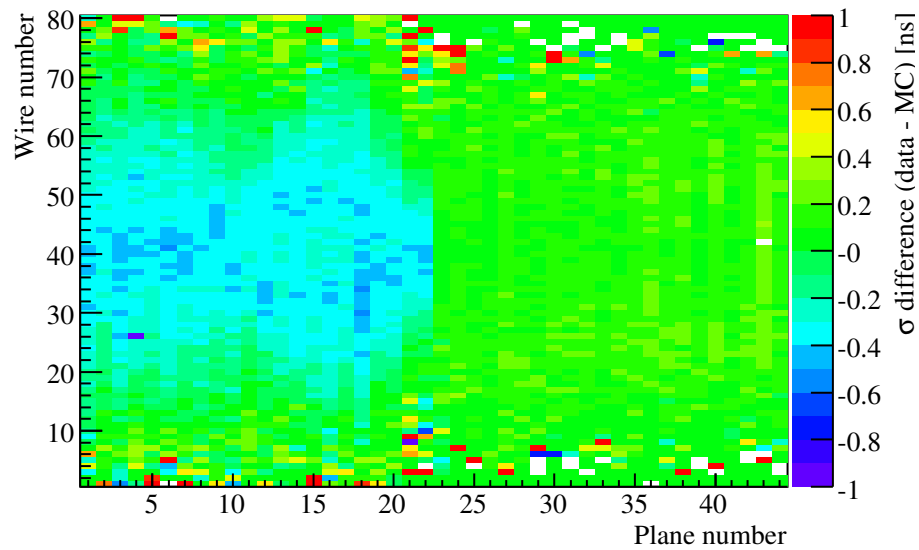
Figure 6.4: Difference between data and MC of the σ parameters of the line shape fit for each wire.

time offsets from the beam positrons are all measured relative to the DS scintillator. In order to extract the asymmetry between the two halves of the detector, for each wire the decay positron time offset is subtracted from the beam positron time offset. The resulting difference contains the biases from the two time offset measurements on both halves plus the difference in time between the PU and the DS scintillators for the upstream half. Similarly to the decay positron measurement, the beam positron measurement was validated using MC (Fig. 6.5). The measured asymmetry is equal to (13 ± 16)ps which is consistent with zero. Therefore the input and the measured asymmetry are consistent.

A possible uncertainty in the asymmetry measurement originates from the uncertainty on the position of the PU and the DS scintillators used for the wire time offset measurement. The position of the scintillators is known to a precision of 0.5 cm. The decay positrons travel more than 50 cm to reach the scintillators therefore the fractional uncertainty on the distance of flight of the positrons is 0.01. The average time of flight is about 8 ns therefore the corresponding uncertainty is 80 ps. A conservative uncertainty of 100 ps is assigned to the relative calibration of the upstream and downstream halves of the detector.
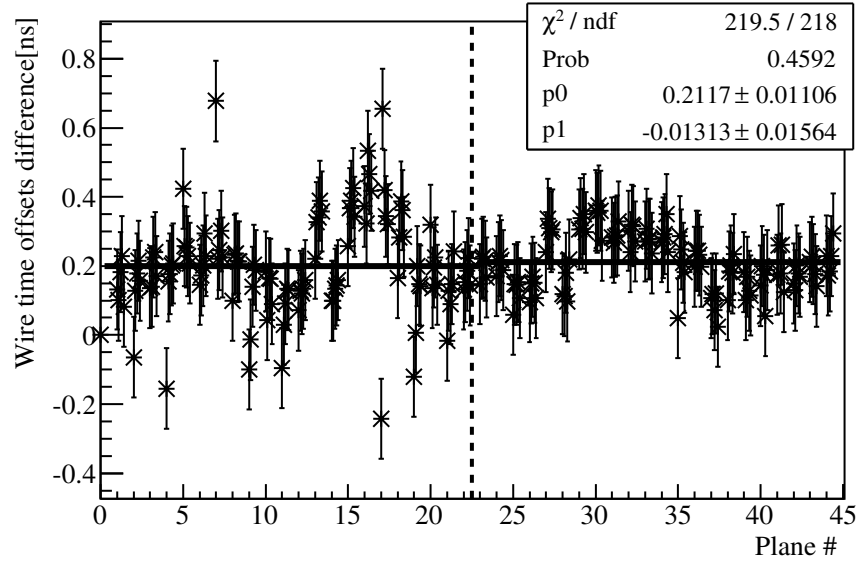
Figure 6.5: The MC wire time offset differences between the decay positron and the beam positron measurements are plotted versus the DC plane number. Five wires are used for each plane. The systematic effects are due to a different wire dependence between the two wire time offsets and should appear in both data and MC. The parameter p_1 represents the difference between upstream and downstream.

6.3   Drift chamber space time relationships

The Drift Chamber Space Time Relationships (DC STRs) are fundamental to the decay positron track reconstruction used to convert the drift time into a drift distance. The previous TWIST analyses used STRs extracted from Garfield simulations [47]. These STRs were the source of the leading systematic uncertainty for the previous δ measurement [17]). The analysis presented here uses STRs derived from the decay positron reconstruction.

The extraction of the STRs uses the Garfield STRs as a starting point. The drift volume around the wire, the cell, is divided into sub-cells. Decay positron tracks are reconstructed using the standard helix fitter. The time residuals of the hits in a sub-cell are entered in a histogram. For each sub-cell the mean of the time residual distribution is subtracted from the STRs used for the reconstruction. The new raw STRs cannot be used directly because they are not smooth enough to be physical. A spline fit over the whole cell corrects this problem and also creates the final STR table with a much finer granularity. The complete procedure is iterated until the average time residual distributions have converged to zero.

The STR tables include effects from the helix reconstruction algorithm. In order to perform the helix fit, the algorithm must assign a position in u or v (depending on the DC) and in z to each hit. A position on the drift time isochron is determined by finding the closest distance of approach to the wire (See Fig. 3.8). The possible positions on the isochron depend on the $\cos\theta$ of the track. For this reason the cell occupancy is correlated to the $\cos\theta$ reconstruction efficiency. In particular this creates zones in the cells where no hits are found due to the low reconstruction efficiency for tracks with $\cos\theta$ close to zero.

The STRs calibration procedure was applied to experimental data and MC. This allowed to include the helix reconstruction features for both the real detector and the MC. In particular the ionization of the gas in the DC cells is a discrete process. For this reason the closest distance of approach used in the helix fitter is only an approximation. Consequently the measured STRs are not the real STRs of the chambers but instead effective STRs including the effects of this approximation. For the analysis of the experimental data one STR table for each plane and for all the wires of the plane is created. These plane dependent STRs take into account the imperfections of the planes due to their construction and the bulge of the cathode foils under the differential pressure between the DCs and the cradle. Such imperfections do not exist
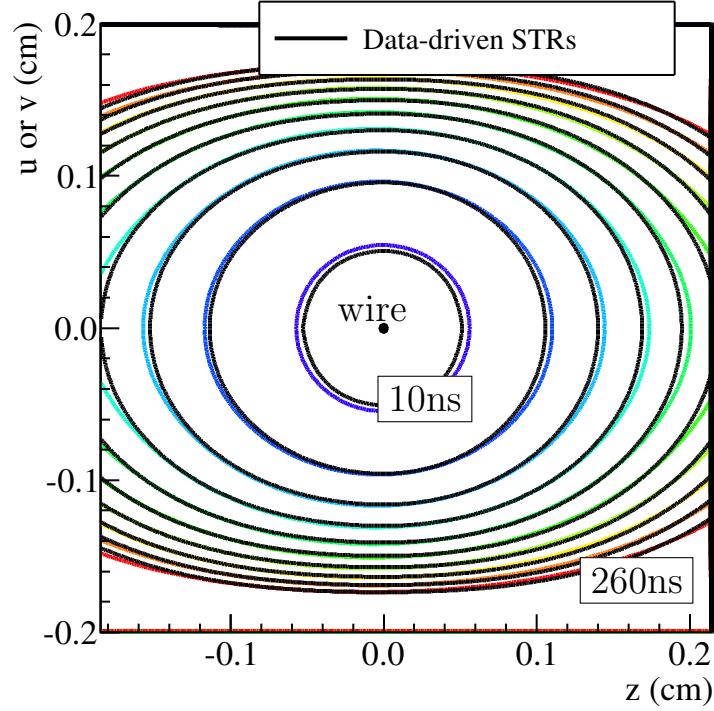
Figure 6.6: Isochrons of the STR tables from Garfield (in color gradient) and data-driven. Only the isochrons from 10 ns to 260 ns are displayed. The longest drift time in the cell is about 1000 ns. The cathode foils are located at -0.185 and 0.215 cm in z.

in the MC and consequently one STR table for all the planes and all the wires is sufficient.

The apparent difference between the Garfield simulated and the data-driven STRs tables is physically small (Fig. 6.6), but has a significant effect on the helix reconstruction (Fig. 6.7).

The previous analyses used a constant drift distance resolution of 100 μm across the whole cell. For this analysis a function describing the resolution with respect to the drift distance was determined by improving the momentum reconstruction resolution and bias in MC (Fig. 6.8). This drift distance resolution corresponds to an effective resolution including features from the helix fitter.

A change of the density of the DC gas alters the drift velocity and therefore the STRs. The relationship between the density and the STRs was studied on the data set 75. The study showed that multiplying all the drift times by a scaling factor function of the density is sufficient to correct for the density variations. The density correction is applied on a run by run basis using the slow control records of temperature and
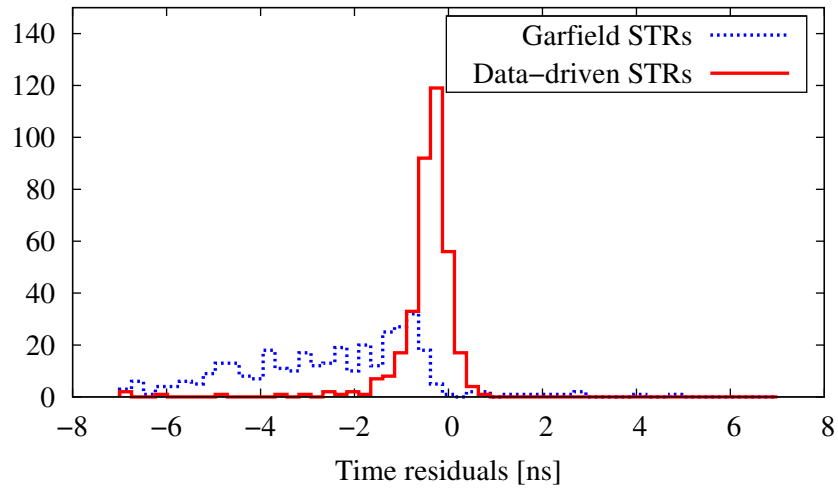
Figure 6.7: The time residuals show the clear improvement of the reconstruction due to the data-driven STRs. The data-driven STRs time residuals are almost centered on zero and the distribution is barely asymmetric.
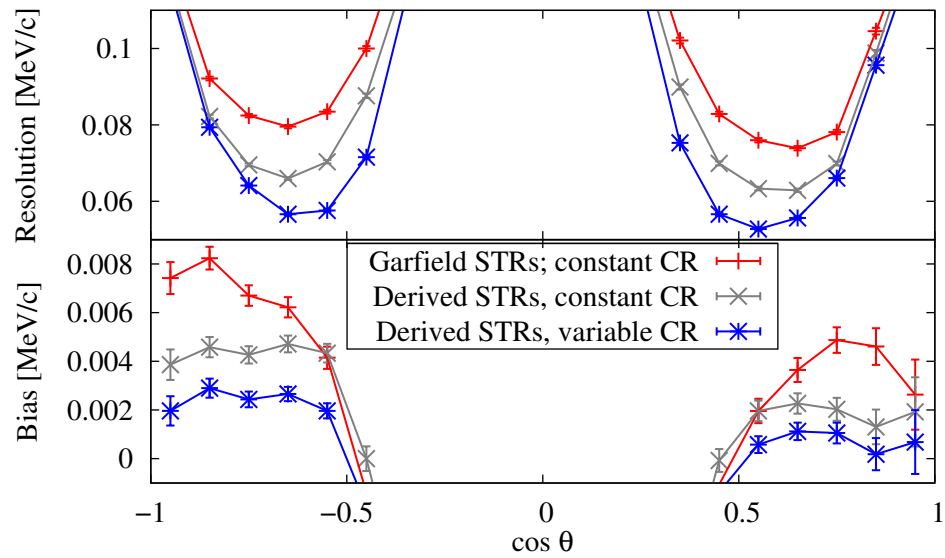
Figure 6.8: The derived STRs and the variable cell resolution (CR) are responsible for a net improvement of the momentum resolution and a reduction of the momentum reconstruction bias. The resolution and the reconstruction bias are measured in the MC using the true track angle and momentum.

pressure.

Chapter 7

Systematic uncertainties and corrections

The blind analysis scheme used for the measurement of the decay parameter δ requires that all the systematic uncertainties and corrections be evaluated prior to revealing the hidden parameters of the MC. None of the systematic uncertainties or corrections were modified after the end of the blind analysis. For the entire analysis of δ, the parameter η was fixed in the spectrum fit. The systematic uncertainty for δ from the correlation with η is 0.12×10^{-5} and therefore was dropped as too small to influence the total uncertainty. The analysis of the parameter η was not blind because the parameter used to generate the MC decay positrons was not hidden. However all the systematic uncertainties and corrections of δ were simply reevaluated by fitting η along with the other three decay parameters without any other modification. This gives us confidence that possible human biases were greatly reduced although the analysis was not blind.

Most of the systematic uncertainties originate from a mismatch between the MC and the experimental apparatus or from the physics of the MC. These uncertainties are evaluated by purposely exaggerating the mismatch in an MC simulation and measure the change in decay parameter between this modified MC set and a standard MC set. The difference is the *sensitivity* of the decay parameter to this mismatch. The main purpose of the exaggeration is for the sensitivity to be statistically well determined. The ratio between the exaggerated mismatch and the estimation of the real mismatch is called the *scale factor*. The sensitivity is scaled down by the scale factor in order to provide the systematic uncertainty.

Similarly a data set or an MC set can be analyzed with one component of the analysis exaggerated to test the sensitivity to this component. The change in decay parameter is then measured between two different analyses of the same set. The advantage of this technique is that the same events are fitted against each other except for the distortion from the exaggerated analysis. For this reason the statistical uncertainty from the fit can be renormalized to take into account the correlation by a factor of

$$R = \sqrt{\frac{\chi^2}{dof}} \qquad (7.1)$$

where dof is the number of degrees of freedom of the spectrum fit. In this chapter the sensitivities will be presented with their statistical uncertainties renormalized if it applies along with the Statistical Uncertainty Renormalization Factor (SURF) used.

The evaluation of the systematic uncertainties and the corrections will be explained in detail for the δ parameter. Only the sensitivities are reevaluated and presented for the η parameter. The method and therefore the scale factor and SURF of each systematic uncertainty are identical for both parameters. The corrections are also simply reevaluated with the η parameter as a free parameter of the spectrum fit. By following this procedure, the eta analysis was thus also not biased by our expectations.

7.1 δ systematic uncertainties

All the systematic uncertainties presented in this section are global to all the data sets. They are summarized in Tab. 7.1.

7.1.1 Positron interaction

Bremsstrahlung rate

As it is traversing the spectrometer, a decay positron can emit one or more photons which decelerates the positron. This emission, called bremsstrahlung, affects the momentum vector of the decay positron and therefore affects the momentum reconstruction in two ways. First of all it can modify the momentum between the muon decay vertex and the first DC encountered changing the momentum-angle spectrum of the measured tracks. Secondly the change in momentum due to the bremsstrahlung can be large enough to lead to the identification of two independent tracks (before

Systematic uncertainty	Section	Value ($\times 10^{-4}$)
Positron interaction	7.1.1	
Bremsstrahlung		1.59
δ ray		0.06
Outside material		0.13
Reconstruction resolution	7.1.2	
Momentum		0.70
Angle		0.06
Momentum calibration	7.1.3	
Propagation model		1.08
End points fits		0.54
Field map	7.1.4	0.06
Pulse width cut	7.1.5	0.04
Spectrometer alignment	7.1.6	
Width scale (u and v)		0.10
Length scale (z)		0.34
Chamber response	7.1.7	
DC STRs		1.01
Cathode foil position		1.18
Efficiency asymmetry		0.70
Crosstalk		0.10
Wire time offset wire dependence		0.11
Wire time offset asymmetry		0.44
Radiative corrections	7.1.8	0.63
Total		2.85

Table 7.1: Systematic uncertainties of the decay parameter δ. The uncertainties are added in quadrature.

and after the bremsstrahlung, see Fig. 3.4) instead of one. In this case the accuracy of the track reconstruction is diminished due to the lower number of hits per track. The bremsstrahlung and therefore the corresponding effects on the reconstruction are simulated in the MC. The accuracy of the simulated bremsstrahlung rate depends on the accuracy of the `GEANT3` physics but also on the accuracy of the thickness of the cathode foil, the gas volume and the target in the spectrometer.

The MC set 441 is identical to the nominal MC set 474 except that the bremsstrahlung rate is a factor three higher. This allows for a measurement of the sensitivity of the decay parameters to the bremsstrahlung rate. The δ parameter difference between the sets 441 and 474 is $(132.8 \pm 4.8) \times 10^{-4}$.

The scale factor is evaluated by measuring the bremsstrahlung rate in the data sets and the MC sets. Events containing two reconstructed tracks from a single decay positron, referred to as broken track events, are easily identified and counted. Although the photon from the bremsstrahlung is not measured in the spectrometer, its momentum can be extracted from the difference in momentum between the two reconstructed tracks. The momentum of the photon is used to determine if the broken track is due to a bremsstrahlung or some other processes (Fig 7.1). The difference between data and MC is given by the ratio of broken track events normalized to the number of muons stopping in the target. The average ratio from all the data sets and their corresponding MC sets is equal to 1.024 ± 0.004. The ratio between the MC sets 474 and 441 is equal to 2.82 ± 0.02. This ratio is different from the exaggeration factor of 3.0 because of saturation effects. In fact if too many bremsstrahlung are emitted by one track, the track reconstruction algorithm cannot even identify two independent tracks but instead reconstructs one or no track. As a consequence less bremsstrahlung events are found in the MC with the exaggeration factor of 3.0 than expected. The scale factor is

$$\frac{3.0 - 1.0}{1.024 - 1.0} = 83.3. \tag{7.2}$$

Finally the systematic uncertainty for the bremsstrahlung is equal to $132.8 \times 10^{-4}/83.3 = 1.59 \times 10^{-4}$. Using the measured 2.8 instead of the exaggeration factor 3.0 for the scale factor changes the systematic uncertainty only by 0.2×10^{-4} which is not considered significant.
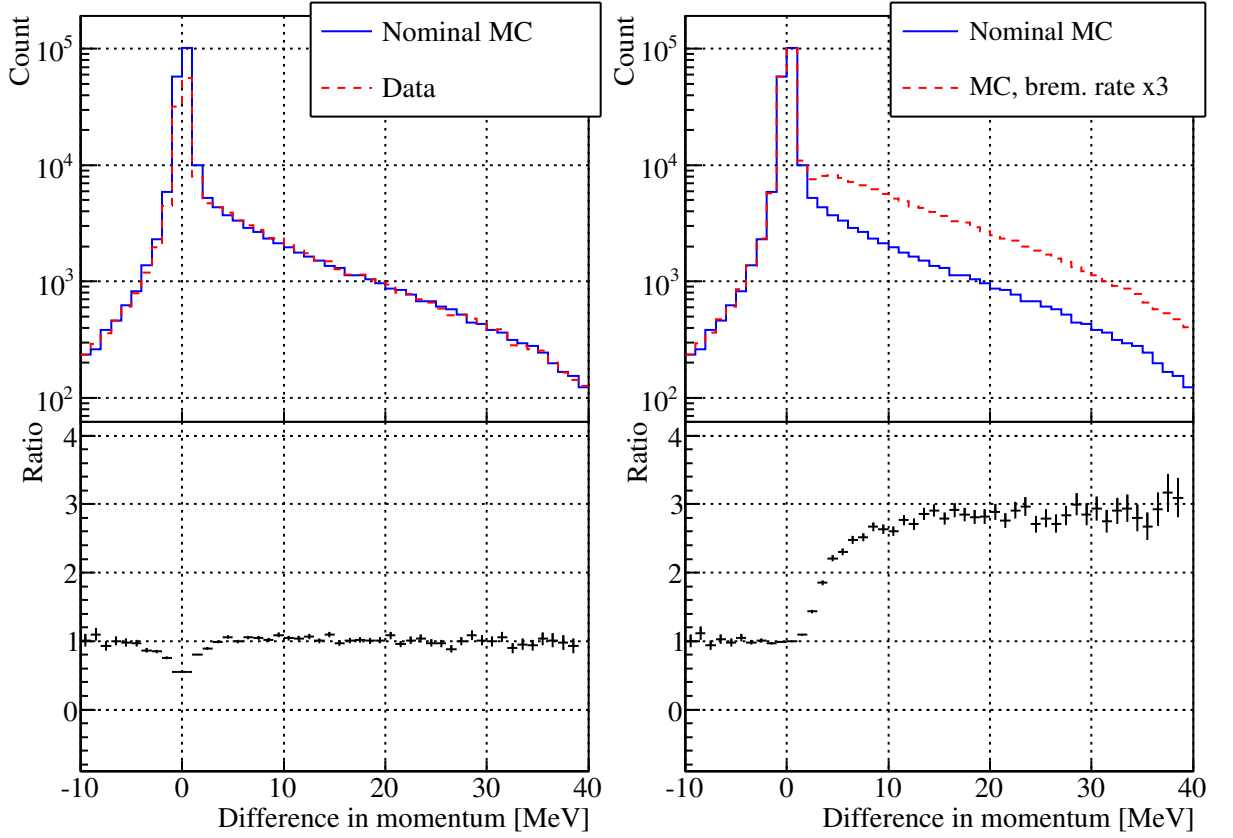
Figure 7.1: Number of broken track events versus the momentum difference between the two reconstructed tracks. The left hand side shows the nominal data set 74 and MC set 474. The right side shows the MC sets 474 and 441. The bottom plots correspond to the ratio of the two distributions above. This ratio is measured for each comparison in the momentum range $(15 < p < 35)$ MeV/c.

δ ray rate

The decay positron can knock out an electron from an orbital in an atom of the material traversed. Similarly to the bremsstrahlung, this physics process called δ ray production must be simulated accurately in the MC to integrate the change in decay positron momentum in the MC spectrum. Since the δ ray production and the bremsstrahlung have similar effects on the track reconstruction, their corresponding systematic uncertainties are evaluated in the same way. The main difference is that the higher energy tail of δ rays can be reconstructed in the spectrometer. For this reason the event topology used to measure the δ ray production rate is composed of two positively charged tracks from the decay positron and a negatively charged track

from the δ ray.

The MC set 440 has a δ ray production rate three times the rate of the MC set 474 but is otherwise identical to the nominal set. This exaggeration changes the decay parameter δ by $(-16.3 \pm 4.9) \times 10^{-4}$. The difference in δ ray production rate between two sets is again given by the ratio (Fig 7.2). The average ratio from all the data sets and their corresponding MC sets is equal to 1.007 ± 0.009. The ratio between the MC sets 474 and 441 is equal to 2.80 ± 0.04.

The systematic uncertainty is then

$$\frac{1.007 - 1.0}{3.0 - 1.0} \times -16.3 \times 10^{-4} = \pm 0.06 \times 10^{-4}. \tag{7.3}$$

Outside material

Decay positrons can scatter on material outside of the spectrometer and eventually enter back into the tracking region. The additional reconstructed tracks add confusion to the reconstruction algorithm, which reduces its efficiency and precision. The probability of a backscatter depends on the momentum vector of the decay positron. Therefore the positron backscatter affects only parts of the spectrum which can lead to a bias in the measurement of the decay parameters.

The data set 83 and its corresponding MC set 583 contain a downstream beam package (Sec. 2.1.4). In order to evaluate the sensitivity to the positron backscatter, the MC set 542 was generated identical to the MC set 583 but without a downstream beam package. In this context the downstream beam package acts as an exaggeration of the positron backscatter. The parameter δ changes by $(0.8 \pm 3.4) \times 10^{-4}$ between the MC sets 583 and 542.

The scale factor for this systematic uncertainty is evaluated using the time of flight measured by the PCs (Sec. 5.2.1). The difference in counts between the distributions of the time of flight normalized to the number of muons stopping in the target, represents the positron backscatter mismatch between two sets (Fig. 7.3). This difference is measured for all the data sets and their corresponding MC sets. The average mismatch in backscatter is -612 counts upstream and 326 counts downstream. Upstream and downstream backscatters are evaluated separately because for all the data sets, except for set 83, there is the upstream beam package on the upstream side and only the hole in the yoke on the downstream side. The amount of downstream backscatter is different by 4525 counts between the MC sets 583 and 542. The scale
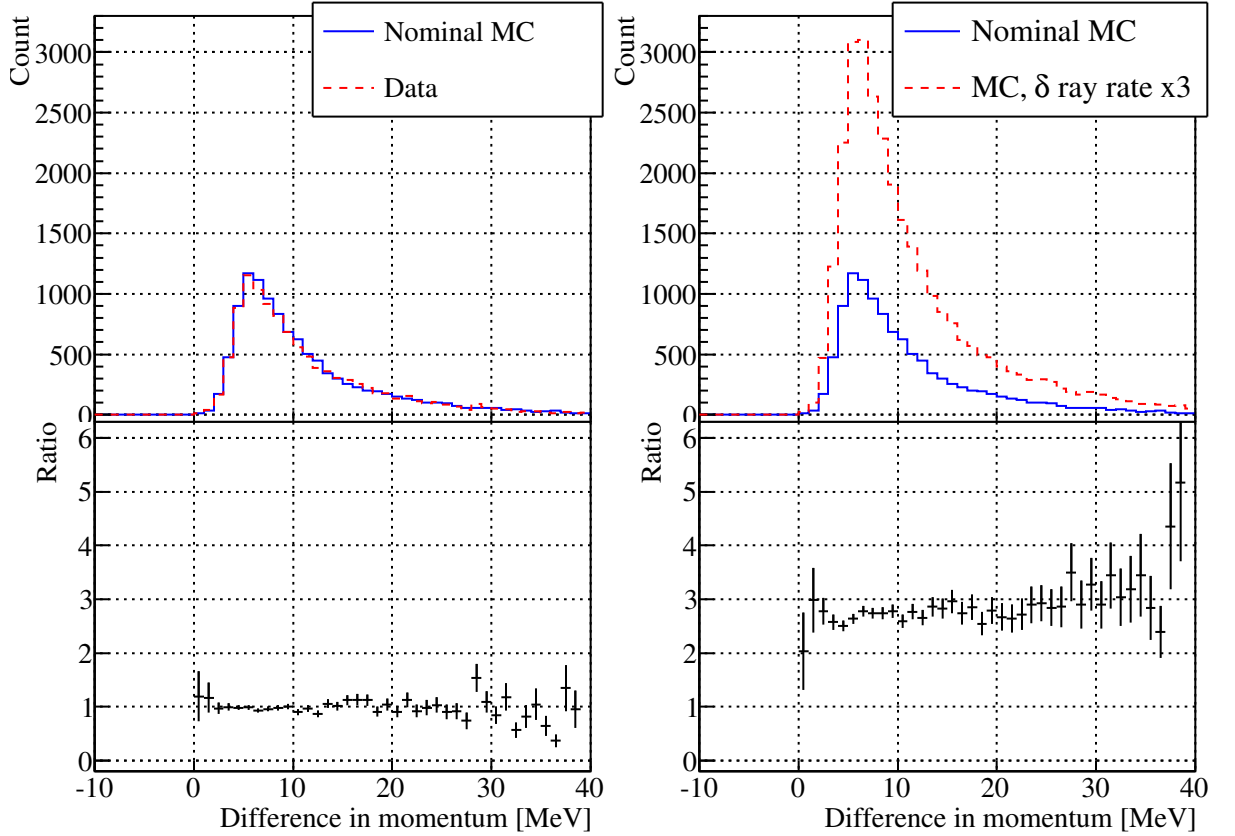
Figure 7.2: Number of events with a broken positively charged track plus one negatively charged track versus the momentum of the negatively charged track. The left hand side shows the nominal data set 74 and MC set 474. The right side shows the MC sets 474 and 440. The bottom plots correspond to the ratio of the two distributions above. This ratio is measured for each comparison in the momentum range $(6 < p < 16)$ MeV/c.

factor is $4526/612 \simeq 7$ for the upstream backscatter and $4526/326 \simeq 14$ for the downstream backscatter.

The upstream and downstream systematic uncertainties for the positron backscatter are added in quadrature. The total uncertainty for the mismatch in outside material is $\sqrt{(0.8/7)^2 + (0.8/14)^2} \times 10^{-4} = 0.13 \times 10^{-4}$.

7.1.2 Reconstruction resolution

The reconstruction resolution in momentum and angle is part of the detector response which modifies the momentum-angle spectrum. In particular the momentum reso-
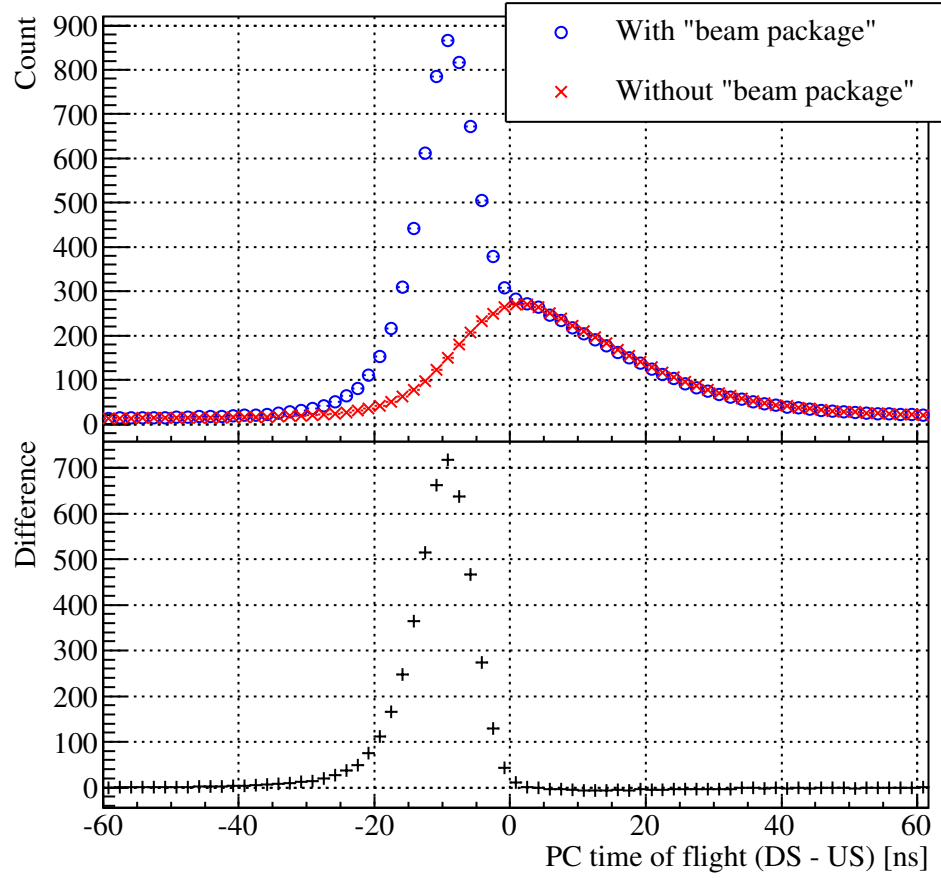
Figure 7.3: PC time of flight distributions for the MC sets 542 and 583, respectively without and with downstream beam package. The difference between the two distributions is plotted in the bottom half. The integral of the difference is equal to 4526.

lution affects the kinematic end-point by modifying its shape. The data and MC kinematic edges are fitted against each other in the momentum calibration. A mismatch between the data and MC edge shapes would lead to a systematic bias in the determination of the momentum calibration and therefore to a systematic bias in the decay parameter measurement.

The data and MC detector responses are studied with the upstream stops analysis in which muons are stopped far upstream of the target and the decay positrons travel through the entire detector (Sec. 5.5.2). The difference in momentum, Δp, and in angle, $\Delta\theta$, between the upstream and downstream tracks from the same decay positron are compared between data and MC. The distributions of Δp and $\Delta\theta$ are sensitive to the reconstruction resolution but also to other components of the spectrometer such

as the target thickness. However our approach is to assign all the measured difference between data and MC to the resolution.

Distributions of Δp and $\Delta\theta$ were extracted for various bins of $1/\sin\theta$ and momentum. The resolution in momentum (angle) is given by the width σ of a Gaussian fit to a distribution of Δp ($\Delta\theta$). The difference in resolution between data and MC is calculated such that:

$$\Delta\sigma = \begin{cases} \sqrt{\sigma_{\mathrm{data}}^2 - \sigma_{\mathrm{sim}}^2} & , \sigma_{\mathrm{data}} > \sigma_{\mathrm{sim}} \\ -\sqrt{\sigma_{\mathrm{sim}}^2 - \sigma_{\mathrm{data}}^2} & , \sigma_{\mathrm{sim}} > \sigma_{\mathrm{data}}. \end{cases} \tag{7.4}$$

The upstream stops analysis was performed with the silver and the aluminium targets, and no significant angular dependence or momentum dependence were found (Fig. 7.4). The constant mismatch in resolution over the entire spectrum was measured and is summarized Tab. 7.2. The resolution mismatches for the aluminium target are used to evaluate the systematic uncertainty for all the data sets because they are the largest of the two targets.

Target	$\Delta\sigma$ Momentum [keV/c]	$\Delta\sigma$ Angle [mrad]
Silver	-6.3	-0.07
Aluminium	-11.5	1.1

Table 7.2: Difference in reconstruction resolution between data and MC calculated according to Eq. (7.4).

The sensitivity to the resolution is evaluated by smearing the track angle or momentum in the spectrum reconstruction. The momentum and angle smearing are performed separately. The track momentum is smeared by 58 keV/c which corresponds to a scale factor of five. The decay parameter δ changed by $(-3.5\pm1.9)\times10^{-4}$ (SURF of 0.30) therefore the systematic uncertainty is $(-3.5/5)\times10^{-4} = \pm0.70\times10^{-4}$. Similarly the angle is smeared by 5.5 mrad for the same scale factor of five. The sensitivity to the angle resolution is $(0.6\pm2.4)\times10^{-4}$ (SURF of 0.38) which leads to a systematic uncertainty of $(0.6/5)\times10^{-4} = \pm0.12\times10^{-4}$.

7.1.3 Momentum calibration

As described in Section 3.3.3, the momentum calibration procedure determines the momentum mismatch between data and MC at the kinematic end-point. This mis-
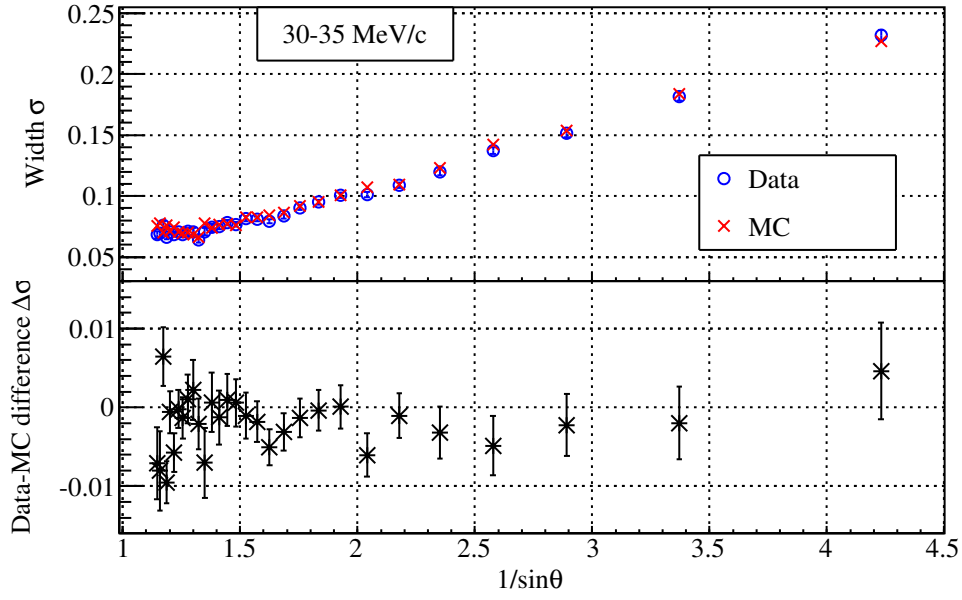
(a) Comparison of the momentum resolution for data and MC.
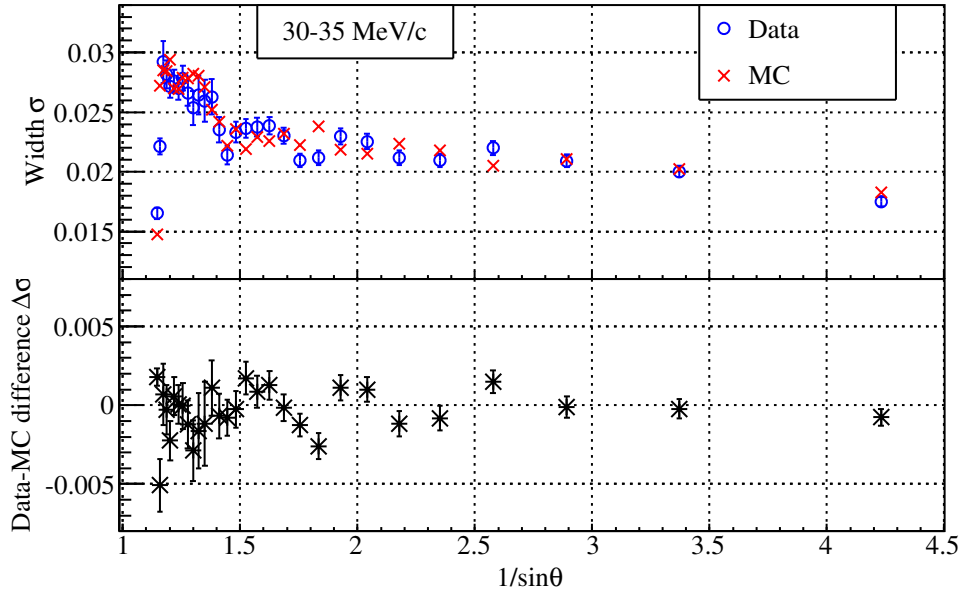
(b) Comparison of the angle resolution for data and MC.

Figure 7.4: The upstream stops analysis is used to measure the angle and the momentum resolutions with respect to the momentum and the angle of the positron track. These results are from silver target runs. Only the resolutions in a momentum range between 30 and 35 MeV/c are shown.

match is measured for bins of $1/\cos\theta$. The upstream and downstream linear dependences are fitted and defined by the intercepts at $1/\cos\theta = 0$ referred to as the offsets (b_{up} and b_{down}), and two slopes or angle dependences (a_{up} and a_{down}). Averaged over all the sets, the two slopes are about 0 keV/c and the intercepts are about 10 keV/c.

Propagation model

The momentum mismatch is measured only at the kinematic end-point but is corrected over the entire spectrum. The momentum dependence of this calibration depends on the source of the momentum mismatch between data and MC. For instance a mismatch in solenoid magnetic field strength leads to a momentum mismatch which depends linearly on the momentum and is referred to as a *scale*. Another example is a mismatch in target thickness which translates into a constant *shift* of the momentum with an angle dependence measured by the slopes a_{up} and a_{down}. The offset at the end-point of 10 keV/c could not be attributed to a unique source therefore the propagation of the momentum mismatch is eventually a mixture of *shift* and *scale*.

For this reason the decay parameters were computed for the two extreme cases of propagation which correspond to a pure *shift* with the form

$$p_{corrected} = p_{reconstructed} - \left(b - \frac{a}{|\cos\theta|} \right), \tag{7.5}$$

or a pure *scale*, given by

$$p_{corrected} = \frac{p_{reconstructed}}{1 + \frac{1}{W_{e\mu}}\left(b - \frac{a}{|\cos\theta|}\right)}, \tag{7.6}$$

where $W_{e\mu}$ is the maximum energy for the positron. The average values of the δ parameter using the *shift* and the *scale* propagations are different by 2.16×10^{-4}. The midpoint between these two extremes is used as the central value for δ so half of the difference between *shift* and *scale* is used as uncertainty to cover the two possibilities. The systematic uncertainty from the propagation model is 1.08×10^{-4}.

End points fits

The momentum mismatch between data and MC is assumed to be linear with respect to $1/\cos\theta$ based on geometrical considerations (Sec. 3.3.3). However the average value of the reduced χ^2 function ($\chi^2/ndof$) for the upstream linear fit is equal to

1.27. This indicates that the behavior of the mismatch is only linear in first order. The reduced χ^2 for the downstream end-point is consistent with one because of the larger statistical uncertainties which reduce the sensitivity to any non-linear behavior.

To take into account this non-linearity and to reduce the upstream reduced χ^2 to be one, one has to add in quadrature an uncertainty of 1.6 keV/c to the statistical uncertainty of the momentum mismatch at each $1/\cos\theta$ bin. The systematic uncertainty is evaluated in a conservative way first of all by applying this 1.6 keV/c uncertainty to both the upstream and the downstream half of the spectrum. Secondly this additional 1.6 keV/c uncertainty to the parameters b_{up} and b_{down} is then propagated to the decay parameters. The decay parameter δ changes by 0.54×10^{-4} which is the value used as the systematic uncertainty.

7.1.4   Field map

The accuracy of the momentum reconstruction relies directly on the accuracy of the solenoid field map. The solenoid magnetic field was scanned in 2002 using a custom built apparatus. Seven Hall probes measured the z component of the field while an NMR probe measured the total field. Multiple maps were measured with various conditions, in particular at the different field strengths of 1.96 T, 2.00 T and 2.04 T. The field was measured every 2.5 cm or 5 cm longitudinally, depending on the map. These maps are not fine enough to provide an accurate track reconstruction.

An `OPERA`[30] simulation modelling the solenoid and the magnetic parts of the apparatus provided a more detailed field map. This simulation was tuned to improve the agreement between the `OPERA` field map and the measured map. The match between measured and simulated maps is better than 0.2 mT in the tracking region.

In order to evaluate the systematic uncertainty, the difference between the measured and the simulated maps is parametrized by

$$\delta B_z = C_2 z^2 + C_3 z^3 + C_r r. \tag{7.7}$$

A modified `OPERA` map including this parametrization is fitted to the measured maps in order to extract the parameters C_2, C_3 and C_r [48]. The fit results for the three field strengths are summarized in Tab. 7.3.

The sensitivity of δ is evaluated using a 2 T magnetic field map including the parametrized difference δB_z multiplied by 20. The radial component B_r was also

Parameter	2.0T	1.96T	2.04T
C_2 ($\times 10^{-8}$ T/cm^2)	-1.7 ± 0.4	$+11.4 \pm 0.3$	-19.7 ± 0.5
C_3 ($\times 10^{-10}$ T/cm^3)	-7.8 ± 0.9	$+2.0 \pm 0.5$	-2.2 ± 0.7
C_r ($\times 10^{-6}$ T/cm)	-8.3 ± 0.3	-1.1 ± 0.6	-2.8 ± 0.9

Table 7.3: Fit parameters measuring the difference between the OPERA and the measured magnetic field maps using Eq. (7.7). The maps are different depending on the field strength.

modified according to

$$\delta B_r = -\left(C_2 r z + \frac{3}{2} C_3 z^2 r \right) \tag{7.8}$$

to satisfy Maxwell's equation $\nabla \cdot \delta \vec{B} = 0$. The data set 84 was reanalyzed with this modified map. The decay parameter δ changed by $(1.2 \pm 1.1) \times 10^{-4}$ (SURF of 0.18) between the nominal analysis and this new analysis. In this evaluation the scale factor is simply the exaggeration factor 20. Therefore the systematic uncertainty is 0.06×10^{-4} for the data sets taken with a 2.0 T magnetic field.

The data sets 70 and 71 were taken with the magnetic field strength at 1.96 T and 2.04 T, respectively. The parameters C_2, C_3 and C_r for these two maps are different by an order of magnitude from the parameters of the 2.0 T map. The systematic uncertainties for the 1.96 T and 2.04 T maps can be evaluated by scaling by an order of magnitude the uncertainty of the 2.0 T map. This leads to a systematic uncertainty of 0.6×10^{-4} on the individual sets 70 and 71 which is small compare to their statistical uncertainties of 5×10^{-4}. Furthermore the parameters C_2, C_3 and C_r have opposite signs therefore the systematic biases from the two sets eventually cancel out when the parameters δ is averaged out over all the data sets. For this reason only the 2.0 T systematic uncertainty is considered in the total systematic uncertainty.

7.1.5 Pulse width cut

The pulse width cut removes from the analysis the muons stopping in the PC 6 and not in the target (Sec. 4.2) modifying the muon stopping distribution in z. This affects the decay parameters in particular by changing the momentum calibration. The MC must reproduce this modification to prevent a bias in the decay parameters. This is tested by measuring the change in δ for two complete analyses with and

without pulse width cut over all the sets. This means that the cut is turned on or off for the data and the MC sets. The δ parameter changed by 0.04×10^{-4}. This entire difference is taken as a systematic uncertainty.

7.1.6   Spectrometer alignment

There are two types of misalignment to consider as a source of uncertainty for the decay parameters measurement. First of all the DCs and their wires can be randomly misaligned because of an inaccuracy in the alignment procedure (Sec. D.1). This affects randomly the hit positions along the tracks which degrades the reconstruction resolution. Therefore the systematic uncertainty from the reconstruction resolution already includes the uncertainty from a random misalignment in the spectrometer.

The other type of misalignment is for example if the DCs are offset in u or v linearly with respect to z leading to a "shear". Similarly the DCs can be rotated around the z axis in a "corkscrew" effect. These two possibilities were studied in the previous analysis of δ [37] and the systematic uncertainties were found to be less than 0.1×10^{-4}. For this reason they were not reevaluated for this analysis. Similarly the misalignment of the magnetic field map and the spectrometer was previously evaluated and found to be very small.

The length scale (z) of the spectrometer, used to measure the longitudinal component of the helices, has a precision of 50 μm over the 1 m [23]. This corresponds to a fractional uncertainty of 5.0×10^{-5}. A data set was reanalyzed with the longitudinal momentum modified by a fractional change of 1×10^{-3} in order to simulate the effect of the length scale uncertainty with an exaggeration factor of 20. The δ parameter changed by $(6.7 \pm 0.8) \times 10^{-4}$ (SURF of 0.20) and therefore the systematic uncertainty is $\pm 0.34 \times 10^{-4}$.

Similarly the width scale (u and v) affects the determination of the transverse momentum of the decay positron. The wires in the DCs were positioned with precision better than 5 μm over the 32 cm of the tracking region. This corresponds to a fractional uncertainty of 2×10^{-5}. This uncertainty was exaggerated by a factor 50 in an analysis where a fractional change of 1×10^{-3} was made to the transverse momentum of the reconstructed helices. The δ parameter changed by $(5.0 \pm 0.8) \times 10^{-4}$ (SURF of 0.19) which leads to a systematic uncertainty of $\pm 0.10 \times 10^{-4}$.

7.1.7 Chamber response

DC STRs

The accuracy of the helix reconstruction depends on the accuracy of the Space Time Relations (STRs). For this final analysis the STRs were measured from the same decay positron tracks used for the measurement of the decay parameters (Sec. 6.3). This STRs measurement technique is applied on both data and MC to ensure that the impact on the analysis of these STRs cancels out at the extraction of the decay parameters. However differences between the data and the MC STRs remain. They are evaluated by the time residuals (Tres) from the helix fitter.

The sensitivity to a mismatch in STRs is measured by creating MC STRs containing the difference in Tres between data and MC STRs.

1. 44 ΔTres are created by taking the difference between the data and the MC Tres.

2. The 44 ΔTres are fitted with a fifth order polynomial function to guarantee the smoothness of the STRs created in the next step.

3. 44 STR tables are created by adding the 44 polynomial functions exaggerated by a factor of ten to 44 duplicates of the MC STRs (since one STR table is used for all the planes in the standard MC analysis).

4. The MC set 584 is reanalyzed with these new STRs.

The sensitivity of δ to the STRs changes significantly if the propagation model for the momentum calibration is a *shift* or a *scale* (Sec. 7.1.3). For this reason the sensitivities from both models are averaged out and the total sensitivity is $(-13.7 - 15.8)/2 \times 10^{-4} = -14.75 \times 10^{-4}$.

The reconstruction resolution at the kinematic end-point is very different between the standard and these exaggerated-STR analyses of the MC set 584. This shows that the STRs are one possible source of mismatch in the reconstruction resolution between data and MC. The systematic effects of this mismatch, in particular on the momentum calibration at the end-point, are included in the sensitivities to the STRs. However the systematic uncertainty from the reconstruction resolution mismatch is already evaluated independently (Sec. 7.1.2). The systematic effect from the resolution must be subtracted from the sensitivities evaluated in this section to avoid double-counting.
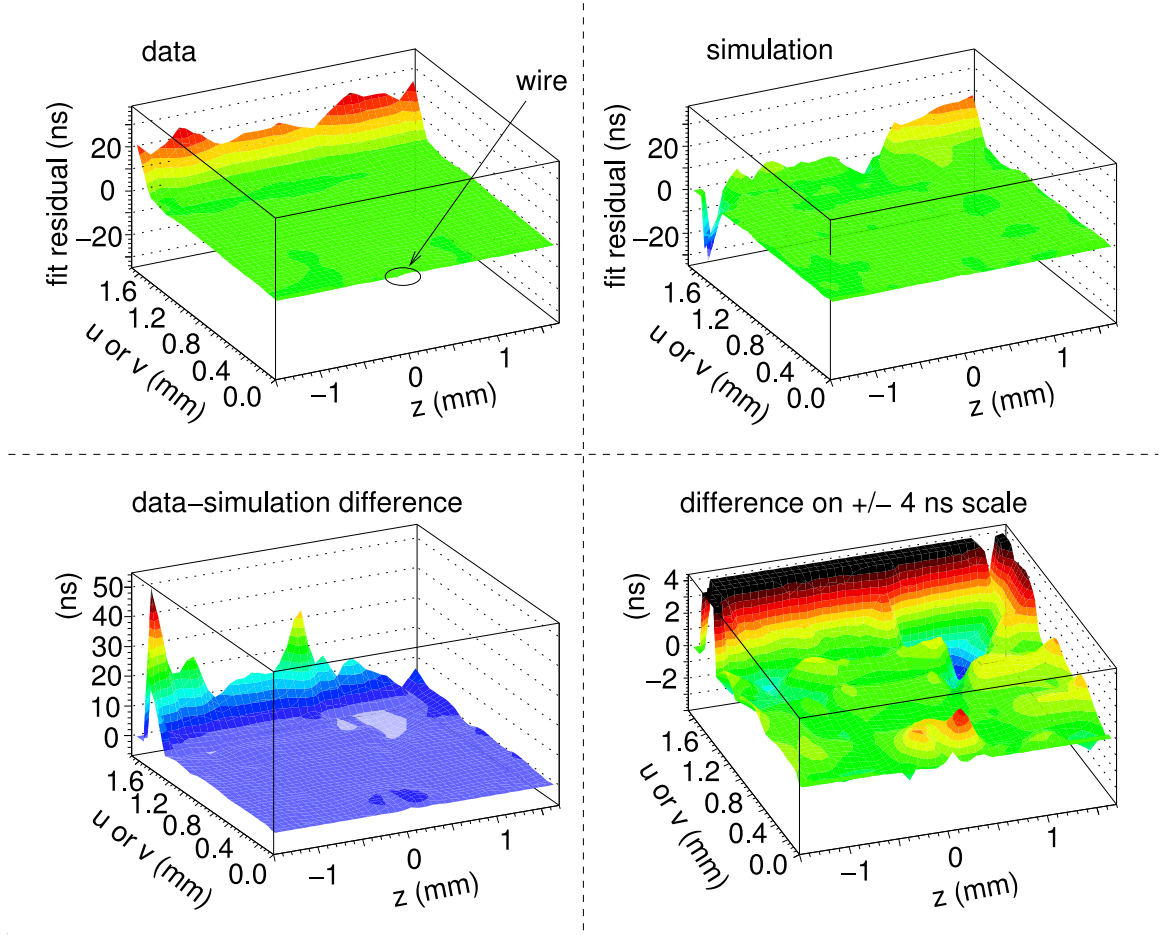
Figure 7.5:   The time residuals (Tres) are shown for only half of the drift cell in a DC because the STRs are reflected about $uv = 0$. The differences between the 44 data STRs (one per plane) and the global MC STRs (one common to all the planes) define 44 ΔTres.

In order to evaluate the amount by which the resolution contributes to the STRs sensitivity, one must measure the reconstruction resolution. This is done at the end-point where the shape of the spectrum is well known. The kinematic edge is fitted using an analytical function in which one of the fit parameters is the resolution (this fitting technique was used in the previous measurement as a momentum calibration technique [32]). Secondly the sensitivity of the reconstruction resolution is reevaluated with respect to the end-point resolution. The momentum is smeared in the spectrum reconstruction by 20, 40, 58 and 80 keV/c and the end-point resolution is measured for each smearing (Fig. 7.6). The end-point resolution of 77 keV/c for the reanalysis of the set 584 leads to a contribution to the sensitivity of -4.74×10^{-4}.
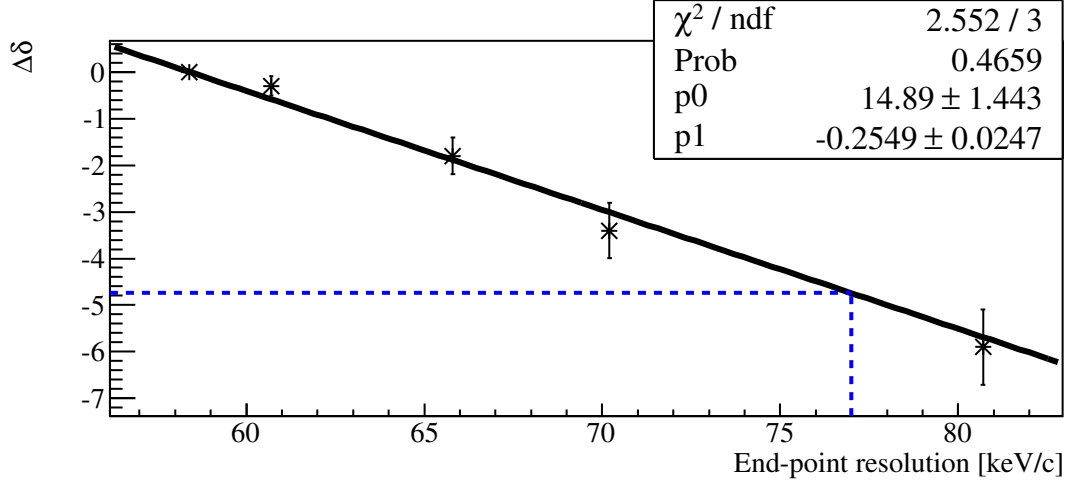
Figure 7.6: Contribution of the resolution to the δ sensitivity to the STRs versus the resolution measured at the kinematic end-point. The dashed lines correspond to the resolution of the exaggerated analysis of the MC set 584.

Finally the sensitivity is scaled down by the exaggeration factor of ten. The systematic uncertainty for the DC STRs is

$$\frac{-14.75 + 4.74}{10} \times 10^4 = 1.01 \times 10^{-4} \tag{7.9}$$

Cathode foil position

In the apparatus there are two different sources of uncertainty on the foil position. First of all there is an uncertainty due to the foil bulge from the differential pressure between the wire chambers and the cradle gas. The permanent foil bulge was (-60±22)μm (average) during the 2006 run period, and (8±22)μm during 2007 (Sec. 6.1). The second source of uncertainty comes from the construction of the chambers and was estimated to be 100 μm on average [49][50].

The position of the cathode foil affects the STRs of a chamber by changing the distance between the foil and the wire, modifying the electric field. Since the STRs are measured independently for each chamber, this effect is taken into account in the analysis. On the other hand a mismatch in cathode foil position between data and MC also means a mismatch in the size the drift cells. A DC with smaller (bigger) drift cells has a lower (higher) hit efficiency. In particular a decay positron can miss the corner of a drift cell if this cell has a reduced size. This has a direct impact notably

on the resolution of the right-left ambiguity in the helix fitter (Sec. 3.2.5).

The sensitivity of the δ parameter to the cathode foil position uncertainty was evaluated on MC by generating a simulation with cathode foils moved inward of the chambers by 500 μm. The fit of this MC set against the corresponding nominal MC set gives a sensitivity of $(5.9 \pm 4.4) \times 10^{-4}$. The cathode foils cannot be moved outward of the chambers because the STRs are defined only within the nominal drift cell. In this modified MC set the hit efficiency is reduced for all the planes but in reality certain drift cells are larger in data than they are in MC. Therefore this sensitivity measurement is an overestimate. For this reason the cathode foil position uncertainties from the bulge and the chamber construction are not added in quadrature but instead only the largest uncertainty of 100 μm is considered. The scale factor is $(500/100) = 5$ and the systematic uncertainty for δ is equal to $5.9/5 \times 10^{-4} = \pm 1.18 \times 10^{-4}$.

Upstream-downstream efficiency asymmetry

The track reconstruction efficiency is an important element of the detector response and therefore a match between data and MC is crucial. The measurement of the reconstruction efficiency is performed on upstream stops data (more details in Sec. 5.5.2). The difference in efficiency between data and MC is calculated in bins of momentum and angle. This provides the momentum and angle dependencies of the efficiency difference which is then used to evaluate the systematic uncertainty (Fig. 7.7).

The results for the silver and for the aluminium target are very similar (Tab. 7.4). The reconstruction efficiency do not appear to depend on the track momentum and for this reason the slope is fixed to zero.

The sensitivity is evaluated by modifying a spectrum according to the difference in efficiency between data and MC. First of all the difference in efficiency is multiplied by a factor ten. The bin contents of a data spectrum are then multiplied by the exaggerated difference in efficiency. This modified spectrum is fitted against the original spectrum. This is done for silver and aluminium but also for the angle and the momentum contributions independently. The constant momentum contribution is subtracted from the angle contribution prior to the evaluation of the sensitivity in order to avoid double-counting. The sensitivities are summarized in Tab. 7.5.

The average of the silver and aluminium sensitivities is scaled down by the scale
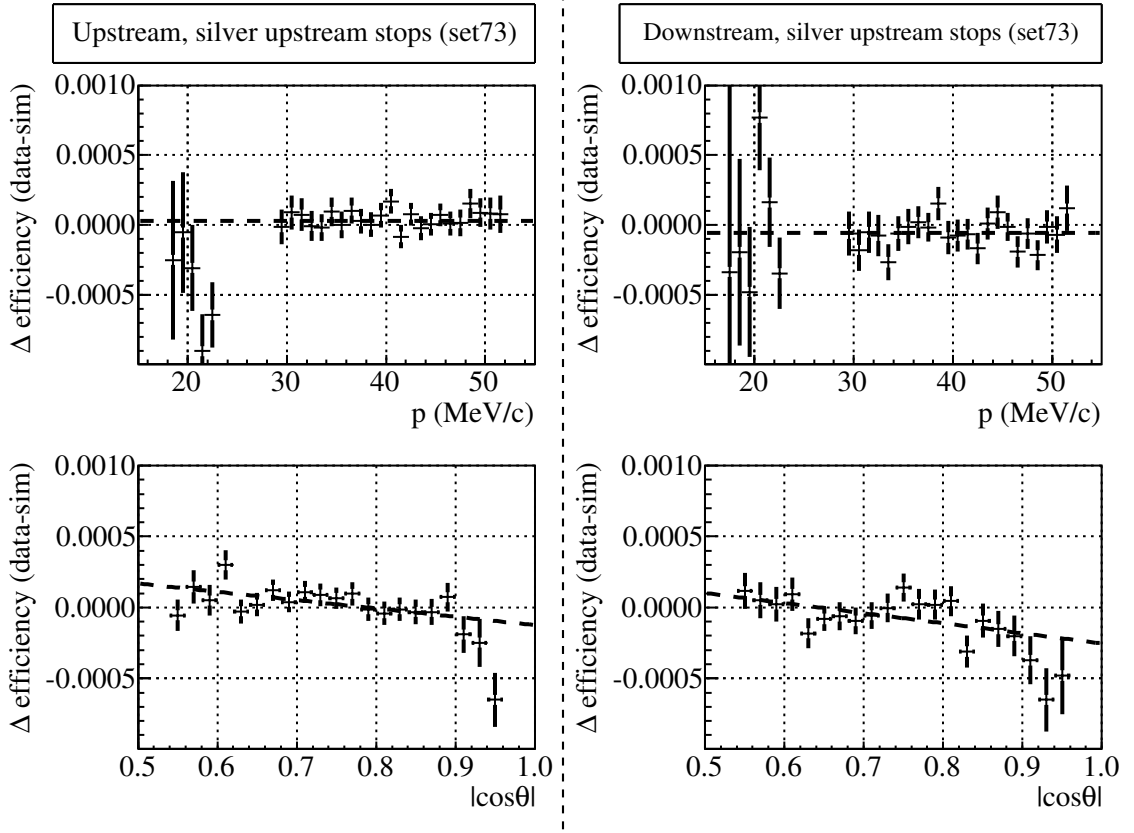
Figure 7.7: Profile plots of the difference between the track reconstruction efficiencies in data and MC for the silver target.

factor of ten. The angle and momentum contributions are added in quadrature. The systematic uncertainty is equal to $\pm 0.70 \times 10^{-4}$.

Crosstalk

The crosstalk signal in the apparatus is removed in the analysis (Sec. 3.2.2). On the other hand there is no crosstalk signal in MC. This difference could eventually lead to a systematic bias between data and MC. The sensitivity of the δ parameter is evaluated by turning off the crosstalk removal in the analysis of the data set 84. The spectrum from this analysis is fitted against the standard analysis of set 84 with the crosstalk removal active.

The efficiency of the crosstalk removal could not be evaluated directly. For this reason the entire difference $\Delta \delta = (0.10 \pm 1.27) \times 10^{-4}$ (SURF of 0.19) is considered to be an upper limit and is used as the systematic uncertainty from the crosstalk signal.

Silver		
	Upstream	Downstream
Angle slope	$(-5.9 \pm 2.0) \times 10^{-4}$	$(-7.1 \pm 2.5) \times 10^{-4}$
Intercept	4.6 ± 1.5	4.6 ± 1.8
Momentum intercept	$(0.30 \pm 0.20) \times 10^{-4}$	$(-0.58 \pm 0.25) \times 10^{-4}$
Aluminium		
	Upstream	Downstream
Angle Slope	$(-6.4 \pm 2.3) \times 10^{-4}$	$(-5.3 \pm 2.8) \times 10^{-4}$
Intercept	5.1 ± 1.7	3.5 ± 2.1
Momentum intercept	$(0.36 \pm 0.23) \times 10^{-4}$	$(-0.30 \pm 0.28) \times 10^{-4}$

Table 7.4: The efficiency difference versus momentum and angle are fitted independently. The slope is fixed to zero for the momentum dependence.

	Silver	Aluminium	Average
Angle contribution	-2.63 ± 0.07	-1.21 ± 0.06	-1.92 ± 0.09
Momentum contribution	8.74 ± 0.00	5.82 ± 0.00	7.28 ± 0.00

Table 7.5: Sensitivities of the δ parameter to the track reconstruction efficiency, in units of 10^{-4}. The angle and momentum dependence of the efficiency are evaluated separately. The SURF of 0.02 for the angle and 10×10^{-4} were applied here.

Wire time offsets

The wire time offsets are measured from the decay positron tracks on a set by set basis (Sec. 6.2). This prevents any uncertainty from a change in the time offsets because of changing experimental conditions. The systematic uncertainty from the wire time offsets comes from the accuracy of the procedure used to measure them. The true wire time offsets are known in MC. The measured and MC input offsets are compared and the difference between the two defines the wire dependent accuracy of the procedure (Fig. 7.8). As shown in Sec. 6.2, the σ coefficient describing the wire time offset line shapes is different by less than 0.5 ns over the entire spectrometer between data and MC. This guarantees that the accuracy of the measurement procedure is not different by more than 0.5 ns between data and MC. For this reason the difference between input and measured offsets in MC can be used to estimate the systematic uncertainty.

A set of wire time offsets was created by multiplying the difference between input and measured offsets seen in Fig. 7.8 by a factor of ten. This corresponds to an exaggeration of the inaccuracy of the offset measurement procedure. An MC set was
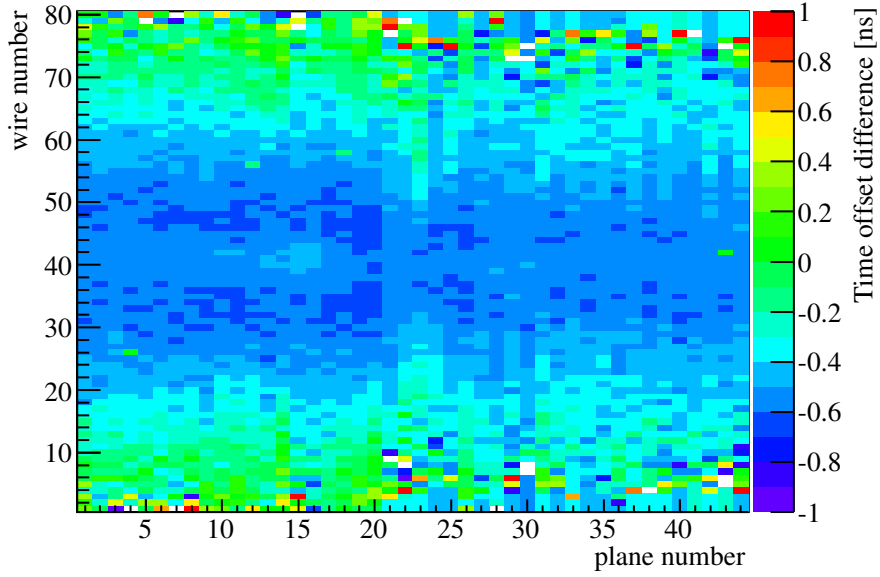
Figure 7.8: Difference between the input and the measured wire time offsets in MC.

reanalyzed with these new wire time offsets. The momentum-angle spectrum from this analysis was fitted against the standard analysis of this set. The difference in the decay parameter δ is equal to $(1.1 \pm 0.9) \times 10^{-4}$ (SURF of 0.15). The scale factor corresponds to the exaggeration factor of ten therefore the systematic uncertainty is $(1.1/10) \times 10^{-4} = \pm 0.11 \times 10^{-4}$.

Beam positrons are used for a relative calibration of the wire time offsets upstream and downstream because they traverse the entire detector. This calibration is performed after the individual wire time offsets have been determined therefore it requires a separate systematic uncertainty. An uncertainty of 100 ps comes from the uncertainty on the position of the scintillators used for the wire time offset measurement (Sec. 6.2). An MC set was reanalyzed using a set of wire time offsets with the downstream offsets shifted by 10 ns which gives a scale factor of 100. The δ parameter is different by $(-44.3 \pm 0.4) \times 10^{-4}$ (SURF of 0.07) between this reanalysis and the standard analysis. The systematic uncertainty of the detector asymmetry is then equal to $\pm 0.44 \times 10^{-4}$.

7.1.8 Radiative corrections

The generation of the decay positrons samples (using hidden parameters) for the MC include the following radiative corrections: full first order, $\mathcal{O}(\alpha^2 L^2)$, $\mathcal{O}(\alpha^2 L)$

and $\mathcal{O}(\alpha^3 L^3)$ where $L = \ln(m_\mu^2/m_e^2)$. The term $\mathcal{O}(\alpha^2)$ was evaluated by numerical integration over a momentum range (and over all angles) covering the TWIST fiducial region [51]. This numerical integration shows that in this region the $\mathcal{O}(\alpha^2)$ term has a similar shape, five times smaller than the $\mathcal{O}(\alpha^2 L)$ term. For this reason we use the $\mathcal{O}(\alpha^2 L)$ term to evaluate the systematic uncertainty for the absence of the $\mathcal{O}(\alpha^2)$ term.

The following steps provide the sensitivity to the $\mathcal{O}(\alpha^2)$:

1. A spectrum of pure radiative correction (RC) of order $\mathcal{O}(\alpha^2 L)$ is produced.

2. The spectrum RC is normalized and added to the MC set 447 to create a new spectrum (447+RC).

3. The spectrum 447+RC is fitted against the MC set 447.

The decay parameter δ changes by $(-3.50 \pm 0.05) \times 10^{-4}$ (SURF of 0.01). The scale factor is given by $5 \times 1.11 = 5.55$ where 5 is the relative size of the $\mathcal{O}(\alpha^2 L)$ term and the $\mathcal{O}(\alpha^2)$ term, and 1.11 is the ratio of counts between the two spectra 447 and 447+RC. The systematic uncertainty for the missing radiative corrections is $(-3.50/5.55) \times 10^{-4} = \pm 0.63 \times 10^{-4}$.

7.2 δ statistical uncertainties

The statistical uncertainty of the decay parameters on individual sets is calculated by the `MINUIT` algorithm of the spectrum fit.

The momentum calibration and the decay parameter fit use two different regions of the momentum-angle spectrum. The former is performed on the kinematic endpoint with momenta greater than 52.3 MeV/c. The decay parameters are extracted from the fiducial region located below 52.0 MeV/c. Therefore the two procedures use different events and are statistically independent. For this reason the statistical uncertainty from the measurement of the momentum calibration parameters (a_{up}, b_{up}, a_{down}, b_{down}) must be propagated to the decay parameters.

This propagation is performed using a sensitivity matrix. The elements of this matrix are calculated by applying a momentum calibration with one of the calibration parameters at 100 keV/c and by fitting this calibrated set to the same set uncalibrated. The change in decay parameter is scaled down by 100 to obtain the sensitivity to a

Data set	Statistical uncertainties ($\times 10^{-4}$)		Corrections ($\times 10^{-4}$) momentum calibration applied	
	Spectrum fit	Momentum calibration	as a shift	as a scale
68	6.18	0.44	-0.50	-0.49
70	5.10	0.36	-0.45	-0.44
71	5.36	0.38	-0.46	-0.45
72	5.22	0.37	-0.41	-0.40
74	6.09	0.44	-0.53	-0.51
75	5.19	0.37	-0.43	-0.42
76	5.70	0.40	-0.48	-0.47
83	5.32	0.37	-0.39	-0.38
84	5.58	0.39	-0.42	-0.41
86	5.07	0.35	-0.31	-0.30
87	5.47	0.39	-0.41	-0.40
91	10.46	0.86	-0.50	-0.48
92	9.03	0.69	-0.52	-0.51
93	7.37	0.54	-0.48	-0.37

Table 7.6: Statistical uncertainties and corrections for the decay parameter δ for each data set.

change of 1 keV/c of the calibration parameter. The correlation matrix between the calibration parameters is also required for the propagation of the uncertainty.

The spectrum fit uncertainties and the propagated uncertainties from the momentum calibration are summarized in the Tab. 7.6. These uncertainties are added in quadrature for each set.

7.3 Corrections to the δ parameter

A consistency check on the spectrum fitter and the momentum calibration showed that both algorithms are sensitive to the ratio of the number of events in the data and the MC spectra. This bias is attributed to the fact that the probability distribution of a bin content in a spectrum is a difference of Poisson distributions which is not symmetric.

The residuals calculated in the χ^2 function take the difference between each bin in the data and MC spectra. In the situation where data and MC spectra have the same number of events, the difference of the two identical asymmetric Poisson distributions of the two bins leads to a symmetric probability distribution for the

residuals. However all the MC sets contain more events than their corresponding data set in order to reduce the statistical uncertainty of the decay parameters. This creates an asymmetric distribution for the residuals and a bias in the χ^2 minimization which is used by the spectrum fitter and the momentum calibration.

The biases of the two algorithms were evaluated with the same technique, individually on each pair of data and MC sets. The MC set was divided into subsets containing a number of events matching the data set. Each subset was fitted against the data set and the resulting fit parameters were averaged because these fits are performed on equal numbers of data and MC events and they therefore do not have the bias. For each parameter, the difference between the subsets average and the results using the whole MC set corresponds to the bias.

The measured biases for the spectrum fitter vary from set to set between 0.0 and -0.25×10^{-4} with an average of -0.05×10^{-4}. The average bias was corrected on the final result of δ rather than on a set by set basis because of the small size of the correction. The bias on the momentum calibration parameters was propagated to the decay parameters using the sensitivity matrices already evaluated for the statistic uncertainties. Since this propagation depends on the way the momentum calibration is applied to the spectrum, the corrections for both *shift* and *scale* were calculated (Tab. 7.6).

The validity of the measured biases was verified using other measurement techniques which are not presented here. The uncertainties of the corrections of the spectrum fit and the momentum calibration are less than 0.2×10^{-4} and were considered too small to be included in the systematic uncertainties table.

7.4 η uncertainties and corrections

The systematic uncertainties for the measurement of the η parameter are summarized in Tab. 7.7. The statistical uncertainties and corrections are summarized in Tab. 7.8.

The η sensitivities are calculated by fitting the same spectra used for the δ sensitivities with all four parameters free. Those sensitivities included in Tab. 7.7 are sufficient to recalculate the uncertainties from their descriptions for the δ parameter in Sec.7.1. The systematic uncertainties for the propagation model of the momentum calibration and the pulse width cut used the same analyses as the evaluation for δ. These analyses were simply refitted with η as an additional fit parameter.

A new matrix propagating the momentum calibration parameters to the decay

Systematic uncertainty	Section	Sensitivity ($\times 10^{-3}$)	Value ($\times 10^{-3}$)
Positron interaction	7.1.1		
Bremsstrahlung		441.61 ± 49.57	5.32
δ ray		-64.80 ± 49.44	0.23
Outside material		50.08 ± 34.68	7.15
Reconstruction resolution	7.1.2		
Momentum		8.83 ± 19.37	1.77
Angle		7.32 ± 24.53	1.46
Momentum calibration	7.1.3		
Propagation model			1.69
End points fits			2.39
Field map	7.1.4	-69.19 ± 11.67	3.46
Pulse width cut	7.1.5		10.60
Spectrometer alignment	7.1.6		
Width scale (u and v)		31.97 ± 8.12	0.64
Length scale (z)		74.84 ± 8.54	3.74
Chamber response	7.1.7		
DC STRs			6.00
Cathode foil position		59.28 ± 44.83	11.86
Efficiency asymmetry		17.69 ± 4.50	1.77
Crosstalk		11.71 ± 12.35	11.71
Wire time offset wire dep.		2.42 ± 8.52	2.42
Wire time offset asymmetry		2.75 ± 3.90	0.03
Radiative corrections	7.1.8	-17.20 ± 0.55	3.09
Total			23.76

Table 7.7: Systematic uncertainties of the decay parameter η.

Data set	Stat. uncertainties ($\times 10^{-3}$)		Corrections ($\times 10^{-3}$)		
	Spectrum fit	Momentum calibration	Spectrum fit	Momentum calib. applied as a shift	as a scale
68	62.54	0.79	4.52	4.83	-1.47
70	51.52	0.71	1.91	3.08	-0.94
71	54.25	0.68	1.95	3.42	-1.00
72	52.93	0.68	1.58	3.14	-0.95
74	61.57	0.82	3.24	6.19	-1.89
75	52.51	0.65	2.12	3.12	-0.94
76	57.48	0.74	2.28	4.66	-1.46
83	53.79	0.77	1.09	3.05	-0.94
84	56.35	0.80	0.02	3.41	-1.01
86	51.08	0.71	1.06	0.81	-0.24
87	55.39	0.70	1.38	3.31	-1.00
91	105.93	1.64	7.40	5.22	-1.57
92	91.20	1.23	5.48	7.60	-2.22
93	74.33	0.89	2.87	4.01	-1.19

Table 7.8: Statistical uncertainties and corrections for the decay parameter η for each data set.

parameters was calculated to include η; it was used to calculate the end points fits uncertainty, the statistical uncertainties and the corrections of the momentum calibration statistical bias. The spectrum fit correction is applied on a set by set basis for η because its size is similar to the size of the momentum calibration correction.

Chapter 8

Results and conclusion

8.1 Results of the measurement of δ

The three decay parameters ρ, δ and $P_\mu\xi$ were measured simultaneously however only δ is presented here. The results for ρ and $P_\mu\xi$ can be found respectively in [29] and [31].

8.1.1 Blind analysis results

The data sets are independent measurements of the decay parameters and their results are averaged out. The weight of the individual sets is set according to the statistical uncertainties summarized in Tab. 7.6. The corrections were also applied prior to the extraction of the average.

As described in Section 7.1.3, the reconstruction of the spectrum was performed twice using *shift* or *scale* as propagation models for the momentum calibration. The final value of δ is the average of the results from these two analyses (Tab. 8.1 and Fig. 8.1). The correction of -0.05×10^{-4} from the spectrum fit bias due to the unequal number of events in data and MC is added to the final value.

The result of the blind analysis is:

$$\Delta\delta = \Big(51.34 \pm 1.57(\text{stat.}) \pm 2.85(\text{syst.})\Big) \times 10^{-4}. \tag{8.1}$$

Once the collaboration agreed on the end of the blind analysis, the hidden value

| Data set | $\Delta\delta$ ($\times10^{-4}$) momentum calibration applied | | Statistical uncertainties ($\times10^{-4}$) |
	as a shift	as a scale	
68	43.46	41.49	6.20
70	59.34	57.09	5.11
71	58.70	56.99	5.37
72	44.72	42.87	5.23
74	56.78	54.69	6.11
75	56.42	54.82	5.20
76	47.67	45.48	5.71
83	44.95	42.31	5.33
84	52.15	49.51	5.59
86	59.95	57.59	5.08
87	47.52	45.29	5.48
91	38.11	35.96	10.50
92	56.03	53.24	9.06
93	61.31	58.92	7.39
Weighted average	52.47	50.30	1.57

Table 8.1: Difference between data and MC, $\Delta\delta$, for each data set and for the weighted average. The statistical uncertainties correspond to the quadratic sum of the spectrum fit and the momentum calibration uncertainties (Tab. 7.6). Both analyses use the same data so their statistical uncertainties are the same.

of δ was revealed on the 29th of January 2010 as:

$$\delta_{\text{hidden}} = 0.74559 \tag{8.2}$$

Finally the result for the measurement of δ is the addition of the blind analysis and the hidden values which gives:

$$\delta = 0.75072 \pm 0.00016(\text{stat.}) \pm 0.00028(\text{syst.}). \tag{8.3}$$

This result is consistent with the previous measurements of TWIST [16][17](See Sec.1.4.1) and the measurement prior to TWIST by B. Balke et al. [15] as shown in Fig. 8.2. This measurement is more precise by a factor of 11.5 than the measurement by Balke and therefore it achieves the original goal of the collaboration of an order of magnitude improvement. The Standard Model prediction of 0.75 is 2.2 standard deviations away from our measurement.
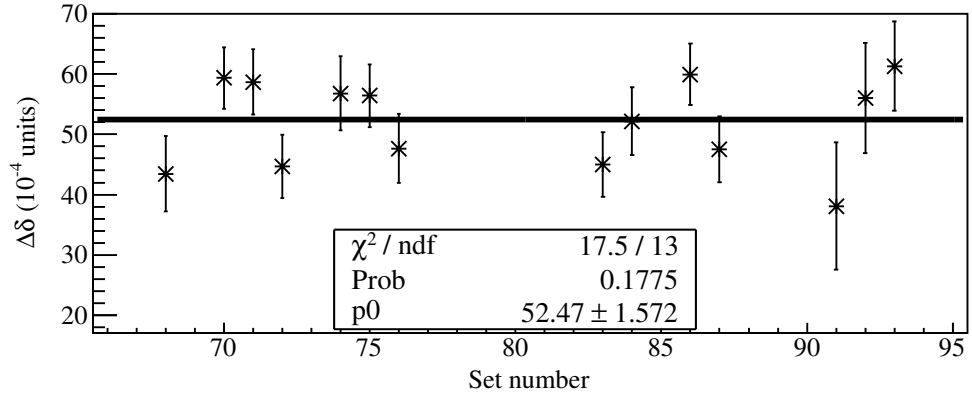
(a) Difference between data and MC for the analysis using the shift as the momentum calibration propagation model.
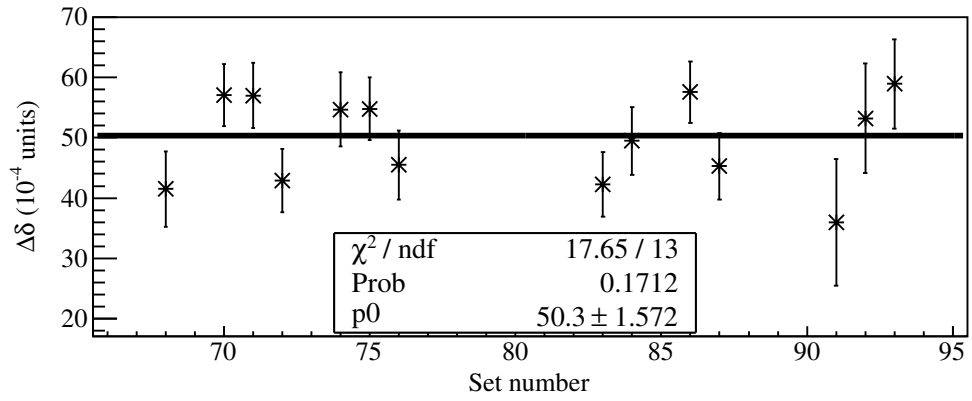
(b) Difference between data and MC for the analysis using the scale as the momentum calibration propagation model.

Figure 8.1: The difference $\Delta\delta$ is measured separately for the shift and the scale propagation model and the average of the two analyses is the result of the blind analysis.
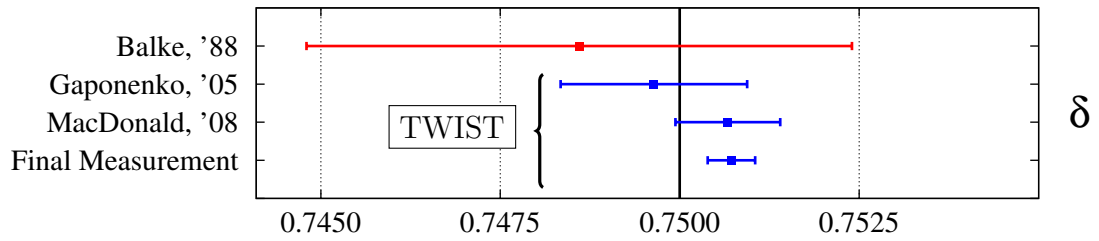
Figure 8.2: Comparison between the different measurements of the parameter δ. All the measurements are less than one standard deviation from one another.

Data set	MC input	Difference between MC input and blind analysis results	Measured $\Delta\delta$
74 (silver)	0.746542	0.00418	0.00454 ± 0.00061
74 (silver)	0.750665	-0.00005	0.00028 ± 0.00061
84 (aluminium)	0.750665	-0.00005	0.00027 ± 0.00056

Table 8.2: The data sets are fitted against a corresponding MC set generated using known decay parameters to verify that the measured $\Delta\delta$ do not depend on the MC input parameters. The results are consistent with the absence of bias.

8.1.2 Consistency test

The analysis procedure includes only one consistency test after the hidden parameter has been revealed. This test verifies that the results do not depend on the value of the hidden parameters. New MC sets were generated using random parameters and parameters equal to the blind analysis results. The measured values of δ are consistent with the input (Tab. 8.2). The test was performed on both targets.

8.1.3 $P_\mu\xi\delta/\rho$ inconsistency

The differential decay rate at the kinematic end point and in the direction opposite to the muon polarization can be written such that:

$$\frac{d^2\Gamma}{dx \, d\cos\theta} \propto \left(1 - \frac{P_\mu\xi\delta}{\rho}\right). \tag{8.4}$$

Since the differential decay rate is positive definite, the combination $\frac{P_\mu\xi\delta}{\rho}$ is necessarily smaller or equal to one.

The blind analysis presented here provides a simultaneous measurement of the parameters ρ, δ and $P_\mu\xi$ therefore it is possible to calculate the value of their combination. The result[1] from the blind analysis is:

$$\frac{P_\mu\xi\delta}{\rho} = 1.00192^{+0.00167}_{-0.00066} \tag{8.5}$$

This measurement is 2.9 standard deviations above the limit of one. This may indicate

---

[1]The asymmetric uncertainty comes from the asymmetric uncertainties from the measurement of $P_\mu\xi$ [31]. The correlations between the parameters are an important contribution to the uncertainty on $\frac{P_\mu\xi\delta}{\rho}$.

Coupling constants	pre-TWIST	Gagliardi[12]	Preliminary results	Improvement
$|g_{RR}^S|$	< 0.066	< 0.067	< 0.031	×2.1
$|g_{LR}^S|$	< 0.125	< 0.088	< 0.041	×3.0
$|g_{RR}^V|$	< 0.033	< 0.034	< 0.015	×2.2
$|g_{LR}^V|$	< 0.066	< 0.036	< 0.018	×3.7
$|g_{LR}^T|$	< 0.036	< 0.025	< 0.012	×3.0

Table 8.3: New global analysis results compared to the results prior to TWIST. The publish global analysis which used the initial TWIST results are also shown.

a problem in the blind analysis. At the time of writing this thesis, the problem has not been identified and this inconsistency is being investigated. The results and theoretical implications presented here correspond to the blind analysis. The central values or the systematic uncertainties of the final measurement of the decay parameters may change depending on the results of this investigation.

8.1.4 New global analysis

The global analysis described in Section 1.3.1 was performed using the newly measured decay parameters ρ, δ and $P_\mu\xi$. The results available are still *preliminary* at the time of writing this thesis. The new decay parameters provide constraints mostly on the right-handed muon decays and for this reason the other results of the global analysis are not presented here.

The parameters of the global analysis $Q_{\epsilon\mu}$ (Eq. (1.13)) represents the total probabilities for a μ-handed muon to decay into a ϵ-handed positron. Therefore the parameter Q_R^μ defined by:

$$Q_R^\mu = Q_{RR} + Q_{LR} \tag{8.6}$$

represents the probability for a right-handed muon to decay through any type of interaction. The global analysis provides a limit at a 90% confidence level of:

$$Q_R^\mu < 5.8 \times 10^{-4} \tag{8.7}$$

Limits on the individual coupling constants are also extracted from the analysis and compared to the results prior to TWIST in Tab. 8.3.

Besides the coupling constants, the global analysis provides new central values for the decay parameters. This is particularly interesting for the parameters such as η

which are difficult to measure at high precision. This new global analysis gives a new value of $\eta = -0.0033 \pm 0.0046$.

8.1.5 Limit on non-local tensor interactions

The relative strength of a potential non-local tensor interaction (Sec. 1.3.2) is evaluated using the relation:

$$\delta \approx \frac{3}{4}(1 - 6|g_{RR}^{T}|^{2}).\tag{8.8}$$

The coupling constant g_{RR}^{T} is defined only if $\delta \leq 0.75$. The measured value of δ in Eq. (8.3) is 2.2 standard deviations above 0.75 therefore the non-local tensor interaction is excluded with a confidence level of 97%.

8.2 η measurement

All the spectra from the blind analysis were refitted with the four decay parameters as fit parameters to measure η. The measured differences between data and MC are tabulated in Tab. 8.4. Again the results from the two analyses using the two propagation model for the momentum calibration are averaged to give the final difference of:

$$\Delta\eta = \left(-0.29 \pm 1.57(\text{stat.}) \pm 2.37(\text{syst.})\right) \times 10^{-2}\tag{8.9}$$

using the uncertainties evaluated in Sec. 7.4.

This result is not the experimental result because the MC was generated with the parameter η set at -0.0036 which is the value obtained from the global analysis using the previous TWIST measurement [17]. Therefore the experimental results of the measurement of η is:

$$\eta = 0.001 \pm 0.016(\text{stat.}) \pm 0.024(\text{syst.}).\tag{8.10}$$

This new measurement represents an improvement of a factor of 7.4 over the previous measurement on the momentum-angle spectrum by Derenzo [20] (Fig. 8.4). The improvement is only a factor of 1.3 compared to the best measurement from the transverse polarization of the decay positron by Danneberg *et al.* [22]. However since the two measurement techniques are very different, with their own systematic uncertainties, a potential bias in one technique is unlikely to exist in the other technique.

	$\Delta\eta$ ($\times 10^{-2}$) momentum calibration applied		Statistical uncertainties ($\times 10^{-2}$)
Data set	as a shift	as a scale	
68	5.06	6.67	6.25
70	9.37	11.42	5.15
71	1.79	3.03	5.42
72	-18.79	-17.22	5.29
74	-0.18	1.40	6.16
75	1.45	2.91	5.25
76	5.18	-3.33	5.75
83	0.67	1.72	5.38
84	-0.88	1.52	5.63
86	0.31	2.48	5.11
87	-5.35	-3.09	5.54
91	-4.66	-3.06	10.59
92	4.88	7.16	9.12
93	4.58	6.91	7.43
Weighted average	-0.30	1.14	1.58

Table 8.4: Difference between data and MC $\Delta\eta$ for each data set and for the weighted average. The statistical uncertainties correspond to the quadratic sum of the spectrum fit and the momentum calibration uncertainties (Tab. 7.8). Both analyses use the same data so their statistical uncertainties are the same.
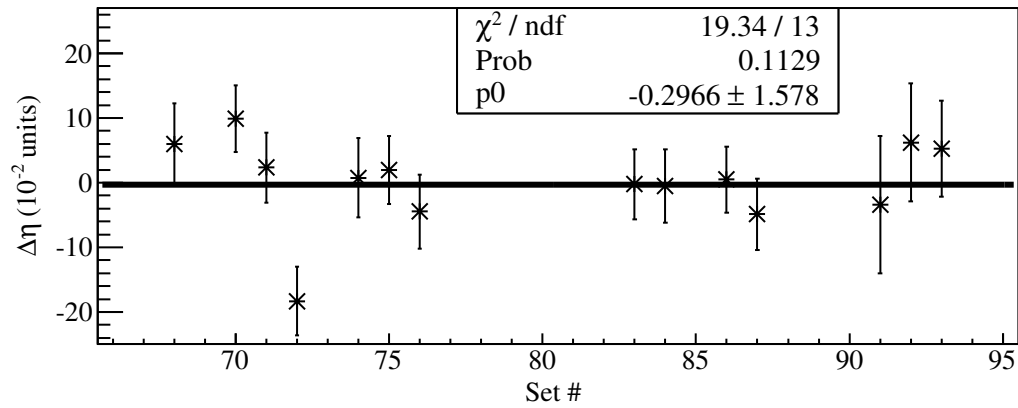
(a) Difference between data and MC for the analysis using the shift as the momentum calibration propagation model.
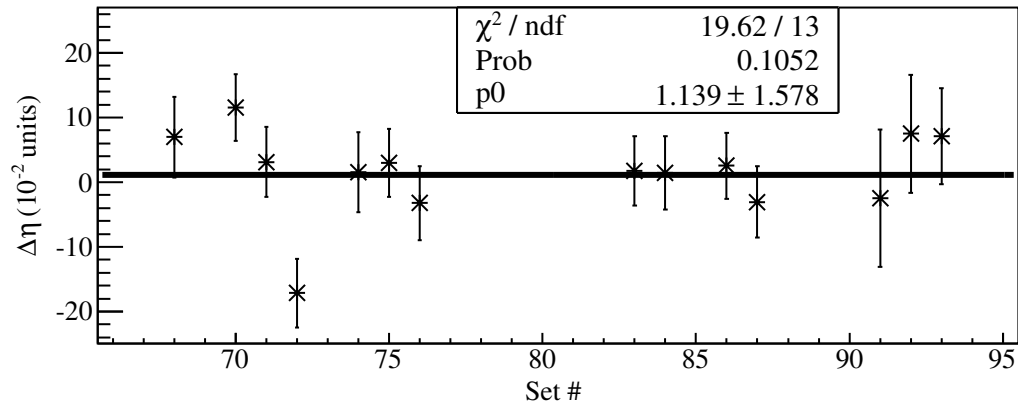
(b) Difference between data and MC for the analysis using the scale as the momentum calibration propagation model.

Figure 8.3: The difference $\Delta\eta$ is measured separately for the shift and the scale propagation model. The average of the two analyses is corrected by the value of η used to generate the MC to give the measured value.
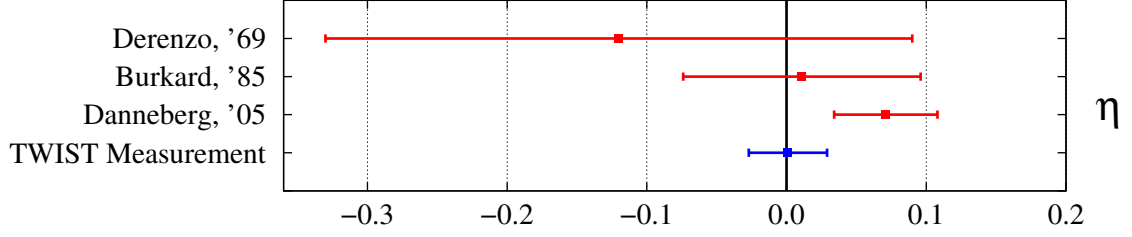
Figure 8.4: Comparison between of the different measurements of the parameter η. Besides the TWIST and Danneberg measurements which are separated by 1.5 standard deviation, all the measurements are less than one standard deviation from one another. TWIST and Derenzo measure positron momentum spectrum, while Burkard and Danneberg measure the positron's transverse polarization.

For this reason the two direct measurements are very complementary.

Our measured value of η is consistent with the Standard Model prediction of zero.

Similarly to the other three parameters, the final result of the measurement of η may be modified by the resolution of the $P_\mu \xi \delta / \rho$ inconsistency (Sec. 8.1.3).

Bibliography

[1] C.D. Anderson and S.H. Neddermeyer. Cloud Chamber Observations of Cosmic Rays at 4300 Meters Elevation and Near Sea-Level. *Phys. Rev.*, 50:263–271, 1936.

[2] S.F. Novaes. *Standard Model: An Introduction.* World Scientific, 2000. in *Particles and Fields, Proceedings of the X Jorge André Swieca Summer School,* arXiv:hep-ph/0001283v1.

[3] M. Bustamante, L. Cieri, and John Ellis. Beyond the Standard Model for Montaneros, 2009. arXiv:hep-ph/0911.4409v1.

[4] D. Griffiths. *Introduction to Elementary Particles.* Wiley, 1987.

[5] W. Fetscher, H.-J. Gerber, and K. F. Johnson. Muon decay: Complete determination of the interaction and comparison with the standard model. *Phys. Lett.*, B173:102, 1986.

[6] W. Fetscher and H.-J. Gerber. *Precision measurements in muon and tau decays.* World Scientific, 1995. in *Precision Tests of the Standard Electroweak Model.*

[7] A. Grossheim *et al.* Decay of negative muons bound in al^{2}7. *Phys. Rev. D,* 80:052012, 2009.

[8] L. Michel. Interaction between four half spin particles and the decay of the mu meson. *Proc. Phys. Soc.*, A63:514, 1950.

[9] Claude Bouchiat and Louis Michel. Theory of μ-meson decay with the hypothesis of nonconservation of parity. *Phys. Rev.*, 106(1):170–172, Apr 1957.

[10] Toichiro Kinoshita and Alberto Sirlin. Muon decay with parity nonconserving interactions and radiative corrections in the two-component theory. *Phys. Rev.*, 107(2):593–599, Jul 1957.

[11] Toichiro Kinoshita and Alberto Sirlin. Polarization of electrons in muon decay with general parity-nonconserving interactions. *Phys. Rev.*, 108(3):844–850, Nov 1957.

[12] C.A. Gagliardi, R.E. Tribble and N.J. Williams. Global analysis of muon decay measurements. *Phys. Rev. D*, 72(7):073002, Oct 2005.

[13] M.V. Chizhov. New tensor interactions in μ decay. *Mod. Phys. Lett.*, A(9):2979, 1994.

[14] M. V. Chizhov. Predictions for energy distribution and polarization of the positron from the polarized muon decay. *arXiv*, hep-ph/0405073, 2004.

[15] B. Balke *et al.* Precise measurement of the asymmetry parameter δ in muon decay. *Phys. Rev.*, D 37:587, 1988.

[16] A. Gaponenko *et al.* Measurement of the muon decay parameter δ. *Phys. Rev.*, D 71:071101(R), 2005.

[17] R. MacDonald *et al.* Precision measurement of the muon decay parameters rho and delta. *Phys. Rev. D*, 78:032010, 2008.

[18] D.B. Chitwood *et al.* Improved Measurement of the Positive-Muon Lifetime and Determination of the Fermi Constant. *Phys. Rev. Lett.*, 99:032001, 2007.

[19] A. Barczyk *et al.* Measurement of the Fermi constant by FAST. *Phys. Lett. B*, 663:172–180, 2008.

[20] S.E. Derenzo. Measurement of the Low-Energy End of the μ^+ Decay Spectrum. *Phys. Rev.*, 181:1854, 1969.

[21] H. Burkard *et al.* Muon Decay: Measurement of the Transverse Positron Polarization and General Analysis. *Phys. Lett.*, 160B:343, 1985.

[22] N. Danneberg *et al.* Muon Decay: Measurement of the Transverse Polarization of the Decay Positrons and its Implications for the Fermi Coupling Constant and the Time Reversal Invariance. *Phys. Rev. Lett.*, 94:021802, 2005.

[23] R.S. Henderson *et al.* Precision planar drift chambers and cradle for the TWIST muon decay spectrometer. *NIM A*, 548:306–335, 2005.

[24] J. Hu *et al.* Time expansion chamber system for characterization of TWIST low-energy muon beams. *NIM A*, 566:563–574, 2006.

[25] B. Jamieson. *Measurement of the Muon Decay Asymmetry Parameter with the TWIST Spectrometer.* PhD thesis, University of British Columbia, November 2005.

[26] R. Openshaw. TRIUMF, Vancouver, Canada. Private Communication.

[27] LeCroy 1877 fastbus TDC manual. *LeCroy Corporation.*

[28] LeCroy Corporation. *1877 Multihit Time-to-digital Converter: Specification.*

[29] R. Bayes. *A precision measurement of the muon decay parameter ρ.* PhD thesis, University of Victoria, 2010.

[30] Vector Fields Ltd. *OPERA-3d.*

[31] J. Bueno. *A direct measurement of $P_\mu\xi$ from muon decay.* PhD thesis, University of British Columbia, 2010.

[32] A. Gaponenko. *A precision measurement of the muon decay parameter δ.* PhD thesis, University of Alberta, 2005.

[33] A. Gaponenko. Technical note 88: Blind analysis in TWIST. Technical report, TWIST collaboration, TRIUMF, 2003.

[34] F. James. Fitting tracks in wire chambers using the Chebyshev norm instead of least squares. *Nuclear Instruments and Methods in Physics Research*, 221:145–152, 1982.

[35] G. Lutz. Optimum track fitting in the presence of multiple scattering. *NIM A*, 273:349–361, 1988.

[36] C. *et al.* (Particle Data Group) Amsler. The review of particle physics. *Phys. Lett.*, B667:1, 2008.

[37] R. MacDonald. *A precision measurement of the muon decay parameters ρ and δ.* PhD thesis, University of Alberta, 2008.

[38] R. Brun, F. Rademakers, S. Panacek, I. Antcheva, and D. Biskulic. *ROOT, Users guide.* CERN. http://root.cern.ch.

[39] F. James. MINUIT – Function Minimization and Error Analysis, CERN Program Library Entry D 506.

[40] R. Brun *et al. GEANT3 Users guide, CERN program library W5013.* CERN, 1994. Version 3.21/14 2002.

[41] V. Bargmann, L. Michel and V.L. Telegdi. Precession of the Polarization of Particles Moving in a Homogeneous Electromagnetic Field. *Phys. Rev. Lett.*, 2:435–436, 1959.

[42] A. B. Arbuzov. First-order radiative corrections to polarized muon decay spectrum. *Phys. Lett. B*, 524(1-2):99 – 106, 2002.

[43] A. Arbuzov, A. Czarnecki and A. Gaponenko. Muon decay spectrum: Leading logarithmic approximation. *Phys. Rev. D*, 65:113006, 2002.

[44] A. Arbuzov and K. Melnikov. $\mathcal{O}(\alpha^2 \ln(m_\mu/m_e))$ corrections to electron energy spectrum in muon decay. *Phys. Rev. D*, 66:093003, 2002.

[45] A. Arbuzov. Higher order QED corrections to muon decay spectrum. *J. High Energy Phys.*, 2003(03):063–063, 2003.

[46] A. Arbuzov. Virtual and soft pair corrections to polarized muon decay spectrum. *J. of Experimental and Theoretical Phys.*, 2003(78):179, 2003.

[47] R. Veenhof. *GARFIELD - simulation of gaseous detectors.* CERN.

[48] G. Marshall. OPERA map corrections from Hall and NMR maps at 2.0 T. Internal TWIST report, April 2009.

[49] W. Fraser. TRIUMF, Vancouver, Canada. Private Communication.

[50] V. Selivanov. Technical note 98: Direct Measurement of a Gap between Wire and Cathode Plane in DC4 Chambers. Technical report, TWIST collaboration, TRIUMF, 2005.

[51] K. Melnikov C. Anastasiou and F. Petriello. The electron energy spectrum in muon decay through $\mathcal{O}(\alpha^2)$. *J. High Energy Phys.*, (09):014, 2007.

Appendix A

Personal contributions

I joined the TWIST collaboration in September 2005. At this point the collaboration had already achieved a simultaneous measurement of ρ and δ on data taken in 2002 and a measurement of $P_\mu \xi$ on a different set of data from 2004. A graduate student was working at the time on a new measurement of ρ and δ from the 2004 data. Two graduate students and myself were assigned to the final measurement of the three decay parameters. I performed the subsidiary analysis of η after the analysis of δ was finished.

I participated in an engineering run between October and December 2005. Data was taken for physics results during three runs periods, from May to August 2006, from October to December 2006 and from May 2007 to August 2007. Beside taking shifts during these run periods, I was run coordinator between April and June 2006, and May and June 2007.

Prior to starting the analysis for the final measurement, the various softwares used for the previous measurements were reviewed. I reviewed in detail the code performing the event identification and classification (Sec. 3.2.3). I decided to write from scratch an event selection software called Clark (Chapter 4) to replace the previous software. I studied and tuned the pulse width and the pair matching cuts.

I also developed and prepared some of the calibrations (Chapter 6 and appendices C and D) required for the final analysis:

- DC-TEC alignment

- DC-Yoke alignment

- DC-BField alignment

123

- DC relative alignment

I improved the TEC calibration and the cathode foil bulge measurement which were originally developed by a former PostDoc, Jingliang Hu.

The MOFIA analysis and MC generation were performed on the WestGrid cluster. I have been in charge of the maintenance of the scripts managing the submissions and the data files since October 2007. I was also coordinator of the analyses and MC generations on the Glacier cluster between October 2007 and November 2008 and on the Orcinus cluster since May 2009. Since we were the first users on the Orcinus cluster, I had to adapt our scripts to this new cluster. I participated in the early tests and validations of our final analysis. I prepared and submitted the analysis of most of the data sets, and the second round of statistics of the MC generation. I finalized and validated all the systematic uncertainties common to the three parameters (Chapter 7).

Beside the work of research, I was also the administrator of the 15 cluster machines and 10 desktop computers of the TWIST collaboration at TRIUMF since October 2006. I migrated the TWIST website to a mediawiki website (à la Wikipedia) that I maintained over the years.

Appendix B

Classification types

B.1   Window types

1. Muon

2. Upstream decay positron

3. Downstream decay positron

4. Beam positron

5. Empty window

6. Overlap involved

7. Upstream decay positron with a δ ray emitted downstream.

8. Downstream decay positron with a δ ray emitted upstream.

9. Upstream decay positron that scattered back into the spectrometer.

10. Downstream decay positron that scattered back into the spectrometer.

11. Muon decaying within 100 ns downstream.

12. Muon decaying within 100 ns upstream.

13. Muon and beam positron overlapping within 100 ns

14. Upstream decay positron and beam positron overlapping within 100 ns

15. Downstream decay positron and beam positron overlapping within 100 ns

16. Soft uncorrelated track

17. Cosmic, noise, or beam gas

18. Track appearing too early in the event, 5800 ns before the trigger time.

19. Track appearing too late in the event, 9800 ns after the trigger time.

20. Unidentified

B.2   Event types

1. (Simple clean) One muon and one decay positron not overlapping in time.

2. (Time clean) One muon, one decay positron and one or more beam positrons not overlapping in time.

3. (Simple DC overlap) One muon and one decay positron separated by more than 100 ns but less than 1000 ns.

4. (Time DC overlap) Same as event type 2 with one ore more windows separated by more than 100 ns but less than 1000 ns.

5. (Simple δ ray) One muon and one decay positron with a δ ray emitted in the other half of the spectrometer (window type 7 or 8).

6. (Time δ) One muon, one decay positron with a δ ray emitted in the other half of the spectrometer (window type 7 or 8) and one beam positron.

7. (Simple δ ray DC overlap) Same as event type 5 with one ore more windows separated by more than 100 ns but less than 1000 ns.

8. (Time DC overlap δ ray) Same as event type 6 with one ore more windows separated by more than 100 ns but less than 1000 ns.

9. (Simple backscatter) One muon and one decay positron scattering back in the spectrometer (window types 9 or 10).

10. (Time backscatter) One muon, one decay positron scattering back in the spectrometer (window types 9 or 10) and one beam positron.

11. (Simple backscatter DC overlap) Same as event type 9 with one ore more windows separated by more than 100 ns but less than 1000 ns.

12. (Time backscatter DC overlap) Same as event type 10 with one ore more windows separated by more than 100 ns but less than 1000 ns.

13. (Beam positron trigger) Event triggered by a beam positron.

14. (Multiple muon decays simple clean) More than one muon each with a corresponding decay positron.

15. (Multiple muon decays time clean) More than one muon each with a corresponding decay positron and one or more beam positrons.

16. (Multiple muon decays simple clean DC overlap) Same as event type 14 with one ore more windows separated by more than 100 ns but less than 1000 ns.

17. (Multiple muon decays time clean DC overlap) Same as event type 15 with one ore more windows separated by more than 100 ns but less than 1000 ns.

18. (Multiple muon decays dirty) More than one muon with some decay positrons not associated with any muon.

19. (Muon(s) and beam positron(s)) One or more muons and one or more beam positrons. No decay positrons.

20. (Simple beam positron) One muon and one decay positron overlapping within 100 ns of a beam positron (window type 14 or 15).

21. (Time beam positron) One muon, one decay positron overlapping within 100 ns of a beam positron (window type 14 or 15) and one or more beam positrons.

22. (Simple beam positron DC overlap) Same as event type 20 with one ore more windows separated by more than 100 ns but less than 1000 ns.

23. (Time beam positron DC overlap) Same as event type 21 with one ore more windows separated by more than 100 ns but less than 1000 ns.

24. (Beam positrons, unknown trigger) The event contains one or more beam positrons but no trigger window.

25. (Unknown trigger) Unidentified trigger window.

26. (Unknown) The topology of the event do not correspond to any other event type.

27. (Simple clean with too few plane hit) Same as the event types 1, 6, 10, and 21 but with less than five hit clusters in the decay positron window.

28. (Time clean with too few planes hit) Same as the event types 2, 7, 11, and 22 but with less than five hit clusters in the decay positron window.

29. (Simple clean with too high angle decay positron) Same as the event types 1, 6, 10, and 21 but with too many hits or hit clusters in the decay positron window.

30. (Time clean with too high angle decay positron) Same as the event types 2, 7, 11, and 22 but with too many hits or hit clusters in the decay positron window.

Appendix C

Time Expansion Chamber (TEC) calibration

The TEC characterization of the muon beam is a critical aspect of the final TWIST measurement of the $P_\mu\xi$ parameter. Four separate calibrations are used to convert the hit TDC times measured in the TEC into drift distances from the sense wires (Fig. C.1). The four calibrations are determined separately in a well defined sequence.

The calibration procedure and precision have been improved significantly from the results reported in [24].

C.1   Calibration data

The calibration of the TEC requires data taken under special running conditions. Two collimators (Fig. C.2(a)) are installed on the TEC gas box (see Sec. 2.1.5). These collimators define straight tracks with a precise position relative to the gas box. Therefore the calibration of the TEC modules is relative to the TEC gas box which is aligned in the TWIST coordinate system as described in section D.

The collimators contain 121 holes, which is an improvement compared to the 49 holes of the collimators used in [24]. The new collimators almost entirely cover the active volume of the TEC, and provide more points for the STR calibration. The M13 beamline was tuned to provide a widely spread beam of muons at 29.6 MeV/c, illuminating almost all the holes of the collimators (Fig. C.2(b)).

Calibration runs were taken for almost every sense wire plane used for the final analysis (see Tab. C.1). Unfortunately no calibration runs were taken for the sense
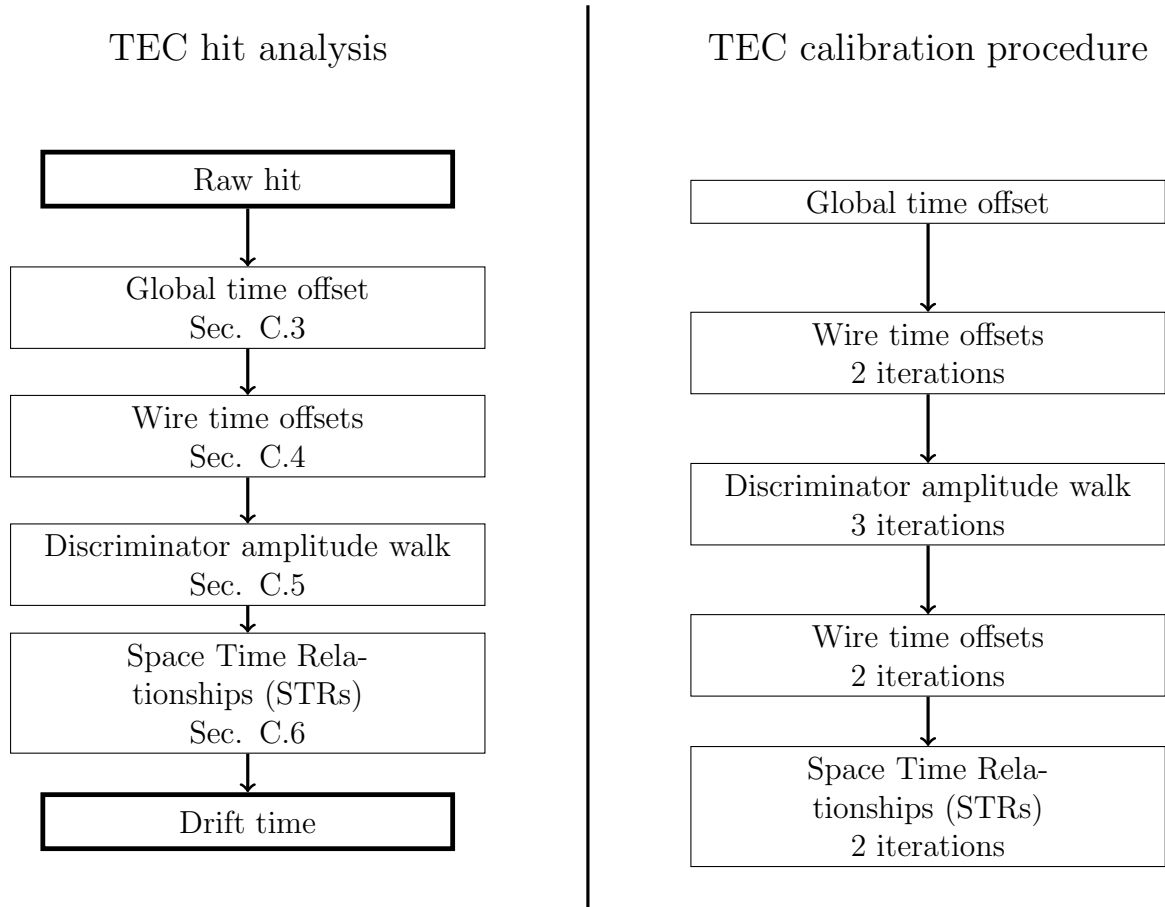
TEC hit analysis

TEC calibration procedure

TEC hit analysis
Raw hit
↓
Global time offset Sec. C.3
↓
Wire time offsets Sec. C.4
↓
Discriminator amplitude walk Sec. C.5
↓
Space Time Rela- tionships (STRs) Sec. C.6
↓
Drift time

| TEC calibration procedure |
|---|
| Global time offset |
| ↓ |
| Wire time offsets
2 iterations |
| ↓ |
| Discriminator amplitude walk
3 iterations |
| ↓ |
| Wire time offsets
2 iterations |
| ↓ |
| Space Time Rela-
tionships (STRs)
2 iterations |

Figure C.1: Four calibrations are applied to a raw hit before obtaining the drift time (on the right). The TEC calibration procedure measures the four calibrations. Most calibrations require few iterations due to the interplay between the track reconstruction and the calibrations. The discriminator amplitude walk correction affects the wire time offsets. For this reason the wire time offsets are calibrated before and after the discriminator amplitude walk correction is measured.
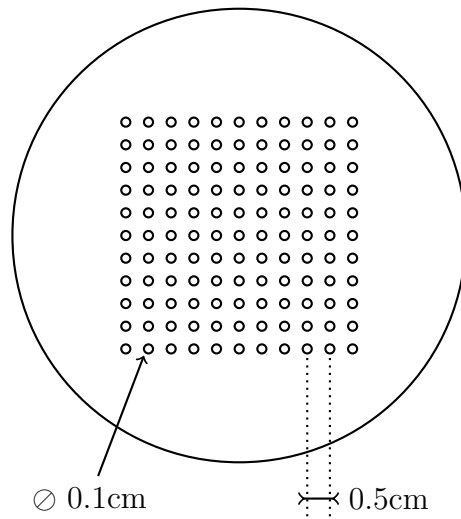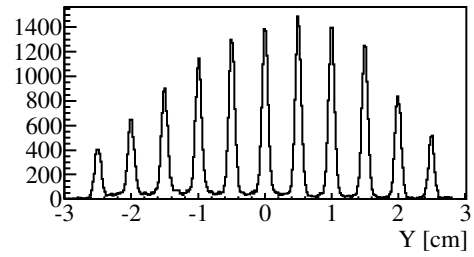
(a) Diagram not to scale.
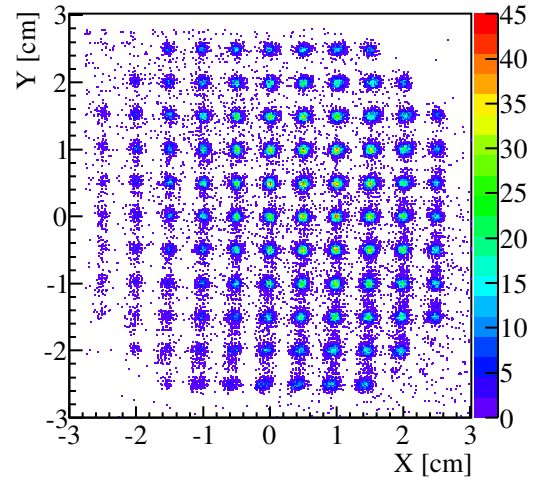
(b)
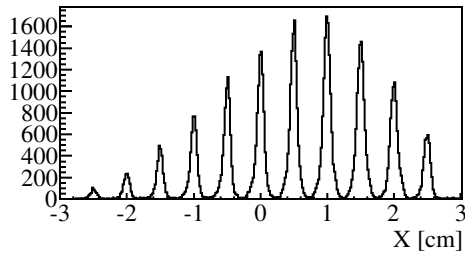
(c)

(d)

Figure C.2: Diagram of the collimators installed on the TEC gas box in (a). The corresponding profile measured by the TEC is (b). Only the projections on x or y in (c) and (d) are measured by the wires.

wire planes used in October and November 2006. The muon beam characterizations measured by these planes will have a higher systematic uncertainty due to the lack of calibration.

Calibration data	Date	Average temperature [°C]
2006Aa	June 2006	26.0
2006Ab	June 2006	27.2
2006B	December 2006	22.4
2007A	May 2007	26.4
2007B	July 2007	27.9
2007C	July 2007	28.1

Table C.1: TEC calibration data collected. The calibration runs 2006Aa and 2006Ab were taken with the same sense wire planes respectively without and with the solenoid magnet energized.

Each wire in the TEC measures the projection in x or y. The wires are calibrated separately and therefore during the calibration only the projection of the 121 holes onto eleven drift distances are available (Fig. C.2(c) and C.2(d)).

C.2 Characterization analysis

The calibrations require straight tracks going through corresponding holes of the upstream and downstream collimators. Cuts on the position and the angle of the tracks select the required tracks. The measured position and angle of the tracks are modified by each step of the calibration procedure. For these reasons the beam profile is analysed before each iteration of each calibration to define the cuts on the position and the angle selecting the straight tracks going through corresponding holes.

C.3 Global time offset

The TDC times from the TEC need to be compared with the M counter of the spectrometer in order to be converted into drift times. The global time offset calibrates the whole TEC. The time offset for each wire is refined in the rest of the calibration procedure.

The global time offset is set in order to get a measured position around zero in x and y for the tracks going through the central hole. This calibration is only providing

a global calibration of the time offset. The calibration of the individual wire time offsets and more importantly the STRs make the final adjustments.

C.4   Wire time offsets

The wire time offsets for the TEC sense wires are derived in a similar way to the wire time offsets in the DCs and PCs. The calibration method uses the time information of hits from the straight tracks going through the central holes of the collimators which are therefore at a constant distance from the sense wires. Since all the hits are in average from the same drift distance, the mean drift times from all the wires must be the same.

For each wire the TDC time of the hits from the tracks going through the central hole of both collimators are plotted (Fig. C.3). A Gaussian fit finds the mean of the peak for each wire. The average drift time is then calculated for the 48 wires. The x and y modules are calibrated simultaneously since the global time offset is set for the whole TEC.
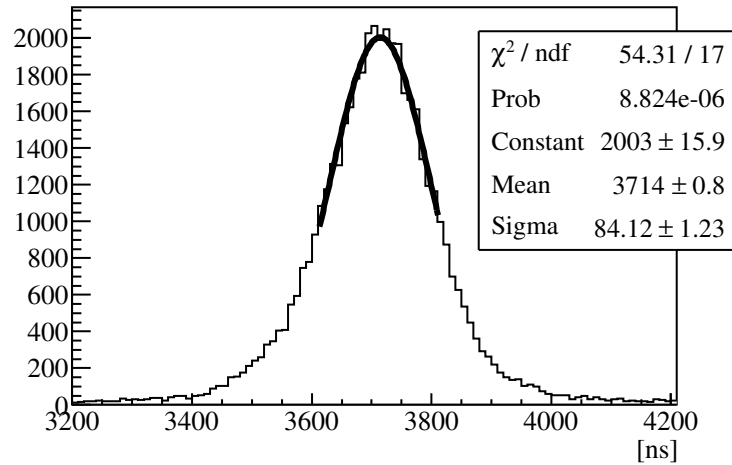

Figure C.3: The drift time of the hits from the tracks going through the central holes is plotted. A Gaussian fit is used to find the mean used to correct the wire time zero offset.

Fig. C.4 shows the dependence of the time offset versus the sense wire number. The relative time offset calibration is done using the fixed distance of selected tracks therefore the geometry of the TEC is an important element of the measurement. The slope of the time offset in one module can be explained by an angle between the TEC
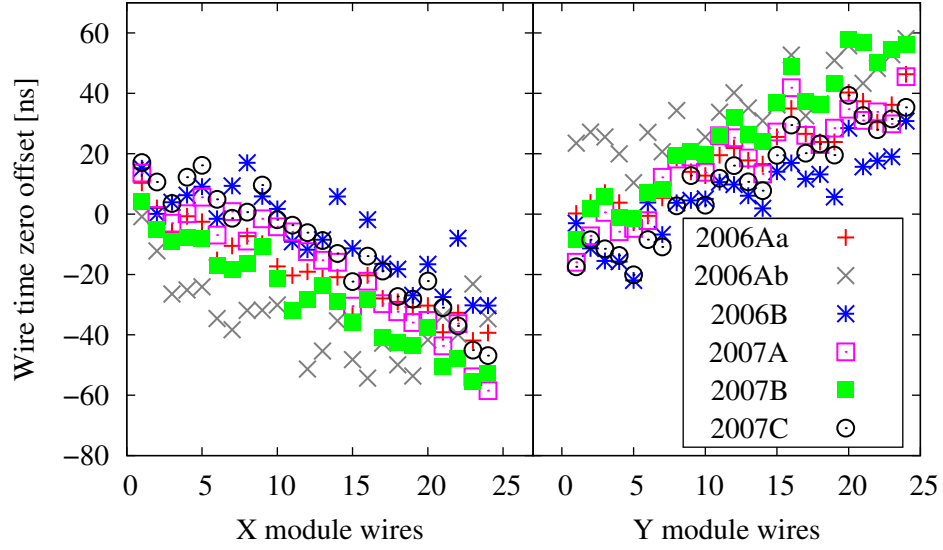
Figure C.4: The main source of the vertical shift of the time offsets is mostly due to the temperature of the DME gas. The difference in slopes is due to different positions of the different sense wire planes from their nominal values.

module and the TEC gas box in which the collimators are installed. The wire time offset calibration is fairly stable for different sense wire planes. The main source of variation is the relative position of the sense wire planes and the collimators. Their absolute position is not perfectly reproducible in repeated installations. The position is reproducible within 500μm.

The calibration improves the tracking, which in return improves the reconstruction of the tracks used for the calibration. For this reason the wire time offsets calibration was iterated twice.

C.5   Discriminator amplitude walk

The rising edge of a hit signal is more or less steep depending on the amplitude of the signal. The Fig. C.5 shows how this affects the time at which the signal reaches the threshold of the TDC. The discriminator amplitude walk calibration corrects for this effect in the TEC.

The amplitude walk calibration uses the same tracks from the central holes of the collimators and therefore the same cuts as the wire time offsets calibration. The time of the hits is plotted versus the TDC width corresponding to their time-over-threshold
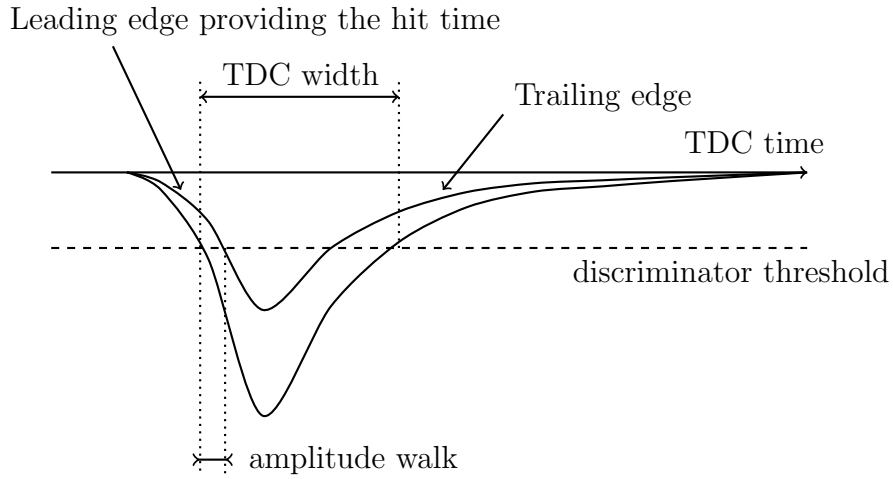
(Fig. C.6).

Figure C.5: Typical TDC signal shape and the effect of the discriminator amplitude walk on the hit starting time. Two hits with different amplitudes do not cross the discriminator threshold at the same time. The resulting walk is biasing the time measurement of the hit from the leading edge.
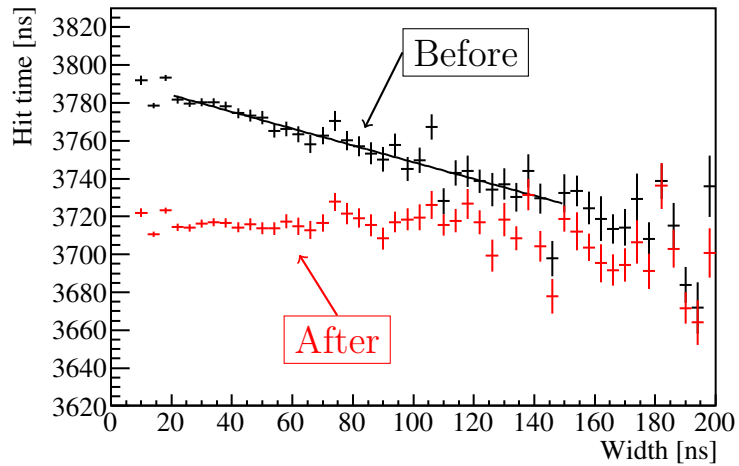

Figure C.6: The drift time versus the TDC width before the discriminator amplitude walk correction (in black) is fitted with a straight line. There is no significant correlation between the TDC time and the TDC width after the correction (in red).

A linear fit is performed on the restricted range of the TDC width because the correlation between the width and the time of the signal is only valid for a certain
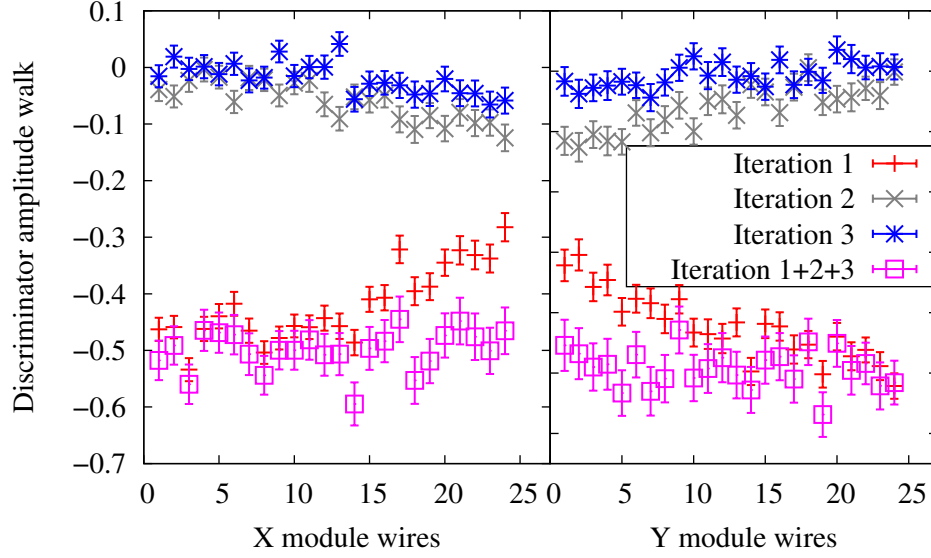
Figure C.7: Three iterations are necessary to get a convergence of the amplitude walk correction. There is no significant correlation between the correction and the sense wire position in the module.

range of TDC width. For very small widths the electronic noise is too significant. The slope of the rising edge reaches a limit above a certain width and the starting time of the signal is not affected anymore. To take this into account the discriminator amplitude walk correction is applied only on a restricted range of the TDC width:

$$T_{corrected} = \begin{cases} T + A * (120 - 20) & \text{if } W < 20ns \\ T + A * (120 - W) & \text{if } 20ns < W < 120ns \\ T + A * 0.0 & \text{if } W < 20ns \end{cases}$$

The amplitude walk calibration requires three iterations to converge (see Fig. C.7). The corrections for all the calibration runs converge to the same value of -0.5. As expected the discriminator amplitude walk is independent of the wire and the sense wire plane.

C.6 TEC Space Time Relationships (STRs)

The Space Time Relationship of each wire is the most important calibration. The collimators shown in Fig. C.2(a) proved to be the ideal design to extract the required

high precision STR calibration. The following procedure is applied to each wire.

The first step of the calibration is to select the tracks going through the eleven drift distances. A figure of merit is calculated for each drift distance:

$$M_h = \frac{(x - x_h)^2}{\sigma_x^2} + \frac{A_x - A_{x0}}{\sigma_A^2}$$

with the index h going from 1 to 11; x and A are the position and the angle of the track; x_h the drift distance; A_{x0} the measured mean angle of the beam; σ_x and σ_A the uncertainties of the position and the angle.

If the value of the figure of merit of one of the drift distances is less than one, the track is selected as going through corresponding collimator holes. Its hit drift times are added to a one dimension histogram (Fig. C.8(a)). Eleven independent Gaussian fits extract the mean drift times for the eleven drift distances.

A plot of the drift distances versus the corresponding drift times is fitted with a third order polynomial (Fig. C.8(b)). This function is the space time relation used in the reconstruction algorithm in MOFIA to convert a drift time into a drift distance. The residuals are less than 50 μm on both modules.

The TEC STRs are sensitive to the density of the DME gas. The pressure is precisely regulated at 80 mbar therefore only the temperature has to be taken into account. Drift time correction factors were calculated using a Garfield [47] simulation of the TEC at different temperatures. The drift time depends linearly on the temperature at a given distance from the sense wire plane(Fig. C.9). The slope of this linear dependence varies quadratically with the distance to the wire.

The temperature correction is applied to the mean drift times from the Gaussian fits of the eleven peaks on Fig. C.8(a). Therefore the correction is applied before the third order polynomial fit. This temperature correction was validated by using the calibration data 2006B and 2007C, which were taken at temperatures different by almost 6°C. The 2007C calibration data was analysed with the calibration from 2006B with and without temperature correction (Fig. C.10(a) and C.10(b)).

Although the temperature correction corrects for most of the difference between 2006B and 2007C, there are some remaining discrepancies that can be explained by the shape of the muon beam. The discrepancies are larger in x and the beam in this direction is very different for 2006B and 2007C (Fig. C.10(c)). The position as well as the angle of the beam determine the illumination of the holes and the occupancy of the various drift distances especially the short and long ones. A drift distance with
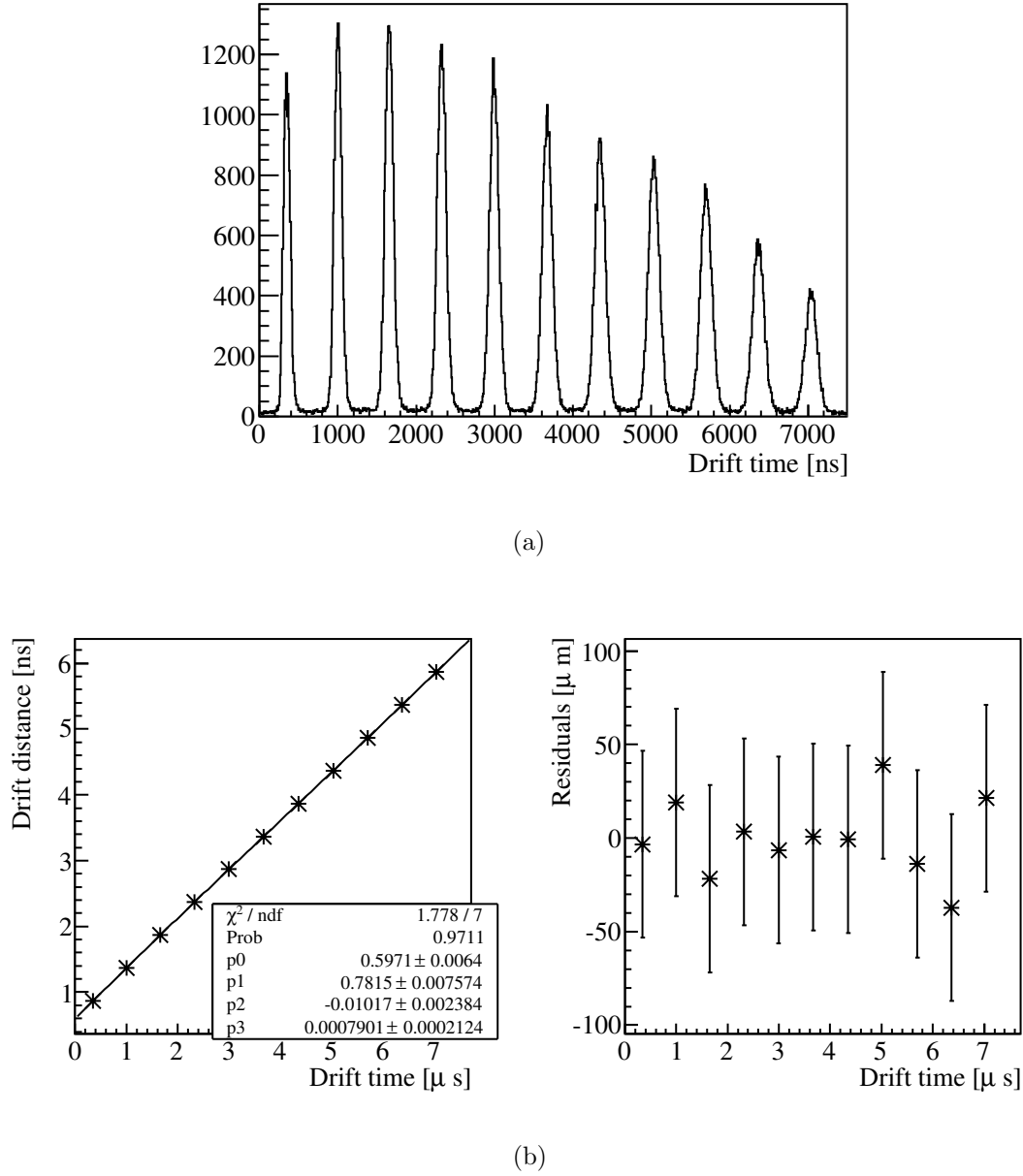
(a)

(b)

Figure C.8: The eleven drift time peaks are fitted independently in (a) with a Gaussian distribution to obtain the mean. The plot (b) of the drift distance versus the drift time is fitted with a third order polynomial which represents the space time relation for this wire. The error bars on the residuals are the uncertainties on the hole positions on the collimators.
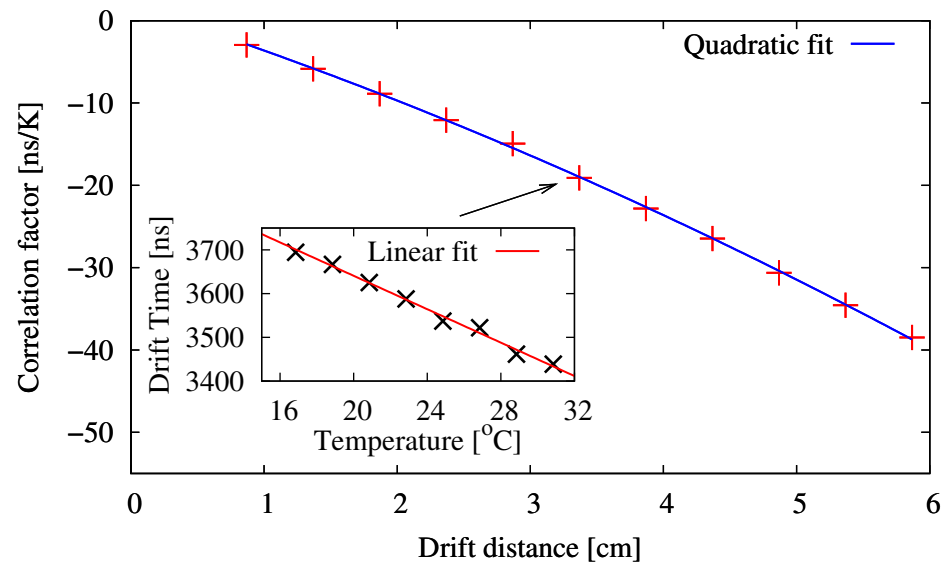
Figure C.9: The drift time depends linearly on the temperature and this linear dependence is a function of the drift distance.
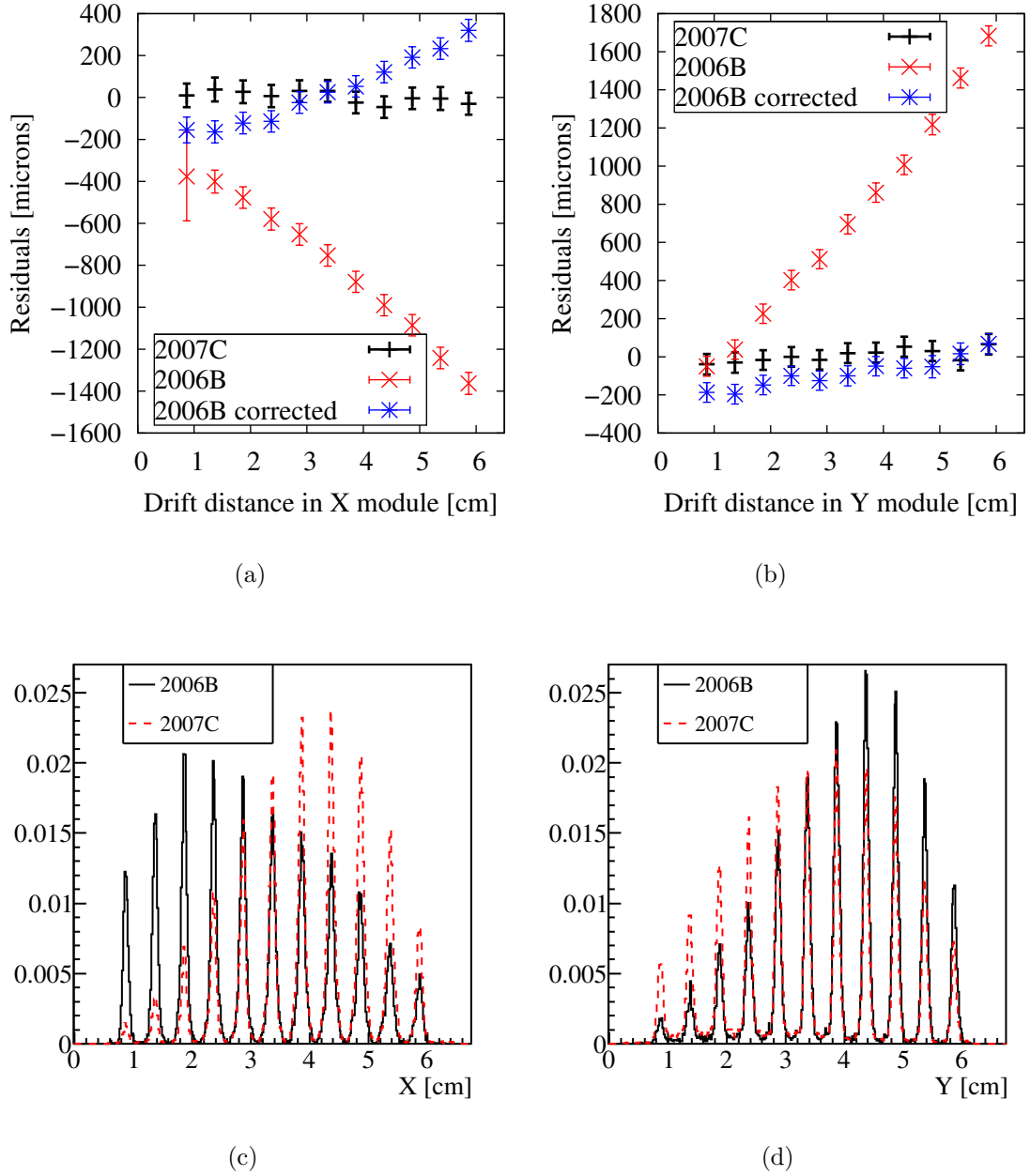
(a)

(b)

(c)

(d)

Figure C.10: The residuals on the plots (a) and (b) are the difference between the measured position of the holes and their actual position on the collimators. The temperature correction is clearly reducing the differences between the calibrations. The remaining difference between the calibrations is from the different beams used for the calibration runs (Fig. (c) and (d)). The effect of the temperature on the drift distances in the opposite in the x and y modules because the sense wires are installed in the x module at x=-3cm and in the y module at y=+3cm.

a low occupancy is biased by up to 500 μm which corresponds to the radius of the holes in the collimators.

C.7   TEC calibration precision

The discriminator amplitude walk calibrations are consistently at -0.5 within statistical errors for all the sense wire planes. Studies on the track reconstruction in the TEC showed that the discriminator amplitude walk as a negligible effect on the muon beam profiles [31]. Therefore there is no uncertainty from this calibration.

The wire time offset corrections are just a first guess. The offset is calibrated much more precisely by the lowest order coefficient of the STR calibration.

The STR calibration is the only source of systematic uncertainty for the TEC calibration. The residuals from the polynomial fit extracting the STRs are less than 50 ns and therefore negligible (Fig. C.8(b)).

A possible source of uncertainty is the temperature correction. The corrections applied are less than 2°C and the table C.2 shows little change in the position measurement despite a correction of 5°C. For this reason the temperature correction is not a significant source of uncertainty. The position uncertainty is better than 100 μm and the corresponding angle uncertainty is 2 mrad. The main uncertainty comes from the effects of the position of the beam on the STR calibration. This affects all the calibrations and all the TEC beam profiles. A systematic uncertainty can be derived from the comparison between 2006B and 2007C calibrations because of the difference in their muon beams (Fig. C.10(c)). The change is not visible in the mean position in x (table C.2) because the center of the TEC where the beam for nominal data is located, is barely affected by the change in calibration beam (Fig C.10(a). However a conservative uncertainty of 200 μm is used for the TEC position uncertainty and 4 mrad for the angle uncertainty.

Calibration data	2007C	2006B	2006B corrected
Mean x [cm]	0.186	0.101	0.182
RMS x [cm]	0.433	0.426	0.439
Mean y [cm]	0.431	0.504	0.440
RMS y [cm]	0.567	0.547	0.562
Mean dx [mrad]	-0.89	-1.98	-2.08
RMS dx [mrad]	13.98	13.80	14.18
Mean dy [mrad]	-2.56	-5.57	-5.73
RMS dy [mrad]	20.96	20.24	20.79

Table C.2: A profile taken with the 2007C planes is analyzed with its corresponding calibration and with the 2006C calibration with and without the 5 $°C$ temperature correction. The temperature correction changes the position by almost a milimiter and barely changes the angle. The change in angle between the 2007C and 2006B calibrations is due to the difference in position of the sense wire planes.

Appendix D

Relative alignments of the apparatus components

All the different elements of the TWIST experiment cannot be aligned simultaneously. Instead a series of relative alignment procedures are performed. The relative alignment of the wire chambers is performed first since its results are used for the other alignment procedures. The stack of the chambers is then aligned to the rest of the experimental setup.

The relative alignment of the wire chambers is fundamental for the reconstruction of the particle tracks in the spectrometer which are used for the other alignment procedures. Once their relative misalignment is corrected, the individual chambers are not considered independently but instead the spectrometer as a whole is aligned to the rest of the experimental setup.

Each procedure aligns two elements of the experimental setup relative to each other. The TEC is aligned during its installation to the yoke by using a theodolite at the beginning of each run period. The spectrometer is aligned to the yoke using collimated straight tracks. Finally the magnetic field map is aligned to the spectrometer by fitting decay positron tracks with helices including two extra degrees of freedom for the helix axis direction. Indirectly the magnetic field map, the spectrometer and the TEC are aligned to each other.

An alignment procedure using straight tracks reconstructed in both the TEC and the spectrometer was developed to align these two elements to each other. This procedure would have eventually improved or at least validated the theodolite alignment of the TEC to the yoke. However the position of the TEC was not constant between

the beginning and the end of the data sets when the TEC was installed to measure the muon beam [31]. Due to this instability the alignment procedure was not carried out for this analysis.

D.1   Wire chambers relative alignment

The position of the wires within each wire chamber plane is known to less than 10 μm from mechanical measurements during the production of the wire chambers and the position in z of the whole chamber is known to a few microns [23]. The alignment of each wire is therefore sufficient and only the misalignment in u and v of the whole chamber is measured.

The position of the chambers was measured using a wide-spread beam of 120 MeV/c pions with the solenoid turned off. In this configuration the pions travel in straight lines through the whole detector. The relative alignment of the drift chambers is achieved by reducing the space residuals of the reconstructed straight tracks at each plane.

The straight tracks are reconstructed using the same helix fitter algorithm used to reconstrcut the helices from the decay positrons in the standard data. However in the case of data with zero magnetic field, the helix fitter actually fits straight lines to the hits. This straight track mode is very efficient because it includes kinks at 16 points in the detector and at the target as fit parameters to take into account the multiple scattering.

The position of the chamber along the direction of its wires cannot be calibrated and is not important. The rotation of the plane can be extracted from the dependence of the residuals with respect to the v (u) direction for a u (v) plane (Fig. D.1).

D.1.1   Drift chambers relative alignment

The DC alignment procedure is an iterative process. During an iteration and for each plane five histograms of the residuals are filled (Fig. D.1). At the end of an iteration, the mean value of the histograms is used to compute the misalignment in translation and rotation of the plane. The measured misalignment is directly implemented as a correction to the detector geometry in the reconstruction software. The residual histograms are emptied before the beginning of the next iteration. Although the same data can be used up to three times in an alignment procedure, it is never used in

two consecutive iterations. The number of tracks per iteration increases during the alignment procedure to increase the precision as it is getting closer to convergence.
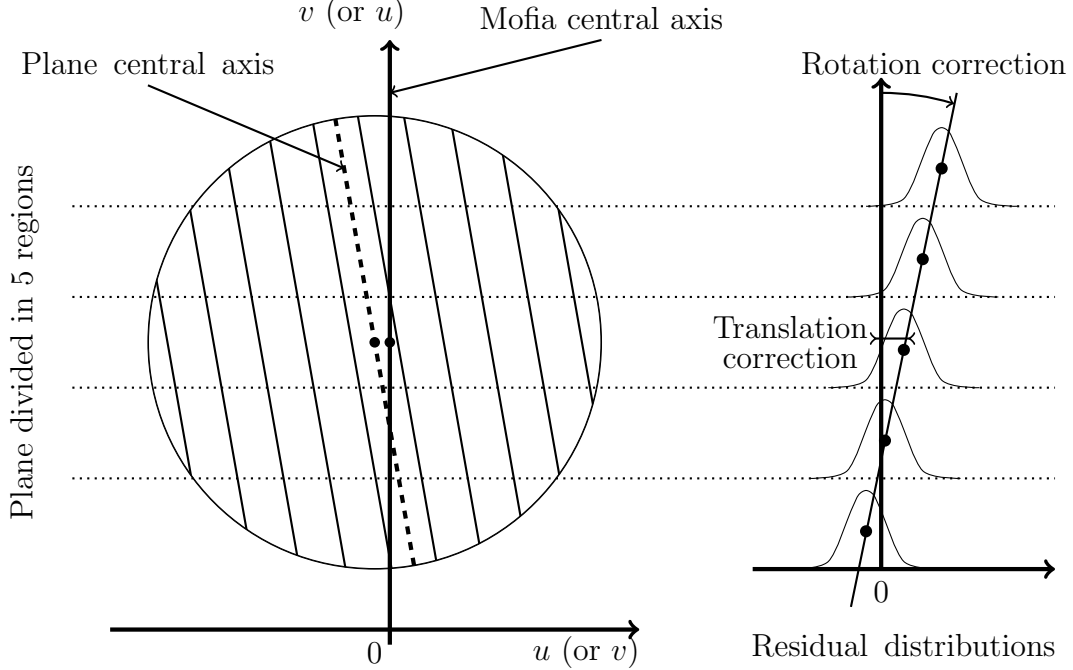

Figure D.1: The translation and rotation misalignment measurement. The residuals are histogramed separately for each sector of the plane. The actual sectors are larger at the top and the bottom of the plane in order to compensate for the lower occupancy.

D.1.2 Target kink corrections

The 16 kinks are located in the drift planes and constrained by the straight line fit (Sec. 3.2.5). The kink at the target on the other hand is a free parameter. It is also independent of the residuals by used for the alignment procedure of the DCs. For this reason a linear dependence of the misalignment can appear with an average kink at the target different from zero (Fig. D.2). This linear dependence corresponds to a constant shear of opposite direction upstream and downstream for the translation correction. The effect on the rotation correction can be described as a "cork screw" effect and more precisely two cork screws of opposite direction upstream and downstream. The cork screw effect on the v (u) planes is due to a linear dependence of the kink at the target with respect to the u (v) coordinate, similar to the linear dependence of the residuals Fig. D.1.
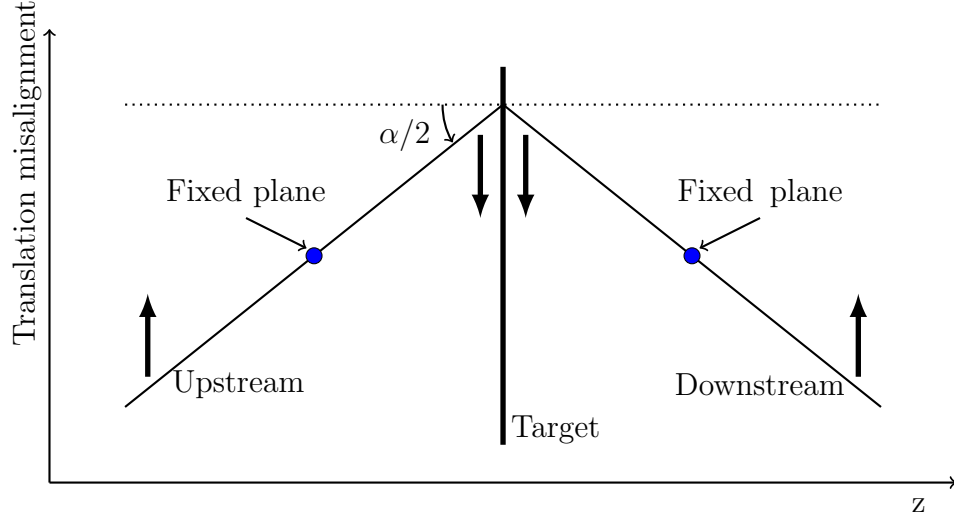
Figure D.2: The kink at the target creates a dependency of the translation misalignment measured with respect to z. The correction of this effect uses the mean of the kink at the target α at each iteration. The fixed planes (planes 14 and 31) are used as anchor points for this correction.

The misalignment created by the non-zero average kink at the target cannot be eliminated by the basic alignment procedure. The kink at the target is known for each track. The average is calculated and used to apply a correction at the end of each iteration of the alignment procedure. Two planes are used as anchors. The target kink correction for the translation is simply using the linear dependence in z (Fig. D.2). For the rotation the target kink correction R for an upstream u plane at a position z is given by:

$$R = \arctan\left(\frac{\tan\left(\frac{v \times a_U}{2}\right) \times (z - z_{14})}{v}\right) \simeq \frac{a_U}{2} \times (z - z_{14}) \qquad \text{(D.1)}$$

with a_u the average target kink angle and z_{14} the z position of the anchor plane 14.
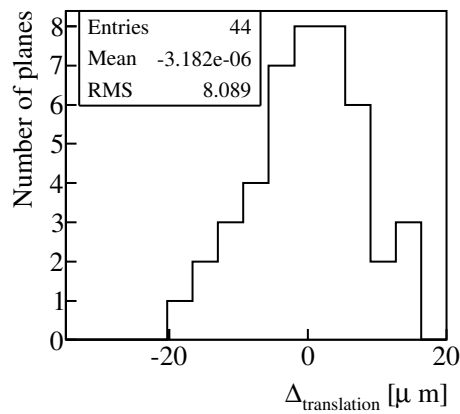
D.1.3 Precision of the DC alignment procedure

The alignment algorithm was developed and tested on a MC by comparing the input misalignment and the misalignment measured. The difference between the input and the output after convergence is also used to determine the precision of the alignment procedure.
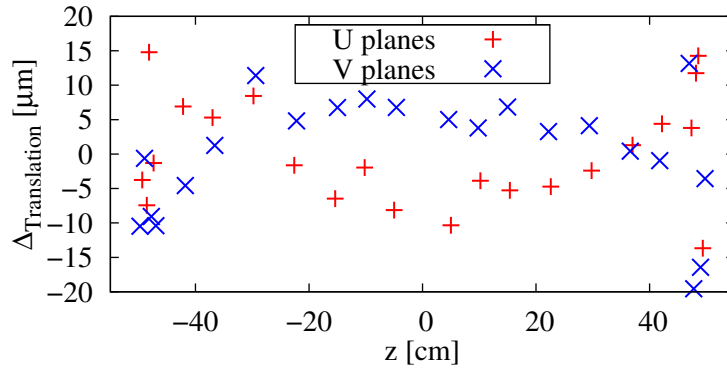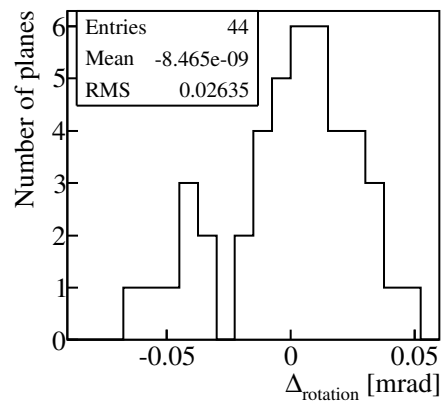
(a)
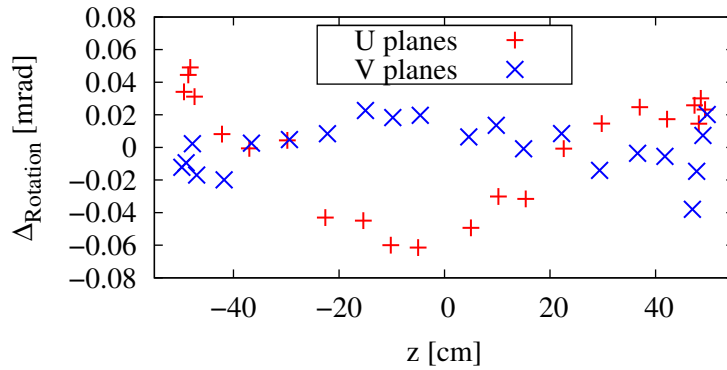
(b)

(c)   (d)

Figure D.3: Difference between the input and measured misalignments after convergence of a MC for the translation ($\Delta_{translation}$) and the rotation ($\Delta_{rotation}$). The precision of the alignment procedure is extracted from (c) and (d).

The precision of the alignment is 10 μm for the translation and 0.03 mrad for the rotation (Fig. D.3) including the z dependence remaining after the target kink correction. The alignment of the DCs was done for each run period because the target was changed between each run period. When the target is changed, the wire chamber stack is opened and the misalignment of the chambers can change. The DC misalignment can typically reach 1 mm in translation and 4 mrad in rotation.

D.1.4 Proportional chambers relative alignment

Unlike the DC alignment, the PC alignment procedure is not iterative because the PCs are not used in the track reconstruction. In addition the PC alignment is not of very high precision since there is no usable drift time. The DCs are aligned first in order to improve the track reconstruction. The position of the tracks are extrapolated to the PCs and compared with the position of the wires which recorded a hit. The residual distributions produced are used in the exact same way that the DC residual distributions in the case of the DC alignment (see Fig. D.1).

D.2 Relative alignment of the spectrometer and the yoke

The relative position of the spectrometer and the yoke is not directly important for the decay parameters. However aligning the spectrometer to the yoke means also that the spectrometer is aligned indirectly to the TEC. The muon beam is measured precisely in the TEC and this characterization of the beam is used to generate the simulated beam. Therefore to propagate the muon beam position and its polarization accurately in the MC, the relative alignment of the TEC and the spectrometer must be as precise as possible.

The measurement of the misalignment between the spectrometer and the yoke is performed using a technique quite similar to the TEC calibration. Two collimators are installed at each end of the yoke (Fig. D.4). The M13 channel is setup to provide a spread beam of 120 MeV/c pions. The solenoid magnet is not energized in order to obtain straight tracks in the spectrometer. The straight tracks are reconstructed just like in the relative alignment of the DCs and are extrapolated to the collimators. The misalignment of the spectrometer with respect to the yoke is equal to the difference between the track occupancy at the collimators and the position of the collimators.
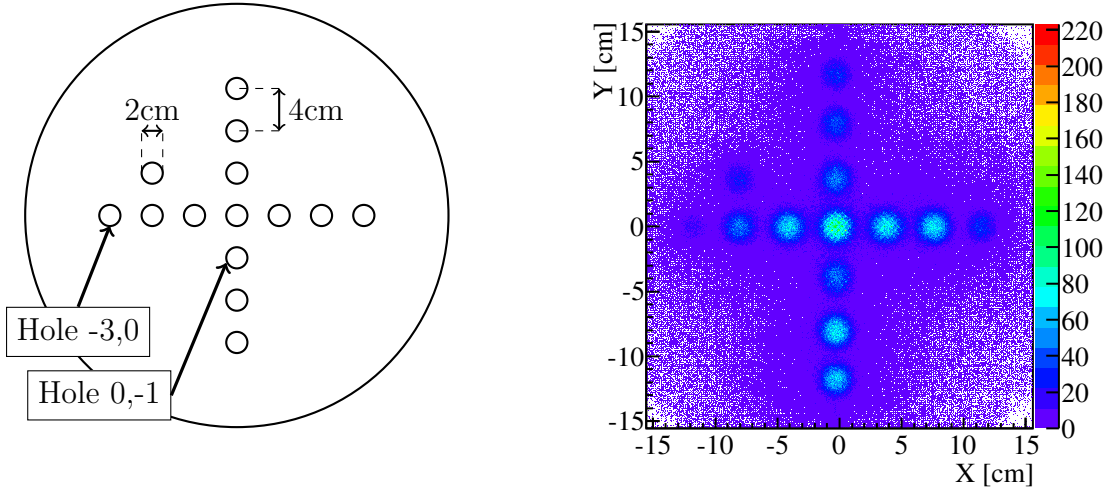
Figure D.4: The collimators installed on the entrances of the yoke contain 14 holes defining a cross plus a hole for the orientation. The holes are labelled using their relative position in x and y such that the hole in the center of the cross is the hole 0,0.

A cut on the track angle selects the tracks going through the corresponding holes upstream and downstream.

The position of the holes cannot be measured accurately by using the peaks of the track occupancy. The pion beam is diverging and therefore the position of the peak of maximum occupancy is not in the center of the holes. The edge of the holes however is less affected by the track occupancy than the peaks. In order to determine the position of the edge of a hole, the cross sections at different height of the occupancy peak are fitted with a circle of constant diameter of 2 cm (Fig. D.5). The cross section with the minimum χ^2 defines the circle fitting the edge and the center of the circle is the position of the hole. The misalignments of the corresponding holes upstream and downstream are compared to determine the translational and rotational misalignment of the spectrometer. The average of the upstream and downstream misalignments defines the misalignment at the center of the spectrometer while the difference defines the angle between the spectrometer and the yoke.

Although the technique of measuring the edge of the holes is less sensitive to the track occupancy, it is possible for a beam travelling at an angle in the spectrometer to bias the measurement. To verify that the alignment procedure is not too sensitive to this effect, the pion beam direction was varied in x using the dipole B2 of the beamline. Variations in the dipole intensity change the track occupancy of the holes
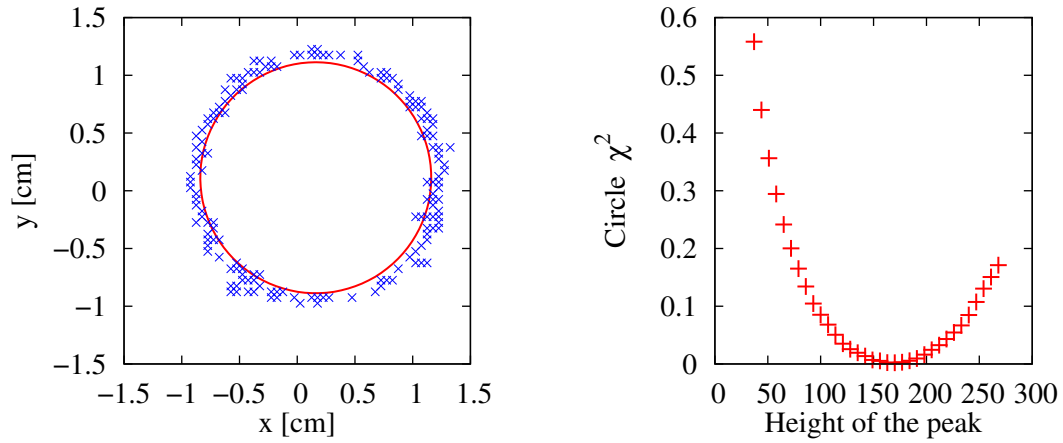
Figure D.5: The cross sections of the track occupancy for a hole are fitted with a circle of constant diameter of 2 cm. The χ^2 of the circle fits reaches a minimum with respect to the height on the occupancy peak. The circle of minimum χ^2 is assumed to be best measure the position of the edge of the hole.

as well as the global angle of the beam in x. The bias due to the hole occupancy is the only uncertainty taken into account in this measurement because it is the largest. The variations of the misalignments measured with respect to the value of the B2 dipole gives an evaluation of this uncertainty (Fig. D.6). Also the track occupancy is not the same for all the holes. The consistency in the displacements measured from different holes is the second element used to evaluate the precision of the measurement.

The installation of the collimators on the yoke requires the upstream beam package to be removed which is a lengthy operation. For this reason only one set of data were acquired for this measurement. The results of the misalignment were extracted from the holes 0,0 upstream and downstream for the B2 DAC value of 11800 which gives the highest occupancy for the central holes and a symmetrically spread beam.

- Translational misalignment in x: (-0.4 ± 0.4) mm

- Translational misalignment in y: (-0.6 ± 0.4) mm

- Rotational misalignment in x: (-1.4 ± 0.1) mrad

- Rotational misalignment in y: (-0.4 ± 0.1) mrad

The pion data with the collimator could not be simulated accurately therefore the alignment procedure could not be performed on the MC. For this reason the spectrometer and the yoke are perfectly aligned in the MC. The misalignment is
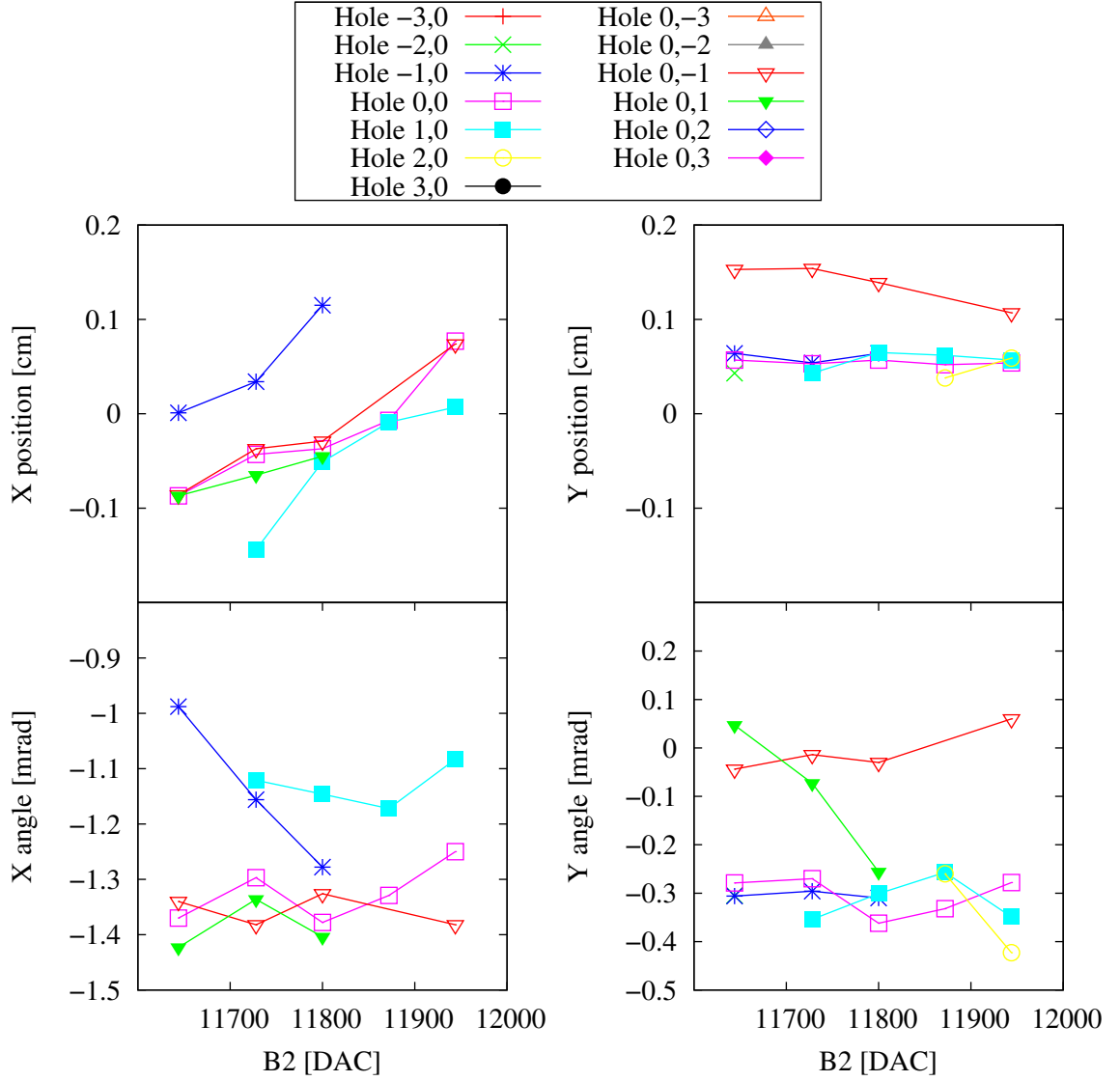
Figure D.6: A change in the B2 DAC value modifies the position and the orientation in x of the pion beam consequently changing the track occupancy in the holes. For the two extreme B2 DAC values, the beam is centered respectively on the holes -1,0 and 1,0. The measured misalignment between the spectrometer and the yoke is sensitive to the hole occupancy in particular the translational misalignment in x.

corrected for the experimental data by using the calibration file defining the position of the DCs. A constant offset as well as a z dependent correction (or "shear") are applied to the DC positions to correct the translational and rotational misalignment of the spectrometer and the yoke.
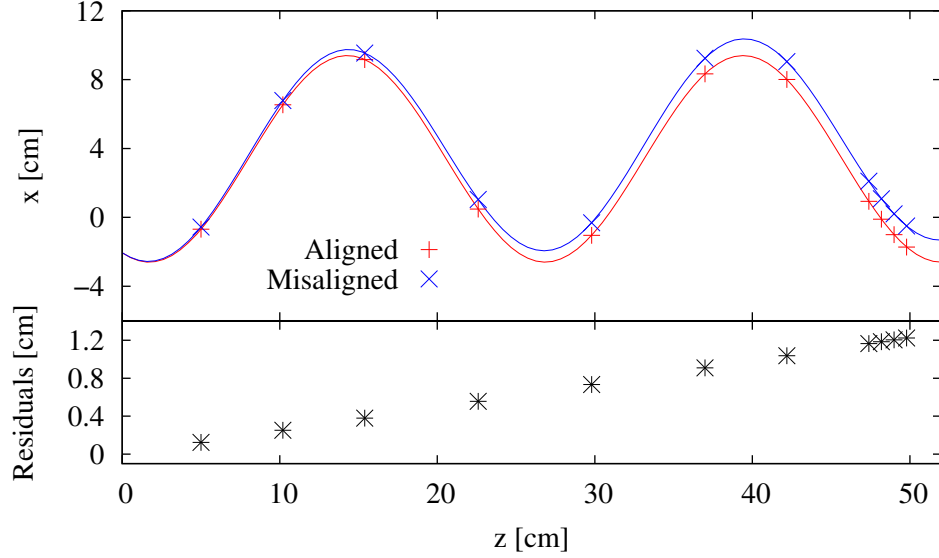
Figure D.7: A misalignment of $\theta_B = 35$ mrad ($2°$) and $\phi_B = 784$ mrad ($45°$) leads to significant residuals potentially biasing the measurement.

D.3 Relative alignment of the spectrometer and the magnetic field map

The high precision reconstruction of the decay positron tracks relies on a very accurate magnetic field map. First of all the shape was studied extensively (Sec. 2.1.3). The second element is the position of the field map with respect to the spectrometer. A mismatch in angle in particular leads to significant reconstruction biases (Fig. D.7). The relative alignment procedure of these two components of the experiment corrects for any rotational misalignment. The translational alignment is not as important due to the very high homogeneity of the magnetic field. It was however evaluated in order for the simulated beam to match the experimental beam as measured by the wire chambers [31]. This evaluation was not used for the reconstruction of the decay positrons but is used for the uncertainty on the position of the magnetic field map (See Sec. 7.1.4).

The misalignment of the magnetic field map with respect to the spectrometer axis

z is described by the polar and azimuthal angles θ_B and ϕ_B such that:

$$B_x = B \sin \theta_B \cos \phi_B$$
$$B_y = B \sin \theta_B \sin \phi_B$$
$$B_z = B \cos \theta_B \tag{D.2}$$

with θ_B small. This misalignment distorts the helix shape in a way that the reconstruction algorithm cannot correct for. In the limit of small θ_B, the misalignment can be approximated by a linear component in z added to the helix. Consequently the misalignment is fitted using the following function to describe the distorted helix:

$$x = a \sin(bz - c) + x_c + d_x z$$
$$y = a \cos(bz - c) + y_c + d_y z \tag{D.3}$$

where a is the amplitude, b is the wavenumber, c is the phase, x_c and y_c are the helix axis position at $z = 0$, and d_x and d_y are the misalignments coefficients.

The relationship between the misalignment coefficients and angles is then:

$$d_x = \sin(\theta_B) \cos(\phi_B),$$
$$d_y = \sin(\theta_B) \sin(\phi_B), \tag{D.4}$$

$$\theta_B = \arcsin \sqrt{d_x^2 + d_y^2},$$
$$\phi_B = \arctan(d_y/d_x). \tag{D.5}$$

The misalignment angles are determined by fitting decay positron tracks with the function Eqs. (D.3). A modified version of MOFIA was developed for that purpose. Only events of event types 1 (one muon and one decay positron well separated in time) and events containing only one reconstructed track are used in the procedure. The list of hits used in the fit are taken from the first guess output with the hit positions wire-centered. A standard χ^2 minimization algorithm uses the first guess parameters of the track as a starting point to fit the functions in Eqs. (D.3). Unlike the standard helix fitter, this reconstruction does not include any kink. This procedure was validated on MC runs and the uncertainty on the θ_B angle is 0.03 mrad.

The measurement of the misalignment between the spectrometer and the magnetic

	Misalignment in x	Misalignment in y
2006 Silver target	0.33 mrad	1.16 mrad
2007 Aluminium target	0.30 mrad	1.12 mrad
2007 Large target	0.32 mrad	1.16 mrad

Table D.1: Rotational misalignment between the spectrometer and the magnetic field map for each run period. The stability of the misalignment shows the robustness of the TWIST spectrometer design and construction. The uncertainty on each measurement is 0.03 mrad.

field map was performed for each run period since the spectrometer was moved in and out of the solenoid between each run period (see Tab. D.1). The misalignment was corrected in MOFIA using a separate calibration file for each run period. The misalignment was also simulated in the MC runs and corrected in MOFIA.